Experimental determination of the partitioning coefficient of nopinone as a marker substance in organic aerosol

Dissertation im Fach Physik

vorgelegt der

Mathematisch-Naturwissenschaftlichen Fakultät

der

Bergischen Universität Wuppertal

von

Dipl.-Phys. Bettina Steitz

aus Bonn

Wuppertal, November 2012

Contents

CONTENTS

CONTENTS

Zusammenfassung

Atmosphärische Aerosole haben einen wesentlichen Einfluss auf die Strahlungsbilanz, die chemischen Prozesse innerhalb der Atmosphäre und damit auf das Erdklima. Sie sind relevant in verschiedenen Umweltprozessen und beeinflussen die menschliche Gesundheit. Sekundäre organische Aerosole machen in vielen Gebieten einen Großteil der Gesamtaerosolmasse aus und bestimmen daher die Eigenschaften der Aerosole. Die vielfältige und komplexe chemische Zusammensetzung sekundärer organischer Aerosole erschwert genaue Analysen ihrer Bildung und ihres chemischen Verhaltens. Diese Informationen sind unter anderem wichtig für die globale und lokale Klimamodellierung. Ein wesentlicher Punkt in derzeitigen Modellen ist die Vorhersage der Menge an organischer Materie innerhalb der Atmosphäre. Hierbei von großer Bedeutung ist ein ausführliches Verständnis der Bildungsprozesse sekundärer organischer Aerosole aus Oxidationsprozessen biogener volatiler organischer Verbindungen. Die Partitionierung der semivolatilen Oxidationsprodukte zwischen Aerosolgas- und Aerosolpartikelphase wird durch den temperaturabhängigen Partitionierungskoeffizienten beschrieben. Dessen experimenteller Ermittlung widmet sich diese Arbeit.

Hierfür wurde eine neuartige Messmethode zur verbindungsspezifischen Analyse organischer Aerosole verwendet. Das Aerosol Collection Module (ACM) ist ein neuentwickeltes Intrument zur Sammlung von Aerosolpartikeln, ihrer Überführung in die Gasphase durch thermische Desorption und zum Transfer in einen angekoppelten Gasphasendetektor zur anschließende Analyse. In dieser Arbeit wurde das ACM erstmals mit einem hochauflösenden PTR-ToF-MS (Proton Transfer Reaction-Time of Flight-Mass Spectrometer) gekoppelt und in α-, und β-Pinen Ozonolyse Experimenten an der AIDA Kammer des Karlsruher Instituts für Technologie (KIT) angewendet. Für die Datenanalyse wurden Auswerteroutinen basierend auf Auswertungsprogrammen für Aerosol Massenspektrometer (AMS)-Daten entwickelt. Für Nopinon, das Hauptprodukt der β-Pinen Ozonolyse, wurde der Partitionierungskoeffizient in Abhängigkeit der Temperatur bestimmt. Dafür wurden zwei experimentelle Verfahren durchgeführt, einerseits die Kopplung des PTR-ToF-MS

mit dem ACM, andererseits Messungen mit dem PTR-ToF-MS mit und ohne Partikelfilter. Für die Partitionierungskoeffizienten aus den ACM-Messungen konnte ein Temperaturverhalten entsprechend theoretischer Überlegungen zur Gas-zu-Partikel Partitionierung aus der Literatur nachgewiesen werden. Ein Vergleich zwischen den Messwerten und anhand von Literatur berechneten Werten zeigt, dass der experimentell bestimmte Partitionierungskoeffizient etwa 1 Größenordnung oberhalb der berechneten Werte liegt. Daraus lässt sich folgern, dass die Menge an Nopinon in der Aerosolpartikelphase in der Theorie unterschätzt wird. Da experimentelle Daten zu den Partitionierungskoeffizienten in der Literatur rar sind, wären weiterführende Untersuchungen der Partitionierungskoeffizienten auch anderer Substanzen mit Hilfe der Verbindung aus ACM und PTR-ToF-MS wünschenswert. Dies würde einen Abgleich der theoretischen Betrachtungen mit experimentellen Ergebnissen ermöglichen und schließlich zu einer Verbesserung im Verständnis der Bildung und somit der Vorhersage von sekundärem organischem Aerosol führen.

Abstract

Atmospheric aerosols have a significant influence on the radiation budget and chemical processes in the atmosphere. Thus, they have an impact on climate. They are relevant in many environmental processes and influence human health. In many regions, secondary organic aerosol (SOA) makes a major contribution to the total aerosol mass. Therefore, SOA significantly influences aerosol properties. The complex and versatile chemical composition of SOA makes the analysis of its formation and chemical behavior difficult and thus complicates global and local climate modeling. One major issue in current models is the prediction of the organic matter in the atmosphere. For this, a detailed understanding of SOA formation from volatile organic compounds (VOCs) is of importance. VOCs undergo oxidation in the atmosphere which results in the formation of semivolatile organic compounds. These partition between the gas and the particle phase. The compound-specific gas-to-particle partitioning can be described with the temperature-dependent partitioning coefficient. This work is dedicated to its experimental determination.

To this end, a new measurement technique for compound-specific analysis of organic aerosol was used. The Aerosol Collection Module (ACM) is a newly developed instrument which collects aerosol particles, converts them into the gas phase via thermal desorption and transfers them to a gas phase detector for further analysis. In this work, the ACM was coupled to a high-resolution Proton Transfer Reaction-Time of Flight-Mass Spectrometer (PTR-ToF-MS) for the first time and used in α -, and β-pinene ozonolysis experiments at the AIDA chamber of the Karlsruhe Institute of Technology (KIT). For the data analysis, routines were developed based on Aerosol Mass Spectrometer (AMS) data analysis. The partitioning coefficient of nopinone, as the major β-pinene ozonolysis product, and its temperature dependence was determined. For this purpose, two experimental approaches were employed: the coupling of ACM and PTR-ToF-MS, and measurements using the PTR-ToF-MS with and without particle filter. The temperature dependence of the partitioning coefficient derived from ACM and PTR-ToF-MS was comparable

to the theoretical temperature dependence found in literature. A comparison with calculated partitioning coefficients following theory showed that the experimental partitioning coefficients of this work were about one order of magnitude higher. This leads to the conclusion that the amount of nopinone in the aerosol particle phase is underestimated by theory. As literature on experimentally derived partitioning coefficients is sparse, further investigations of the partitioning coefficient of other substances with the combination of ACM and PTR-ToF-MS could help to improve the understanding of SOA formation and, thus, SOA prediction.

Chapter 1

Introduction

1.1 Atmospheric Aerosols

Aerosols are defined as liquid and/or solid particles suspended in gas. This work concentrates especially on the partitioning of specific semivolatile compounds between the gas and particle phase.

Sources of atmospheric aerosols can be anthropogenic, such as fossil fuel combustion, as well as natural, e.g. plant emissions, sea spray, mineral dust, biomass burning, and volcanoes, to only name a few. While the above mentioned sources emit aerosols directly, i.e. are sources of primary aerosol, atmospheric chemistry is a source of so-called secondary aerosol.

Aerosol sizes typically range from 10^{-9} m to 10^{-3} m. Depending on their size, number and chemical composition, atmospheric aerosols have different effects. Most widely known are health issues and the impact of aerosols on climate (e.g. (IPCC, 2001), (IPCC, 2007)). The present work concentrates on the aerosol characteristics influencing climate.

1.2 Aerosols and climate

The different effects of atmospheric aerosols on climate can be basically divided into direct and indirect effects.

On the one hand, scattering and absorption of solar radiation by aerosol particles are directly effecting the radiative balance of the atmosphere, and therefore have an impact on climate. On the other hand, aerosol particles can act as cloud condensation nuclei. They have a major influence on the formation of clouds as well as on cloud properties. In this way, aerosol particles have an indirect effect on the radiation budget and climate (IPCC, 2001).

Overall, aerosols are calculated to have a cooling effect on climate (IPCC,

2007). The radiative forcing of the fundamental climate affecting components can be seen in Figure 1.1.
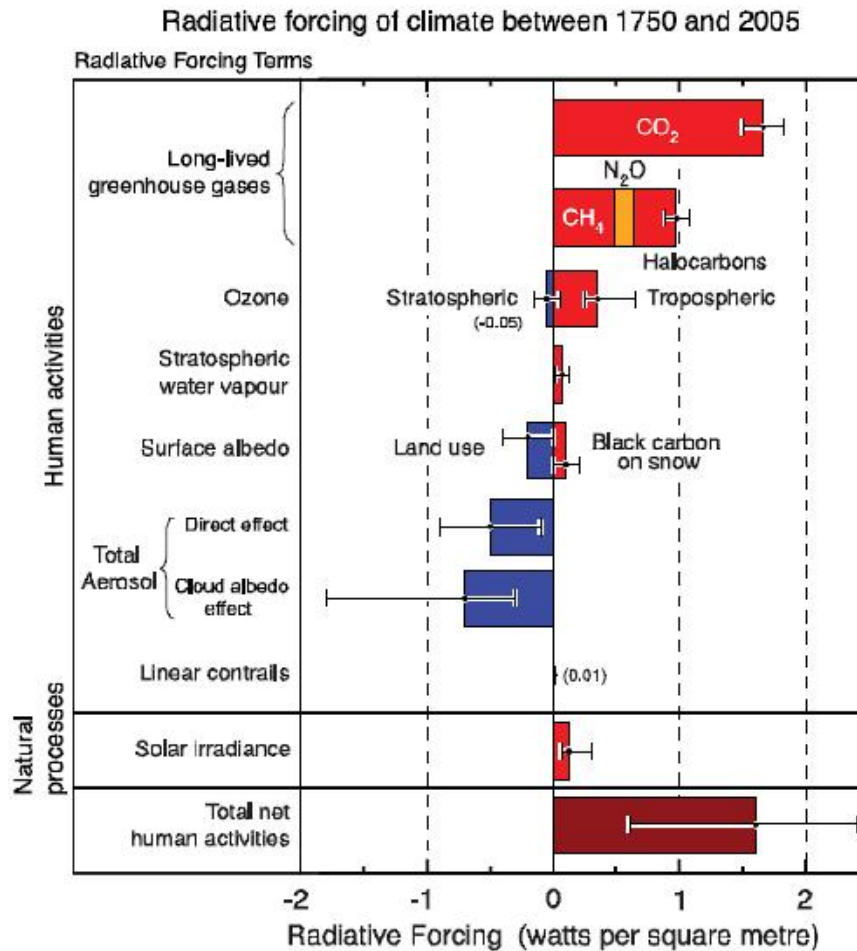
Figure 1.1: Principle components influencing the radiative forcing (IPCC, 2007). The displayed values show the radiative forcing of the year 2005 relative to 1750, as a representative date for the start of the industrial era. Positive forcing is in accordance with a warming effect on climate, while negative forcing represents a cooling effect. Error bars indicate the ranges of uncertainty of the shown values. It can be seen that the uncertainties are especially high for the radiative forcing of aerosols concerning their direct as well as their indirect effect.

Regarding the uncertainties for the different radiative forcing values in particular, it can be seen that there is a high uncertainty about the impact of aerosols on climate. This leads to major problems in global climate modeling (Kiehl, 2007).

As organic aerosol (OA) makes up 20-90 % of the total submicron particulate mass in the atmosphere (Kanakidou et al., 2005), it can be considered of major importance in understanding the different influences of aerosols on climate. Nevertheless, OA sources, its evolution in the atmosphere, and its sinks are still a matter of uncertainty (Jimenez et al., 2009).

Despite the amount of research that has already been done in this area (e.g. (Spracklen et al., 2011), (Koch et al., 2009), (Kulmala et al., 2011)), there is still a high uncertainty about the exact influence of organic aerosols on climate. Regarding the organic particulate mass in the atmosphere, a comparison of model studies to measured data still shows great differences depending on the investigated area and initial assumptions in the simulation (see e.g. (Spracklen et al., 2011), (Kulmala et al., 2011)). Mainly, the models tend to underpredict organic aerosol mass.

1.3 Formation of secondary organic aerosol

The basics of the formation process for organic aerosol are shown in Figure 1.2. Organic aerosol can be emitted directly from its source, leading to primary organic aerosol. By atmospheric evolution, such as chemical reaction, condensation of vapor species, etc., it can alter to secondary organic aerosol (SOA) (Seinfeld and Pankow, 2003).

The second formation path of SOA starts with emissions of volatile organic compounds (VOC). Although anthropogenic emissions can be of importance in locally highly polluted areas, on a global scale anthropogenic VOC contributions to SOA are of smaller abundance. Biogenic VOCs are the major precursors for secondary organic aerosol (Hallquist et al., 2009), (Kanakidou et al., 2005). Field studies show that oxygenated species dominate in organic aerosols and that secondary organic aerosol very likely contributes their major fraction (Zhang et al., 2007).

There are several chemical mechanisms identified to contribute to SOA formation. However, the major contribution comes from oxidation by atmospheric OH, NO_3 and O_3, where ozonolysis contributes the main part (Kanakidou et al., 2005). The resulting oxidation products will, depending on their volatility, either remain in the gas phase, or, if the oxidation products are semivolatile, be partially converted into the particulate phase by nucleation

or by gas-to-particle partitioning, forming secondary organic aerosols.
Comparison of global climate models with field studies show that SOA is
underrepresented in global climate models, leading to the already mentioned
bias between model studies and measurements (see 1.2), e.g. (Zhang et al.,
2007). The understanding of the formation of SOA and the explicit integra-
tion of such knowledge into global climate models is therefore crucial for a
better understanding and prediction of climate.
One of the key points in SOA formation is the gas-to-particle partitioning,
which describes the transition between the gas phase and particle phase of a
compound. It mainly depends on the vapor pressure of a compound and thus
also on the temperature. Generally speaking, at 298 K an organic compound
is considered to be in the gas phase if it has a vapor pressure higher than 0.1
mbar, semivolatile if its vapor pressure is between 0.1 mbar and 10^{-7} mbar,
and in the particle phase for a vapor pressure below 10^{-7} mbar (Goldstein
and Galbally, 2007).
The partitioning between gas and particle phase can be characterized by the
partitioning coefficient.
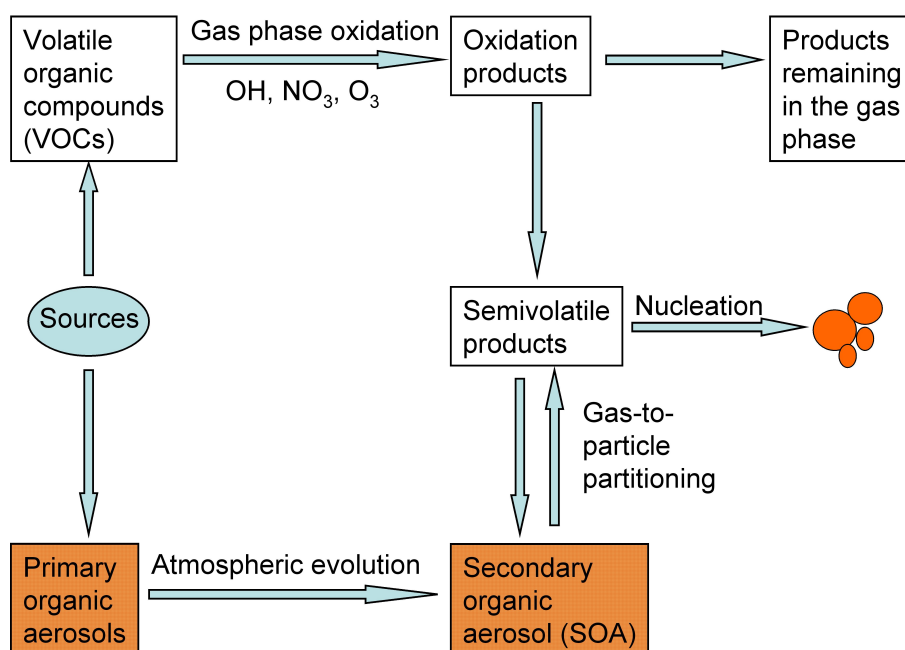
Figure 1.2: Basic formation mechanisms of secondary organic aerosol (SOA),
adapted from (Seinfeld and Pankow, 2003).

1.4   Partitioning coefficient

Organic compounds can be adsorbed and/or absorbed on or into particulate matter. How much of a specific organic compound is adsorbed or absorbed depends on the total suspended particulate matter. Following Seinfeld and Pandis (2006), at a given temperature the gas-to-particle partitioning of an aerosol in equilibrium can be described by the partitioning coefficient as:

$$K_{p,i} = \frac{C_{p,i}}{C_{g,i} \times C_{TSP}} \qquad (1.1)$$

$K_{p,i}$	Equilibrium partitioning coefficient in $m^3 \cdot \mu g^{-1}$
$C_{p,i}$	Mass concentration of a species i in the aerosol particle phase per unit air volume in $\mu g \cdot m^{-3}$
$C_{g,i,}$	Mass concentration of a species i in the gas phase per unit air volume in $\mu g \cdot m^{-3}$
C_{TSP}	Mass concentration of the total suspended mass of particles per unit air volume in $\mu g \cdot m^{-3}$

The partitioning coefficient $K_{p,i}$ provides a measure of the ability of a species i to exist in the particulate phase in equilibrium with the gas phase, given that there is already the mass concentration $C_{p,i}$ of the investigated compound in the particulate phase and the mass concentration $C_{g,i}$ in the gas phase. As a high total suspended mass concentration makes it easier for a species to exist in the particle phase due to surface condensation, absorption, and adsorption, $K_{p,i}$ is normalized to the total suspended particulate mass C_{TSP}.

Equation 1.1 does not give any information on the exact mechanisms which lead to the specific gas-to-particle partitioning of the investigated compound, but when measuring $C_{p,i}$, $C_{g,i}$ and C_{TSP}, Equation 1.1 provides a comparatively easy approach on getting experimentally derived information about the partitioning of a specific organic compound.

1.5 Objectives of this work

As shown in chapters 1.2 and 1.3 a better knowledge of the partitioning coefficient is crucial to enhance the understanding of SOA formation and, therefore, improve climate models. As theoretically derived values leave a high range of uncertainty (see chapter 5.3.1), experimental investigations of the partitioning coefficient are indispensable.

There are numerous well-developed techniques for compound-specific measurements of the gas phase (e.g. Gas Chromatography Mass Spectrometer, Proton Transfer Reaction Mass Spectrometer, etc.). Most of these techniques leave the sampled compounds relatively undisturbed or allow the original concentration of the compound in question to be determined.

The situation is different for the measurement of atmospheric particles. The sampling of particles on quartz or teflon filters is a well-known off-line measurement technique which allows the measurement of, for example, the concentration and the chemical composition of particles. Filter measurements are comparatively low in price and easy to handle, but they also involve a number of difficulties. Prior to analysis the filters are usually stored, which can lead to particle aging and thus to changes in composition. In addition, there is a loss of semivolatiles during sampling and storage, with respect to filter sampling of aerosols. Releasing the particles from the filter with chemical solvents or by thermal desorption can also alter the particles. AMS (Aerosol Mass Spectrometer) is one example of an on-line measurement technique which directly analyzes the particles. However, due to the involved electron impact ionization it only allows the particles to be analyzed in terms of compound classes.

Ideally, one would wish for an online method for compound-specific particle measurements without any alteration of the composition due to the measurement process. Within this work a new quasi-online measurement technique for compound-specific measurements of the aerosol particle phase was used and further developed to investigate the partitioning coefficient of the β-pinene ozonolysis product nopinone at different temperatures. To this end, an Aerosol Collection Module (ACM, see chapter 2.2) was coupled for the first time (see chapters 3.2 and 4.5) to a high resolution Proton Transfer Reaction-Time of Flight-Mass Spectrometer (PTR-ToF-MS, see chapter 2.1) to allow the analysis of the aerosol particle phase and the aerosol gas phase.

Chapter 2

Instrument description

In this work, two methods of deriving the partitioning coefficient are investigated. One method uses a combination of ACM (Aerosol Collection Module, section 2.2) as a quasi-online measurement technique of the aerosol particle phase and a PTR-ToF-MS (Proton Transfer Reaction-Time of Flight-Mass Spectrometer, section 2.1). By comparison of particle phase data with gas phase data the gas-to-particle partitioning can be observed.

The other approach uses the PTR-ToF-MS only. The investigated gas phase samples, where the particulate material is removed by a filter, are compared to samples including gas- and particulate phase. In this chapter the instruments and the PTR-ToF-MS data handling are explained.

2.1 Proton Transfer Reaction-Time of Flight-Mass Spectrometer (PTR-ToF-MS)

The PTR-ToF-MS is a high resolution mass spectrometer (IONICON Analytik, Innsbruck). Detailed descriptions can be found in literature, e.g. (Jordan et al., 2009), (Cappellin et al., 2010). Here, only the major working principle, some of the details, important in this work, and the basics of the applied data analysis are described.

2.1.1 Working principle

Figure 2.1 shows the basic set-up of the PTR-ToF-MS. It consists of four major parts: an ion source, a drift tube, a transfer lens system, and a time-of-flight section.

The ion source is a hollow cathode in which H_3O^+ ions are generated from water vapor. H_3O^+ is used as a primary ion for ionization of the analytes.
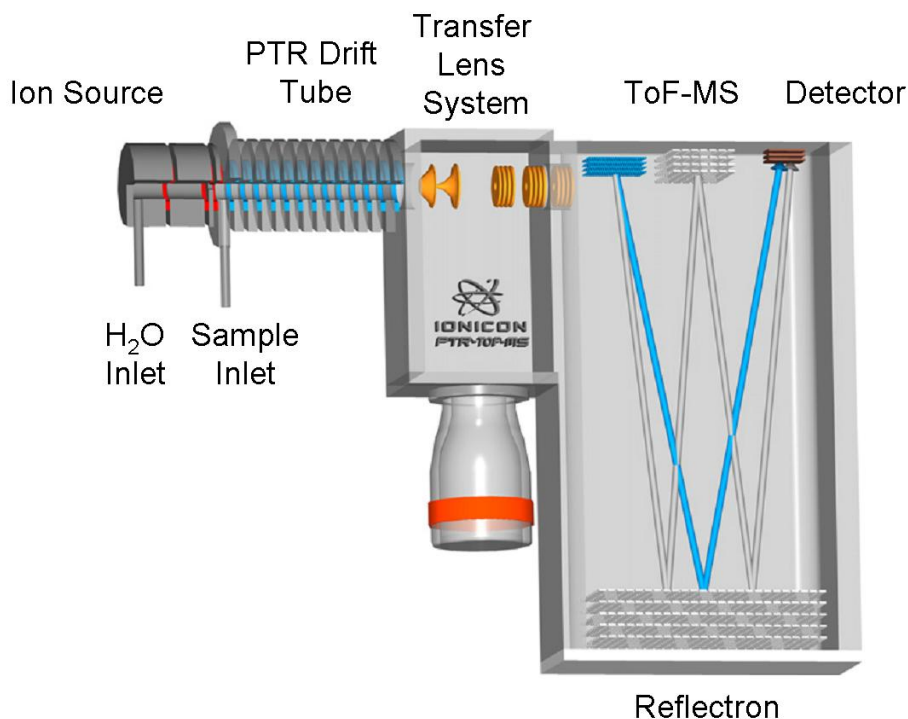
Figure 2.1: PTR-ToF-MS set-up developed by IONICON Analytik; (Jordan et al., 2009).

These enter the system through the sample inlet. Primary ions and analytes are led through the drift chamber by an electric field. There, all compounds with proton affinities higher than water are ionized via chemical ionization with H_3O^+ (for details on the ionization see section 2.1.2).

Connected to the drift chamber is a transfer lens system, which focuses the ions onto a narrow beam and leads them to the time of flight section. Using a pulsed electric field, every few micro-seconds a package of ions is injected into that section. A repulsive electric potential at the reflectron forces the ions onto a V-shaped flight path until they reach the detector. On the one hand, a longer flight path enhances mass resolution, on the other hand, the reflectron allows to correct for ions with a non-ideal injection into the time of flight part of the instrument (see section 2.1.4). Following this procedure, the information of a full mass spectrum is available at any time of the measurement.

The time of flight of each ion is proportional to its mass to charge ratio (m/z). Under normal operating conditions the charge equals one. The measurement

technique results in high mass resolution gas phase mass spectra (for details
on the mass resolution see section 2.1.3).

2.1.2 Ionization

The PTR-ToF-MS uses proton transfer as a chemical ionization method. Due
to the low excess energy which is released during this ionization process the
analytes undergo only minor fragmentation. For many species the ionized
original compound can be observed in the resulting mass spectra. Thus, the
PTR-ToF-MS works with a soft ionization method.

In this work H_3O^+ is used as primary ion. Both, the primary ion and the
analyte R, are led through the PTR-ToF-MS drift chamber where the ioniza-
tion takes place. If the analyte has a higher proton affinity than water, H_3O^+
is depleted of one proton, which is then attached to the analyte. This process
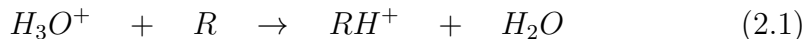leaves H_2O and the analyte including one additional proton (see Equation
2.1). Therefore, the analyte will be seen in the mass spectra on its molecular
mass plus one.

$$H_3O^+ \quad + \quad R \quad \rightarrow \quad RH^+ \quad + \quad H_2O \tag{2.1}$$

The concentration of the reactant $[R]$ can be retrieved by

$$[R] \approx k \cdot t \cdot \frac{[RH^+]}{[H_3O^+]} \tag{2.2}$$

where k is the reaction rate between the analyte and H_3O^+, t is the resi-
dence time of a compound in the drift chamber, $[RH^+]$ is the concentration
of the ionized analyte, and $[H_3O^+]$ is the concentration of the primary ion
(Lindinger et al., 1998).

As the compounds only undergo ionization if the exchanged proton is fi-
nally on a lower energy level than at the beginning, regarding the system
H_3O^+ and the analyte, the ionization mechanism is bound to result in a
compound-specific amount of excess energy, which is to be released. This
can either happen through collision with other compounds in the drift cham-
ber, leaving the original analyte intact in its molecular structure, or it can
lead to fragmentation of the analyte.

The exact fragmentation pattern depends on three different aspects:

1. the energetic difference between the initial and the final state of the sys-
tem, i.e. the difference in the proton affinity of a specific compound compared
to that of water;

2. the molecular structure of the compound, which leads to preferential split-
ting up of some of the molecular bondings, therefore making some fragments

more likely than others;

3. the conditions in the drift chamber, which define the probability for the ion to release its excess energy through collision with other molecules.

The drift chamber conditions are determined by the E/N ratio, which is a ratio between the electric field E and the number of molecules N in the drift chamber. Low E/N leads to low fragmentation, but it also leads to a high stability of water clusters $H_3O^+ \cdot (H_2O)_n$ with $n = 1, 2, 3, ...$, which have different reaction rates and proton affinities. A high amount of water clusters results in competing ionization reactions to the ones with H_3O^+.

A high E/N, on the other hand, leads to low cluster concentration but also to a higher fragmentation. Lindinger et al. (1998) recommend E/N values between 120 Td and 140 Td to provide a good compromise for low concentration of water clusters and low fragmentation. Fragmentation studies at different E/N-values (e.g. from Tani et al. (2003)) lead to the conclusion that the fragmentation of a specific compound can be considered comparable to other studies only for similar E/N-values. The experimental conditions of the experiments presented in this work lead to an E/N of 154.14 ± 7.78 Td (for details of the specific PTR-ToF-MS conditions leading to this E/N see Table 3.1). Therefore, the fragmentation is slightly higher than for the values Lindinger et al. (1998) recommend. A fragmentation study for this work considering α-pinene, β-pinene, and nopinone is given in chapter 4.3.

2.1.3 Mass resolution

Following the IUPAC (International Union of Pure and Applied Chemistry) definition, the mass resolution R of a peak at mass m and peak width Δm in a mass spectrum is defined as

$$R = \frac{m}{\Delta m} \tag{2.3}$$

A mass range from m/z 1 to m/z 400 is explored in the experiments within this work. Considering this range, a resolution of several hundred would result in unit mass resolution spectra, where peaks on the same integer mass cannot be distinguished. The time-of-flight part of the PTR-ToF-MS allowed to gain the mass spectra presented in this work with a mass resolution of $\approx$ 3000. This allows for example to distinguish between oxygenated and not oxygenated compounds. Figure 2.2 shows an example for ketene and propene on integer m/z 43. They have a mass difference of 0.037 and can therefore be separated with a mass resolution of 3000. A mass resolution of e.g. 300 would result in unit mass resolution where both peaks would be seen as one. A high mass resolution also provides the opportunity to find interferences of

different ions on one integer mass, which would lead to misinterpretations of the resulting concentrations of a compound in unit mass resolution as shown in Figure 2.3.
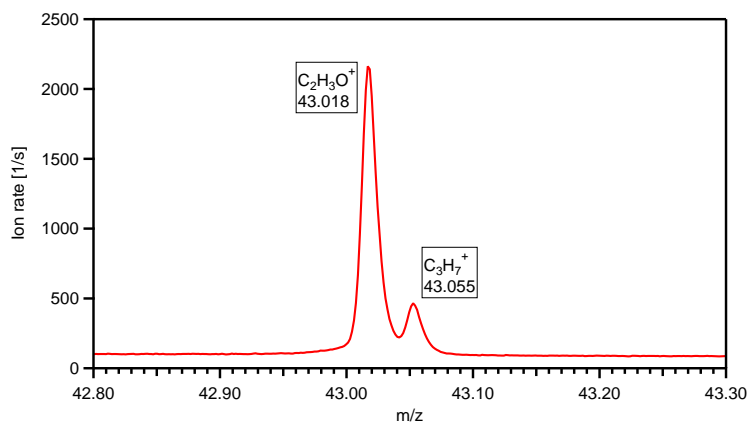
Figure 2.2: Example for the mass resolution in the PTR-ToF-MS. Ketene and propene can be distinguished at a mass difference of 0.037 with a mass resolution of 3000.
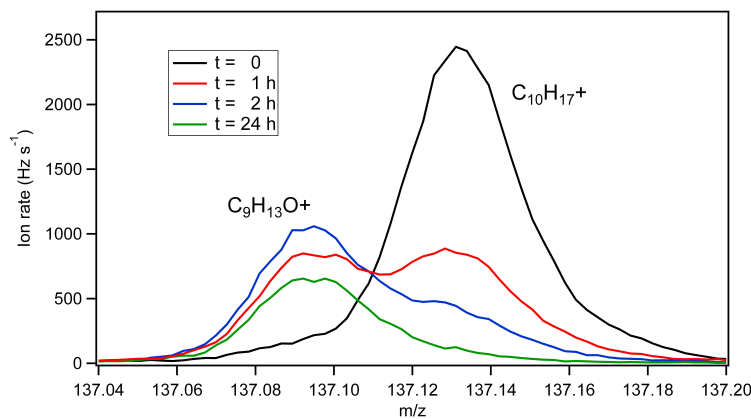
Figure 2.3: High resolution of PTR-ToF-MS data showing the time evolution of an identified interference of an oxygenated β-pinene ozonolysis product $C_9H_{13}O^+$ with the β-pinene parent ion $C_{10}H17^+$, both on nominal mass 137. The measurement was conducted at the Jülich Aerosol Chamber in a β-pinene ozonolysis experiment described in Hohaus (2009).

2.1.4   Data Handling

As the PTR-ToF-MS is a relatively new instrument, a routine for data analysis had to be developed within this work. The data analysis was conducted in analogy to AMS (Aerosol Mass Spectrometer; (Jayne et al., 2000)) data analysis. Therefore, the Igor Pro[1]-based analysis tools SQUIRREL (SeQUential Igor data RetRiEvaL[2]) and PIKA (Peak Integration by Key Analysis[3]) were adapted to process the PTR-ToF-MS data. SQUIRRL is a ToF-AMS Unit Mass Resolution Analysis Software, while PIKA is a ToF-AMS High Mass Resolution Analysis software [4]. Thus, these tools allow to handle data in unit mass resolution, as well as in high mass resolution.

Unit Mass Resolution   Two general pre-processing steps have to be conducted before unit mass resolution data analysis: a mass scale calibration and a baseline subtraction.

As a first step, a mass scale is assigned to the flight times of the ions from the time-of-flight section of the PTR-ToF-MS. This corrects for drifts in the mass scale, which can occur during the experiment. The mass scale is calibrated with signals from ions which are present throughout the whole dataset. In this work, the isotope $H_3^{18}O^+$ at m/z 21.0226 of the primary ion H_3O^+, the water cluster $H_5O_2^+$ at m/z 37.0290, $C_3H_7O^+$ which is protonated acetone at m/z 59.0497, $C_6H_{12}^+$ at m/z 84.0939 and $C_6H_{11}O^+$ at m/z 99.081 were chosen for the mass scale calibration.

By looking at the mass scale calibrated raw data the integration areas for unit mass resolution are defined. The areas in between are used to calculate a baseline with reference to each peak integration area. This baseline is subtracted. Afterwards, for every integer mass to charge (m/z) value all signal within the peak integration area is integrated to determine the unit mass resolution data.

Looking into the data in unit mass resolution can help to get an overview before having a detailed look into the high mass resolution data, as this can be very complex. Additionally, this approach provides data which is directly comparable to PTR-MS data from instruments operating with a QMS (Quadrupole Mass Spectrometer).

---

[1]by Wavemetrics, Inc. www.wavemetrics.com

[2]Developed by university of Manchester, University of Colorado, Boulder, Max-Planck Institute for Chemistry, Mainz, and Aerodyne Research, Inc.

[3]Developed by University of Colorado, Boulder

[4]Details on SUIRREL and PIKA can be found at http://cires.colorado.edu/jimenez-group/wiki/index.php/ToF-AMS_Analysis_Software

High Mass Resolution The high mass resolution data processing is conducted based on the unit mass resolution in terms of mass scale calibration and baseline subtraction. In difference to unit mass resolution, the area under the raw signal peaks is integrated instead of all signal within a defined mass range. In order to derive the signal of all ions in a mass spectrum, the following steps are performed: peak shape definition; defining a list of ions which show a signal in the raw spectra; and a least squares fitting of each mass spectrum for all peaks of the defined shape at the m/z position given by the peak list.

The statistic distribution of momentum of the ions entering the electric injection field leads to a Gauss shaped peak. In practice, not all ions enter the electric field optimally (see Figure 2.4). Therefore, not all them pass through the whole electric field and gain the maximum kinetic energy. Partly, the reflectron corrects for ions with less than maximum kinetic energy. These ions do not enter the reflective potential as deep as ions with maximum energy. Therefore, the flight path for ions with low energy is slightly shorter. Nevertheless, the final peak shape shows a tailing to the right for each peak.
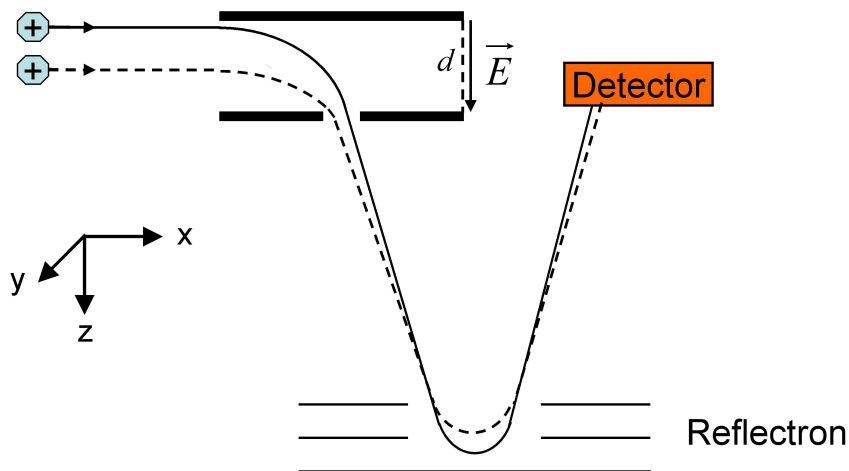
Figure 2.4: Schematic of the electric injection field and the time-of-flight section of the PTR-ToF-MS. The ions (blue octagons) enter the pulsed electric field E. Thus, they are injected into the time-of-flight section. Their kinetic energy in z-direction equals the amount of energy gained from running through this electric field. The black line shows the path of an ion which runs through the whole electric field of length d. The dashed line shows the path of an ion which only runs through a part of the electric field.

The resulting peak shape is defined from the averages of chosen peaks in the data set. In this work, the water cluster peak $H_5O_2^+$, O_2^+, and $H_3^{18}O^+$ were used (see Figure 2.5). All of them were present throughout the whole dataset in an amount high enough to show a representative peak shape.
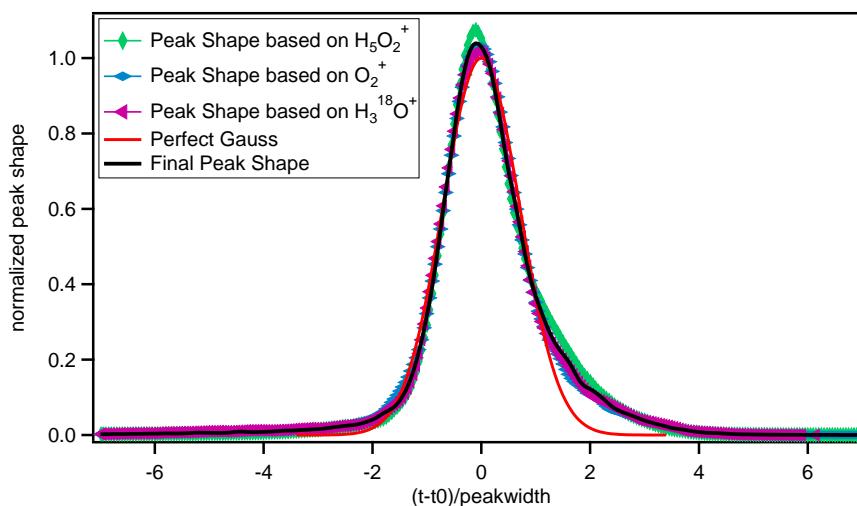
Figure 2.5: Peak shape fitting based on the peak shapes of $H_5O_2^+$ (green), O_2^+ (blue), and $H_3^{18}O^+$ (violet). The resulting final peak shape is shown in black. For comparison, a Gauss peak is shown in red.

In the second step, the raw spectra are viewed to define the list of compounds which appear in the data set. Finally, the determined peak shape is applied to all of these peaks in the raw spectra. The area under the peak is integrated to determine the high mass resolution data. The integrated peak areas result in counts per second for each compound from the defined list of compounds. A detailed description on the determination of mixing ratios for the experiments described in this work can be found in chapter 4.

2.2   Aerosol Collection Module (ACM)

The ACM is a quasi-online device for the measurement of the aerosol particle phase (Hohaus, 2009), (Hohaus et al., 2010). It collects aerosol particles and evaporates them to the gas phase. Combined with a gas phase detector, it provides composition information of the particulate phase of organic aerosols. In this work, the ACM is connected to a PTR-ToF-MS to provide high resolution mass spectra.

2.2.1   Working principle

Details of the working principle of the ACM can be found in Hohaus (2009).
Figure 2.6 shows a schematic of the ACM.
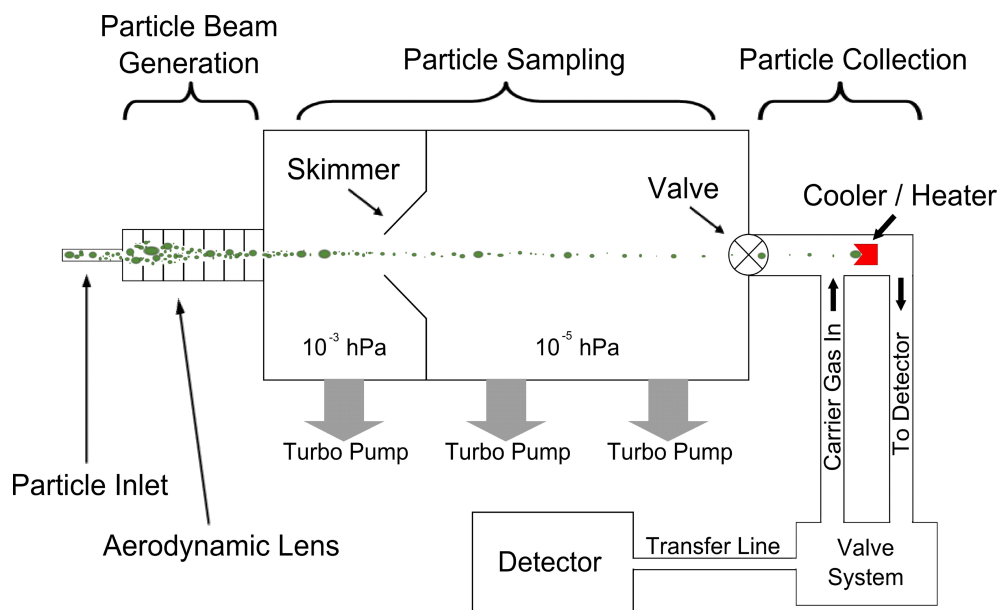
Figure 2.6: Schematic of the Aerosol Collection Module (ACM) in collection
mode (Hohaus, 2009). If coupled with a gas phase mass spectrometer, it allows
measurements of the particle phase of organic aerosols.

    The aerosol is introduced into the ACM via a critical orifice. Follow-
ing, an aerodynamic lens system generates a narrow particle beam. The
beam passes through a differentially pumped vacuum chamber. Here, the
gas phase of the sample is discarded and only the particulate phase is lead
further through the system.
In the collection mode, the particles pass through a valve and are then col-
lected on a cooled collector surface. In the present work, the cooling temper-
ature was -30 °C. The cooling of the collector is essential to ensure that the
particles do not evaporate into the gas phase during the collection time.
After the collection time, the valve to the vacuum chamber is closed and the
desorption mode is initiated by heating the collector up to a desorption tem-
perature of up to 190°C. The collected particles evaporate from the collection
surface and are flushed with synthetic air as a carrier gas through a valve
system to the PTR-ToF-MS, where they are analyzed. A detailed description
of the Aerosol Collection Module and its coupling to a Gas Chromatography

25

Mass Spectrometer (GC-MS) can be found in Hohaus (2009).

2.2.2 ACM collection section

All experiments presented in this work involving the ACM were conducted with the ACM set-up as seen in Figure 2.6 and the collection section as seen in Figure 2.7.
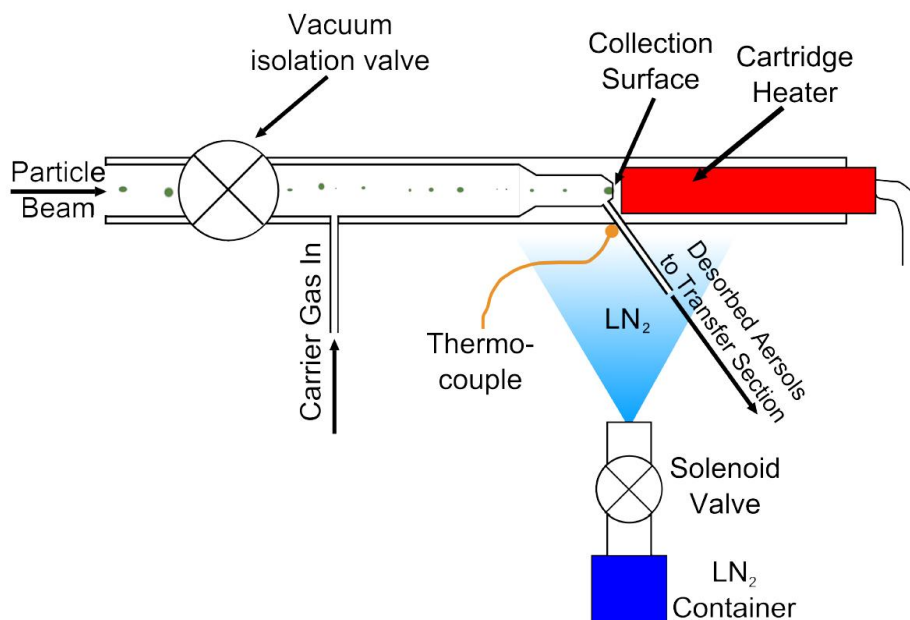
Figure 2.7: Schematic of the ACM-collection section with liquid nitrogen cooling and cartridge heater (from Hohaus (2009))

The ACM-collection section consists of two major parts: the collector and a cooling and heating system to provide the temperatures needed for the cooling during the collection and for the heating in the desorption mode. The collector consists of a 316 stainless steel tubing (length: 80.8 mm, inner diameter: 5.3 mm). It is chemically passivated with an Inertium® coating (Advanced Materials Components Express, Lemont, PA). The collection surface has a diameter of 3.4 mm. It divides the collector in two parts. The 5 mm long collection part, which is connected via the vacuum isolation valve to the vacuum chamber, and the remaining heating part, which is open to ambient atmosphere and filled with a removable cartridge heater.

Connected to the collection part are two tubings with an outer diameter of 1.6 mm and an inner diameter of 1 mm. They are chemically passivated with Silcosteel® (SilcoTek, Bellefonte, PA). The first tubing is located behind the vacuum isolation valve. It introduces the carrier gas, which flushes the evaporated compounds to the gas phase detector. The second tubing is located in front of the collection surface. It leads the carrier gas and the evaporated compounds to the detector.

The desorption process of heating the collector up was conducted in one step from -30 ℃, as collection phase temperature, to 190 ℃, as desorption temperature. The cooling during the sampling phase was ensured with liquid nitrogen. Therefore, a liquid nitrogen container was connected to the collection unit so that the liquid nitrogen could be sprayed onto the outside of the collector. This process was controlled with an automated solenoid valve.

The heating of the collector to the desorption temperature was ensured by the cartridge heater behind the collection surface. It was conducted within approximately one minute. Afterwards the temperature was held for 5 more minutes. Figure 2.8 shows an example of an ACM desorption peak for nopinone, analyzed with the PTR-ToF-MS. During the time before the desorption, the connection between ACM and PTR-ToF-MS is flushed with synthetic air to ensure removal of all remaining compounds in the lines. When starting the desorption, the collected aerosol particles evaporate into the gas phase and are flushed to the PTR-ToF-MS. The sharpness of the desorption peak leads to the conclusion that the compound was evaporated at once. After the desorption peak, the signal decreases due to the synthetic air, which still flushes through the ACM-system to the PTR-ToF-MS.
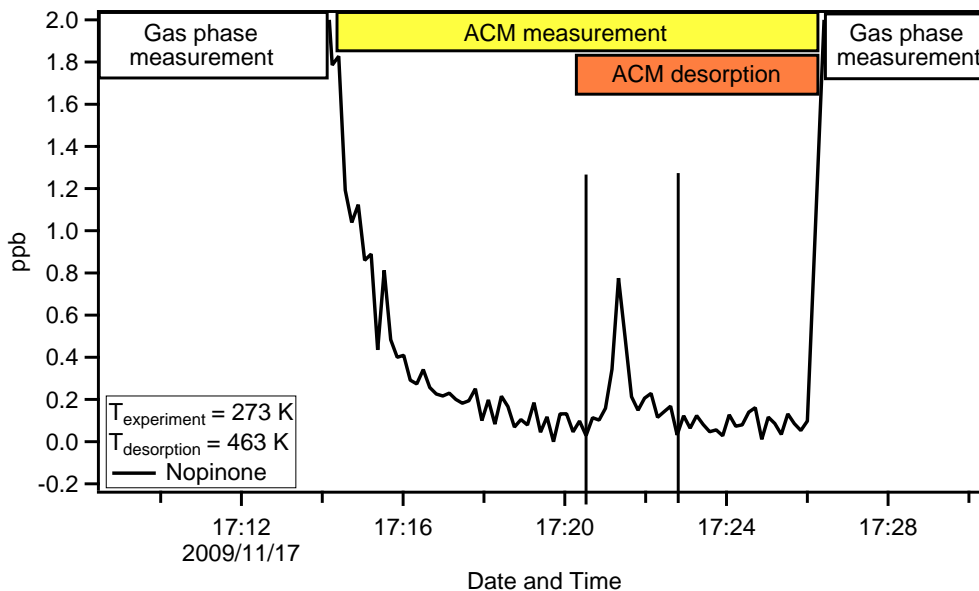
Figure 2.8: Example of an ACM desorption peak for nopinone (black line). In the left and in the right part of the Figure, gas phase was measured. The yellow bar indicates the period of ACM measurement. It starts with several minutes of synthetic air before heating the ACM collector up for desorption. The nopinone desorption peak can be seen between the two vertical lines.

Improvement of the ACM-collection section

Within this work, two major improvements of the ACM-collection section were conducted: changing from liquid nitrogen cooling to a peltier element cooling, and heating of the collector for desorption in several steps instead of one step.

ACM cooling
Although the cooling with liquid nitrogen ensures collection temperatures down to -60 °C, it has a major disadvantage. A container with liquid nitrogen has to be provided at all times during the measurements with the ACM. To facilitate the operation of the ACM the system was changed to be cooled by a peltier element (Peltier-S, EURECA Messtechnik GmbH). As a thermal contact is needed to cool the collector down, a copper block was adjusted to encase the whole collector tube. The dimensions of the copper block (see Figure 2.9) have been adjusted to the system as much as possible to reduce the thermal mass, which has to be cooled down by the peltier element, as well as heated up for the desorption phase. The encasing copper block consists of

28

two parts with grooves for the collector tubings. The two parts are fastened around the collector tubing with 4 screws to ensure a good thermal contact. The lower part of the copper unit has a plane surface of 3×3 cm^2. The peltier element is connected to another 3×3 cm^2 copper plane. This part is moved up and down by a lifting platform (VWR International GmbH), which was motorized for this purpose within this work. The platform is controlled by a thermo element (Type K, RÖSSEL-Messtechnik GmbH), which measures the temperature of the peltier unit. When the peltier-cooled lower copper plane is moved up, it is connected to the copper unit which encloses the ACM collector. Thus, the whole unit is cooled down to approximately -15 °C at surrounding temperatures up to 30 °C. For experiments at temperatures below -15 °C, the copper unit can be removed completely. The ACM can, thus, either be used with the new cooling/heating unit, or with the old liquid nitrogen cooling system.
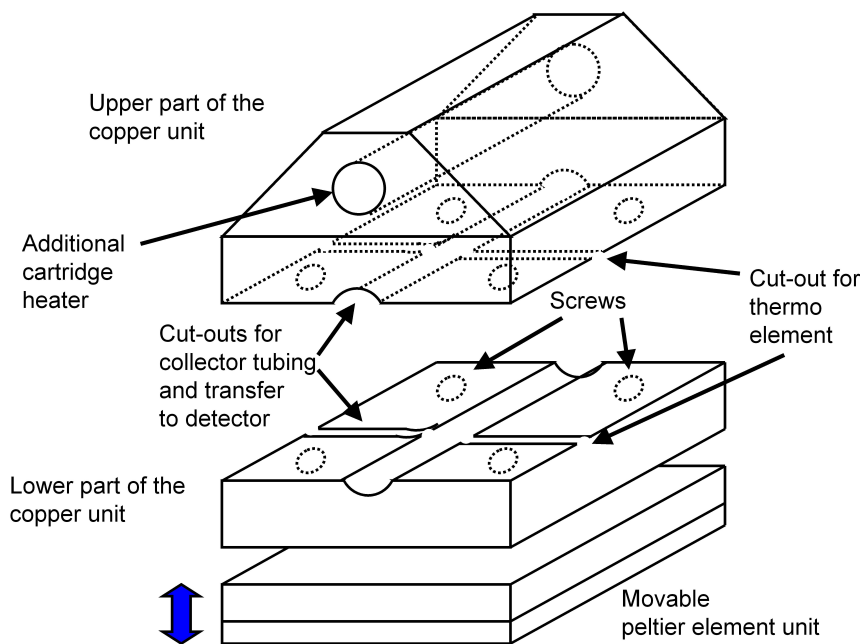
Figure 2.9: Schematic of the new ACM heating and cooling unit with a peltier element

ACM heating
So far, the desorption has been conducted in one step from -30 °C to 190 °C, resulting in one sharp desorption peak (see Figure 2.8). A softer desorption method is to heat the collection unit stepwise. By that, the compounds are

29

supplied with less excess energy, leading to less breaking up of the evaporated compounds. Additionally, this allows a far more detailed look into the composition of aerosol particles by measuring which compounds desorb at a given temperature. Therefore, an automized ramp heating process was developed. It is regulated by the temperatures of the peltier element and the ACM collector. Due to the higher thermal mass from the copper unit which encloses the ACM collector an additional cartridge heater (Türk+Hillinger GmbH) is applied in the upper copper part to ensure a fast heating process.

Test programs

Two test programs with different heating rates were conducted with the new cooling and heating system. The heating rate of test program 1 was 50 $\frac{°C}{min}$ while the heating rate of test program 2 was 80 $\frac{°C}{min}$. The difference in heating rates has been analyzed to give an estimate of the temperature overdrive at the collector. The program steps and the reached collector temperatures are shown in Table 2.1.

Table 2.1: Program steps of the two test programs conducted with the new, automated cooling- and heating-system of the ACM collector. Shown are the set collector temperature (T_{Coll}), the holding time of each temperature (t_{hold}), the temperature in the transfer line ($T_{Transfer}$), and the reached collector temperature for test program 1 and 2.

Step	Set T_{Coll} [°C]	t_{hold} [min]	$T_{Transfer}$ [°C]	Reached T_{Coll} program 1 [°C]	Reached T_{Coll} program 2 [°C]
1)	-20	30	off	-11.3	-15.6
2)	30	6	40	32.0	31.4
3)	80	6	90	82.7	82.6
4)	130	6	140	130.4	131.3
5)	180	6	190	178.3	179.2
6)	-20	hold till program start	off	-14.2	-13.4

The collection temperatures, as well as the holding times and the peltier cooling process were executed automatically via a programmable temperature set point controller (TSC) and a proportional–integral–derivative (PID) controller unit (Wachendorf). In difference to the liquid nitrogen cooling,

it turned out that the peltier element could not cool the collector unit sufficiently while the transfer heating was turned on due to the good thermal contact between the ACM collector and the transfer line. Thus, the transfer heating had to be turned off manually in the cooling periods. For the different heating steps it was set manually to temperature values of 10 °C above the respective collector temperature. This ensures that the particles stay in the gas phase when they are lead through the transfer line. The collector temperature and the transfer line temperature have been recorded during both test programs and can be seen in Figure 2.10. Minor changes in the ACM controller unit will allow to automate the whole ACM heating/cooling process. Furthermore, it is possible to automatically run several programs consecutively.

At the start of the test programs, the peltier element was down and started cooling down from surrounding temperature. The lifting platform drove the peltier element up as soon as the element had reached a temperature -15 °C. It has to be noted, that -15 °C is not the final cooling temperature of the peltier element, but it was considered low enough to start the collector cooling process. Thus, the ACM collector was cooled down to collection temperature. The test programs show that final cooling temperatures of the collector between -11.3 °C and -15.6 °C were reached for set temperatures of -20 °C. However, aerosol particle sampling should be conducted at cooling temperatures at or slightly below the experiment temperature to ensure that the sampled aerosol particles stay in the particulate phase. Thus, the new ACM unit can be used for experiment temperatures down to at least -10 °C. The cooling from room temperature (22.5 °C) down to -11.3 °C was conducted within 10 minutes. In the test programs the collection temperature was held for 30 min. Afterwards, the desorption process was started. The peltier element was moved down to remove it from the copper unit to save the peltier element from damage. The solder in the peltier element will start melting at temperatures above 170 °C. In addition to that, high temperature differences can cause material damage at the inner peltier contacts. The desorption heating was conducted in 4 steps from the final collection temperature up to 180 °C. The aimed temperatures were reached within ± 2.7 °C. After the desorption mode, the peltier element was moved up again and started cooling the collection section. To save the peltier element from damage, the lifting platform is controlled by a protective mechanism. It removed the peltier element from the copper block every time the temperature at the peltier element exceeded 25 °C. When it reached a temperature of -15 °C again the lifting platform reconnected the peltier element with the copper block and the cooling process was proceeded. Thus, the collector cooling was conducted in several steps, as can be seen in the stepwise decrease of

the collector temperature in Figure 2.10. The cooling process from 180 °C down to collection temperature was conducted within 20 min. Therefore, 20 min after accomplishing the desorption process the system can start a new sampling cycle.

Figure 2.10: Collector and transfer line temperatures during the test programs of the new ACM heating/cooling system.

Chapter 3

Experiments

In this chapter the experiments of β- and α-pinene ozonolysis are presented. β- and α-pinene were chosen as representatives of biogenic volatile organic precursor compounds for organic aerosol. The experiments were conducted at the AIDA (Aerosol Interaction and Dynamics in the Atmosphere) simulation chamber at the Karlsruhe Institute for Technology (KIT). The general set-up of the chamber is introduced, as well as the connection to the PTR-ToF-MS and the ACM. The daily cleaning procedure of the chamber is described and the addition of the chemical reactants for the experimental cycle is explained. Experiment-specific conditions and procedures of the PTR-ToF-MS and the ACM are presented, and two experimental set-ups for deriving the partitioning coefficient, on the one hand from PTR-ToF-MS and ACM, on the other from a PTR-ToF-MS combined with a particle filter, are described. In the last part of this chapter, the experimental cycles of all experiments are provided and measurements of the PTR-ToF-MS and the coupled PTR-ToF-MS and ACM are shown.

3.1   AIDA chamber

The AIDA chamber is a dark atmospheric simulation chamber. Its set-up and instrumentation can be seen in Figure 3.1. The AIDA chamber provides the possibility to investigate different aspects of aerosol formation and chemistry under controlled atmospheric conditions like temperature, humidity, pressure, etc. Detailed descriptions of the chamber can be found in Saathoff et al. (2003) and Saathoff et al. (2009). Here, only a brief description of the major parts of the chamber and the instrumentation involved is given. The AIDA chamber consists of an inner cylindrical aluminum vessel of 84.5 m^3 volume and an outer thermally isolated housing. The chamber can be op-

erated at temperatures ranging between 183 K and 333 K. Located at the bottom of the inner aluminum vessel a mixing fan was running during all experiments. It ensured homogeneous mixing of all components within 3 minutes.

The chamber was cleaned prior to each experiment by evacuation to ~ 1 mbar total pressure. Then, it was flushed twice with synthetic air at a pressure of 10 mbar before refilling it with humidified synthetic air (low carbon grade, Basi) to atmospheric pressure (~ 1013 mbar).

For the investigation of the formation of secondary organic aerosol presented in this work, the PTR-ToF-MS (see chapter 2.1) and the ACM (see chapter 2.2) were connected to the inner vessel of the chamber (see fig. 3.2). Detailed descriptions of the connections to the chamber and between PTR-ToF-MS and ACM are given in section 3.2.
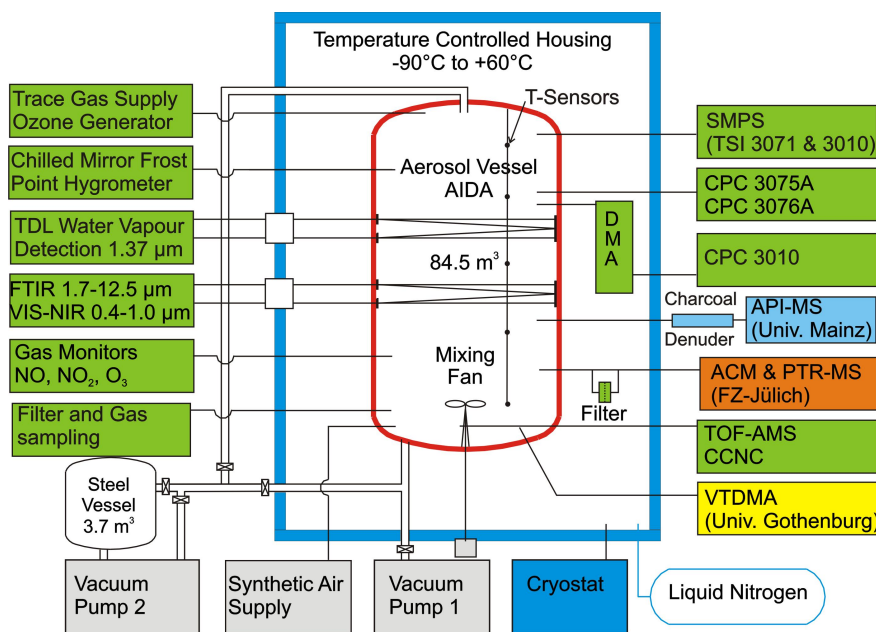
Figure 3.1: Set-up of the AIDA chamber at KIT in Karlsruhe.
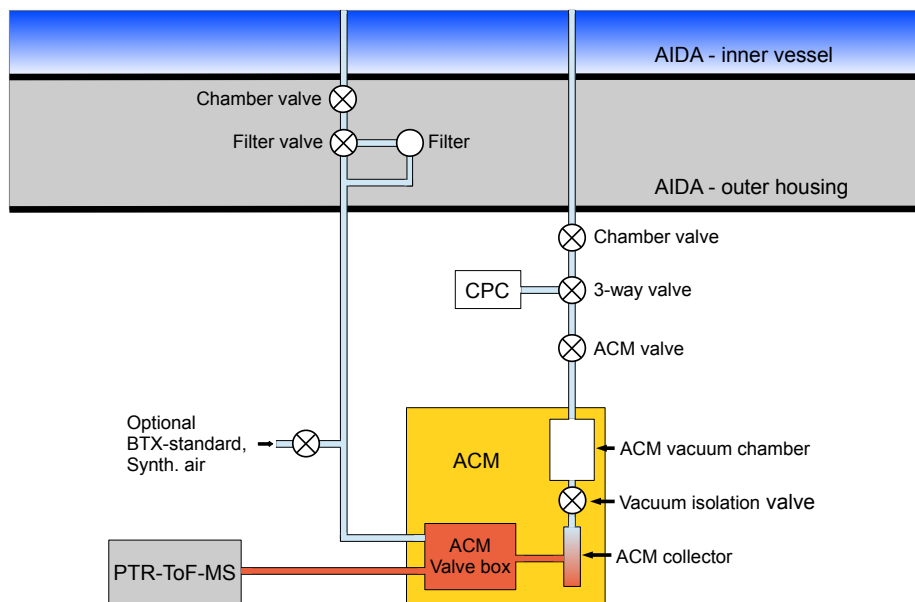
Figure 3.2: Schematic of the connections of PTR-ToF-MS and ACM to the AIDA chamber. The ACM valve box and the connection from the ACM valve box to the PTR-ToF-MS were heated at all times. The ACM collector is cooled during ACM sampling times and heated for desorption. Details of the connections between ACM and PTR-ToF-MS can be seen in Figures 3.3, 3.4, and 3.5.

3.2 Instrumental set-ups and performances

The set-up of the PTR-ToF-MS and the ACM at the AIDA chamber allowed three different measurement modes:
• Measurement of the gas phase with the PTR-ToF-MS via a particle filter (described in section 3.2.1).
• Measurement of the gas and particulate phase of the aerosols via bypassing the particle filter (described in section 3.2.1).
• Measurement of the aerosol particle phase via the ACM (described in section 3.2.2).

3.2.1   Set-up of the PTR-ToF-MS and characterization of the working conditions

In the first measurement mode, the PTR-ToF-MS was connected to the AIDA chamber via a teflon particle filter with a nominal pore size of 200 nm (PTFE, diameter: 47 mm, Sartorius). The filter was located in the isolated housing of the AIDA chamber (see Fig. 3.2). Thus, the filter was at all times at the same temperature as the sample from the inner vessel. With the particle filter in the sampling line the PTR-ToF-MS measured aerosol gas phase.

In the second measurement mode, the filter was bypassed. The PTR-ToF-MS measured aerosol gas phase plus aerosol particle phase. This was reached via a heated PTR-ToF-MS inlet line of 1 m length. The aerosol particles were converted into the gas phase when passing through that inlet line. This approach has previously been tested by Tillmann et al. (2010). Figures 3.3 and 3.4 show the connection schemes of the ACM in standby and in collection mode. In these two modes the PTR-ToF-MS sampled directly from the AIDA chamber. The connection from the chamber leads through the heated ACM valve box. Passing through valve 1, the sample was lead to the PTR-ToF-MS via the heated inlet line.
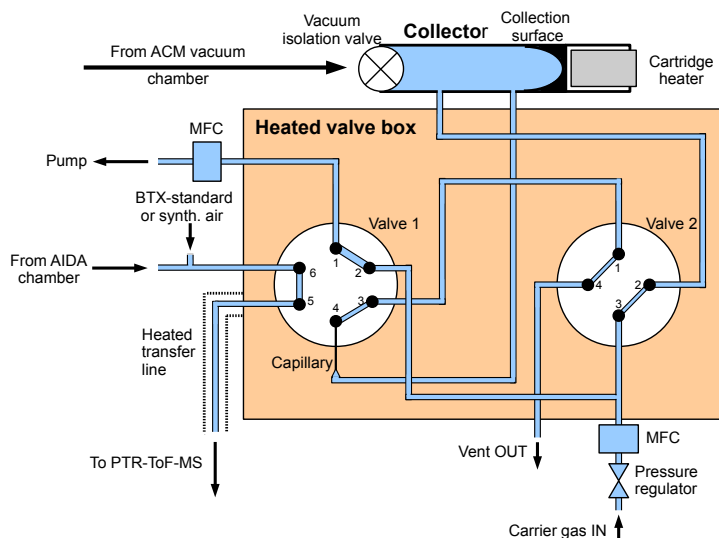
Figure 3.3: Connection scheme of the ACM in standby mode. The active gas flow is shown in blue. See text in section 3.2.2 for description of the standby mode.
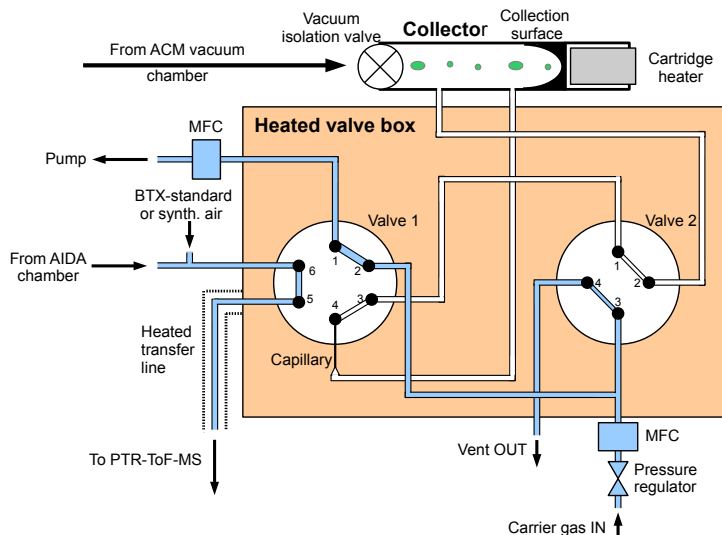
Figure 3.4: Connection scheme of the ACM in collection mode. The active gas flow is shown in blue. The PTR-ToF-MS is measures from the chamber while, separately, the ACM collects aerosol particles (green). See text in section 3.2.2 for description of the ACM collection mode.

Both, ACM valve box, and heated inlet line, were kept at 448 K for all experiments. In addition to results from the ACM, this set-up allowed to gain the partitioning coefficient for compounds which are in the aerosol particle phase at the experiment temperatures of 243 K up to 303 K and evaporate into the gas phase on their way through the heated valve box and inlet line. For this, the PTR-ToF-MS measurements with and without filter were compared (Tillmann et al. (2010), for details on deriving the partitioning coefficient from this set-up see section 4.4, for results see chapter 5.3.1). For calibration a cylinder with a BTX-standard (National Physical Laboratory) was used (for details of the calibration see chapter 4.2). It was connected to the line from the chamber through the ACM valve box to the PTR-ToF-MS (see Fig. 3.2). The set-up allowed to switch between the BTX-standard and synthetic air for background measurements.

The PTR-ToF-MS was operated with an inlet flow of 380 ml per minute. The temperature of the driftchamber was held constant at 333 K. The conditions in the driftchamber, which determine the ionization and fragmentation of the compounds measured by the PTR-ToF-MS can be seen in Table 3.1. They result in an E/N of 154.14 $\pm$ 7.78 Td for all experiments, where E is

the electric field strength and N is the buffer gas number density.

Table 3.1: Arithmetic means and standard deviations of the voltage U_{drift} along the driftpath, the temperature T_{drift} in the driftchamber, the driftchamber pressure p_{drift}, and the resulting E/N for a driftchamber length of 9.6 cm for all experiments.

$\bar{U}_{drift}$ in [V]	$\bar{T}_{drift}$ in [K]	$\bar{p}_{drift}$ in [mbar]	E/N in [Td]
560.05 ± 0.36	333.15 ± 0.04	1.74 ± 0.08	154.14 ± 7.78

3.2.2 Set-up of the ACM and characterization of the working conditions

In the third measurement mode of the ACM-PTR-ToF-MS set-up at the AIDA chamber the aerosol particle phase is measured via the ACM. The ACM was connected to the AIDA chamber via a direct line (see Fig. 3.2). The ACM can be operated in three different modes: the standby, the collection, and the desorption mode. The connection schemes and the respective connections to the AIDA chamber and the PTR-ToF-MS can be seen in Figures 3.3, 3.4, and 3.5.

ACM standby mode: The standby mode was used mainly for the times between experiments to enable a start of the collection mode without any time delay by starting the ACM from shutdown. In standby mode the ACM collection section was closed to the AIDA chamber by the vacuum isolation valve and to the PTR-ToF-MS by the adjustment of valve 1 and 2. The collection section was flushed with carrier gas which was vented out. The PTR-ToF-MS was connected to the AIDA chamber by valve 1. This allowed PTR-ToF-MS measurements from AIDA while the ACM was in standby mode.

ACM collection mode: In the collection mode, the ACM collector was cooled by liquid nitrogen to 243 K. The collection section was open to the AIDA chamber through the open vacuum isolation valve. Thus, the ACM sampled from the AIDA chamber. Aerosol particles were collected in this mode. Via valve 2 the collection section of the ACM was separated from the carrier gas supply. So, the collection section was closed to carrier gas, the vent and to the PTR-ToF-MS. At the same time, the PTR-ToF-MS measured directly from the chamber through valve 1. Thus, PTR-ToF-MS data from the ACM sampling periods are comparable to the samples from the ACM

(see chapter 4.5). Several ACM samplings were conducted in the course of most experiments.

ACM desorption mode: The collection mode was followed by the desorption mode. The connection between the collector and the AIDA chamber was closed by the vacuum isolation valve, ending the aerosol particle collection. The liquid nitrogen cooling was stopped, and the collector was heated up by the cartridge heater. By switching valve 1 the carrier gas was flushed through the collection section of the ACM, carrying the evaporated aerosol to the PTR-ToF-MS which was connected to the ACM collection section instead of to the AIDA chamber in this mode.

Tables 3.2 and 3.3 show an overview of the relevant experimental details for the ACM sampling and desorption periods. The ACM was operated with a flow of $\sim$ 84 ml per minute. Collection times lay between 25 minutes up to 187.5 minutes. During the desorption process, the whole sample was transported to the PTR-ToF-MS in only a few minutes with a flow of 380 ml per min. Therefore, the PTR-ToF-MS measured a concentrated sample. To correct for that, the PTR-ToF-MS signals from ACM measurements have to be corrected with a factor derived from the values seen in Tables 3.2 and 3.3 (see section 4.5).
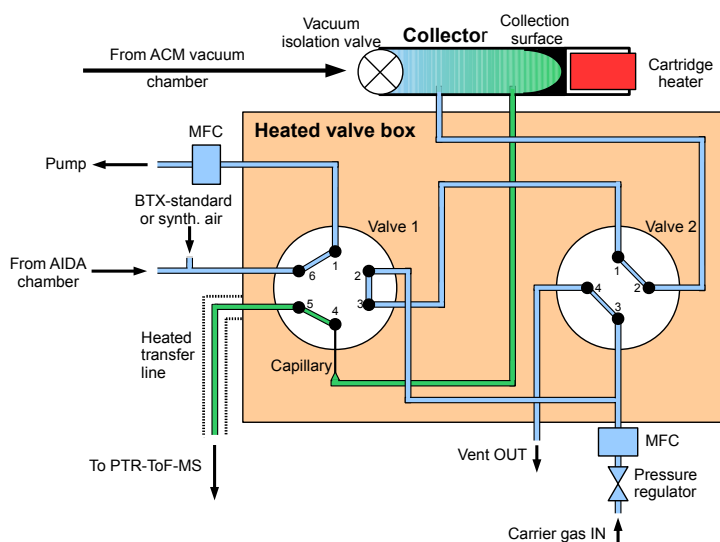
Figure 3.5: Connection scheme of the ACM in desorption mode. The active gas flow is shown in blue and green. Green lines show the carrier gas with the desorbed aerosol particles. See text for description of the ACM desorption mode.

Table 3.2: Overview of the ACM collection and desorption periods for different experiments. Shown are experiment date, experiment temperature, name of the respective ACM period, start and end time of ACM sampling.

Date	T_{exp} in [K]	Notation	Collection start	Collection end
2009/11/16	303	ACM16.1	11:37	14:14
		ACM16.2	16:35	18:39
2009/11/17	273	ACM17.1	11:09	14:11
		ACM17.2	16:48	17:13
2009/11/18	243	ACM18.1	11:24	14:02
		ACM18.2	16:37	18:37
2009/11/19	273	ACM19.1	10:58	11:55
		ACM19.2	12:42	14:35
		ACM19.3	16:42	17:19
		ACM19.4	17:44	19:09
2009/11/20	258	ACM20.1	12:13	14:08
		ACM20.2	16:17	18:32
2009/11/25	258	ACM25.1	11:54	14:24
		ACM25.2	15:25	16:28
2009/11/26	273	ACM26.1	13:25	16:29
2009/11/27	273	ACM27.1	10:30	13:37

3.3 Experimental Conditions and Procedure

All experiments were conducted under ambient pressure (~ 1000 mbar). Relative humdity ranged between 30 to 80 %. To ensure pure ozonolysis reactions, high concentrations (~ 500 ppm) of cyclohexane (99.5 %, Merck) were used as scavenger for OH-radicals generated during the ozonolysis reactions (Saathoff et al., 2009). Except for one α-pinene ozonolysis experiment at 243 K, all other experiments started with the addition of cyclohexane by flushing 9 l synthetic air per minute over a saturator. Afterwards, ozone, which was generated by a silent discharge generator (Semozon 030.2, Serbios), was either injected directly or after dilution in a 1 l glass vessel with a flow of 5 l per minute of synthetic air. A detailed day-to-day routine of all experiments can be found in the appendix A.

Table 3.3: Overview of the ACM collection times (t_{ACM}), sampling flows (f_{ACM}), desorption time lengths (t_{PTR}) in which the PTR-ToF-MS measured from the ACM, and desorption temperatures (T_{des}) for the different ACM periods. The desorption temperature was at 463 K in all desorption processes. The PTR-ToF-MS sampled with a flow of 380 $\frac{ml}{min}$

Notation	t_{ACM} in [min]	f_{ACM} in [ml m^{-1}]	t_{PTR} in [min]
ACM16.1	157	84.00	6
ACM16.2	124	84.00	6
ACM17.1	183	84.00	6
ACM17.2	25	84.00	6
ACM18.1	158	84.60	6
ACM18.2	120	84.60	5
ACM19.1	57	84.60	12
ACM19.2	113	84.60	6
ACM19.3	37	84.60	6
ACM19.4	85	85.20	8
ACM20.1	55	84.60	7
ACM20.2	136	85.20	9
ACM24.1	180	84.60	10
ACM25.1	150	84.00	10
ACM25.2	63	84.00	6
ACM26.1	65	83.40	10
ACM27.1	188	82.80	10

3.3.1 β-pinene ozonolysis experiments

β-Pinene ozonolysis experiments were conducted at 243 K, 258 K, 273 K, and 303 K. For these experiments β-pinene (99 %, Aldrich) was evaporated at a pressure of 2 mbar into a 2 l glass vessel and injected into the chamber with 10 l min^{-1} of synthetic air. An additional injection of $\sim$ 20 ppb nopinone (98 %, Aldrich), as the major β-pinene ozonolysis product, was conducted for reference purposes at points where the major content of the reactants was assumed to have been consumed. Therefore, 8 l min^{-1} of synthetic air was flushed over a saturator containing nopinone at 50 °C. An overview of the β-pinene ozonolysis experiments is given in Table 3.4. Figure 3.6 shows a β-pinene ozonolysis experiment at 273 K as an example for the general β-pinene ozonolysis experiment procedure. The PTR-ToF-MS data of the development of the β-pinene parent ion $C_{10}H_{17}^+$ is shown in green. The development of the nopinone parent ion $C_9H_{15}O^+$ is shown in black. Fragments of β-pinene and

Table 3.4: Overview of the β-pinene ozonolysis experiments.

Date	T_{exp} in [K]	Added compound	Mixing ratio in [ppb]
2009/11/16	303	Cyclohexane	~ 500
		Ozone	530
		β-pinene	49
		Nopinone	20
		Ozone	1000
		β-pinene	49
2009/11/17	273	Cyclohexane	~ 500
		Ozone	710
		β-pinene	44
		Ozone	970
		Nopinone	20
		Ozone	4000
		β-pinene	44
2009/11/18	243	Cyclohexane	~ 500
		Ozone	830
		β-pinene	39
		Ozone	2000
		Nopinone	20
		Ozone	2000
		β-pinene	39
2009/11/25	258	Cyclohexane	~ 500
		Ozone	850
		β-pinene	41.4
		Nopinone	20
2009/11/27	273	Cyclohexane	~ 500
		Ozone	900
		β-pinene	44

nopinone are not included in this picture (see chapter 4.3). In this experiment β-pinene was added twice. There was one additional nopinone injection. The areas marked in pink show the times when the filter between the PTR-ToF-MS and the AIDA chamber was bypassed. In this period, the PTR-ToF-MS was assumed to measure the whole aerosol phase. Areas in blue indicate the ACM sampling times. ACM sampling continued during the PTR-ToF-MS measurement with and without filter. Highlighted in yellow are the periods for ACM desorption. At that times, the PTR-ToF-MS measured

the evaporated compounds of the aerosol particle phase from the ACM. For times that are highlighted neither in pink, nor in yellow the PTR-ToF-MS measured from the AIDA chamber with particle filter in the sampling line. So, only the gas phase is detected by the PTR-ToF-MS in this periods.

Figure 3.6: β-pinene ozonolysis experiment at 273 K. The green line shows the mixing ratio of the β-pinene parent ion $C_{10}H_{17}{}^+$. The black line shows the mixing ratio of the nopinone parent ion $C_9H_{15}O^+$. The shaded areas mark periods of measurement without filter (pink), ACM sampling (blue), measurement without filter and ACM sampling at the same time (violet), and ACM measurement periods (yellow). See text for a detailed description.

3.3.2 α-pinene ozonolysis experiments

An overview of the α-pinene ozonolysis experiments is given in Table 3.5. They were carried out at 243 K, 258 K, and 273 K. α-Pinene was evaporated at a pressure of 2 hPa into a 1 l glass vessel and afterwards injected into the chamber with 10 l min^{-1} of synthetic air. In the experiment at 258 K, pinonaldehyde, as a major α-pinene ozonolysis product, was added by flushing 8 l min^{-1} of synthetic air over a saturator containing pinonaldehyde at 65 °C.

Figure 3.7 shows the development of the α-pinene parent ion $C_{10}H_{17}^+$ at 273 K as a representative of the α-pinene ozonolysis experiments. Two α-pinene additions were conducted in this experiment. The major α-pinene ozonolysis product pinonaldehyde is in the particle phase at temperatures below 273 K. Therefore, it is not included in this Figure. A detailed analysis of pinonaldehyde in the α-pinene ozonolysis experiments is given in chapter 5.1.1. The different measurement and sampling modes are highlighted as in the β-pinene ozonolysis experiments, pink for PTR-ToF-MS measurements without filter, blue for ACM collection times, violet for PTR-ToF-MS measurement and concurrent ACM sampling, and yellow for ACM desorption measurements.

Table 3.5: Overview of the α-pinene ozonolysis experiments.

Date	T_{exp} in [K]	Added compound	Mixing ratio in [ppb]
2009/11/20	258	Cyclohexane	~ 500
		Ozone	333
		α-pinene	4
		α-pinene	21
		Nopinone	20
		Pinonaldehyde	
2009/11/26	273	Cyclohexane	~ 500
		Ozone	310
		α-pinene	5.5
		α-pinene	22

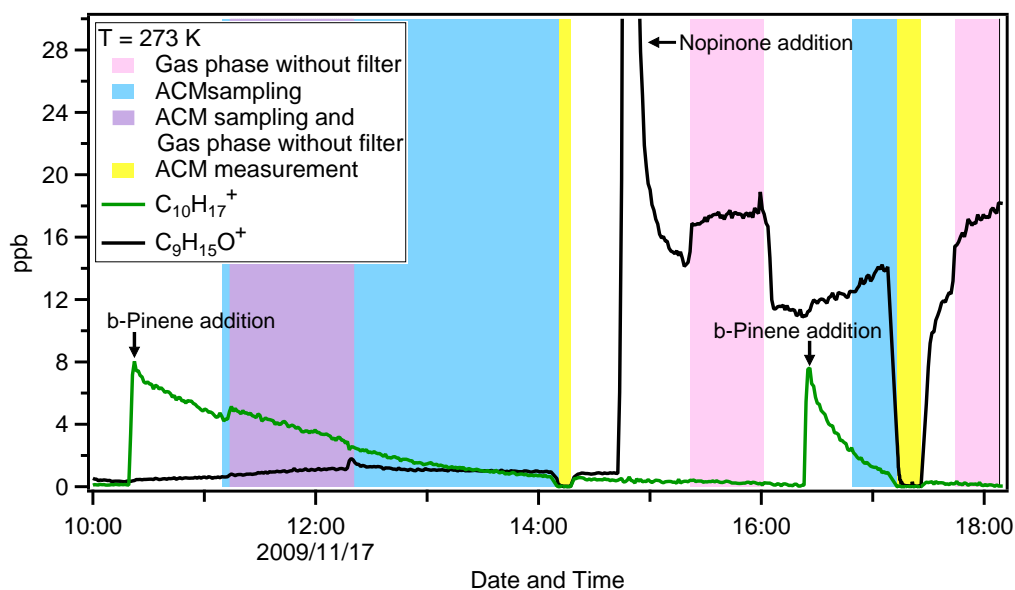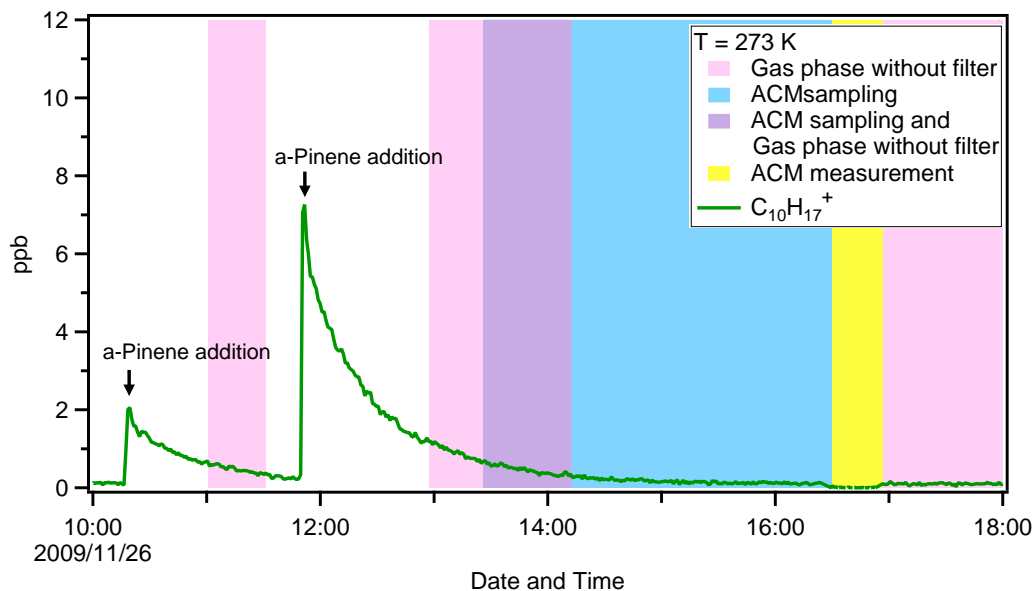Figure 3.7: α-pinene ozonolysis experiment at 273 K. The green line shows the mixing ratio of the α-pinene parent ion $C_{10}H_{17}{}^{+}$. The measurement and sampling modes are highlighted as in the β-pinene ozonolysis experiments. Pink areas: PTR-ToF-MS measurements without filter; blue areas: ACM collection times; violet areas: PTR-ToF-MS measurement and concurrent ACM sampling; yellow areas: measurements from the ACM.

3.3.3 Nopinone experiment

In addition to the ozonolysis experiments, where the formation of secondary organic aerosol from the reaction of α-pinene and β-pinene with ozone was investigated, one experiment at 273 K included only the addition of nopinone as the major β-pinene ozonolysis product (see Figure 3.8). The experimental procedure of this experiment can be seen in Table 3.6. This measurement was used in this work as a reference and for the investigation of the nopinone fragmentation in the PTR-ToF-MS (see chapter 4.3.4). The colored highlights refer to the measurement and collection modes same as in the α-pinene and β-pinene ozonolysis experiments (pink: PTR-ToF-MS measurement without filter; blue: ACM sampling; violet: PTR-ToF-MS measurement without filter and concurrent ACM sampling; yellow: ACM measurement). Due to data acquisition problems there was no data available from 14:53 on.
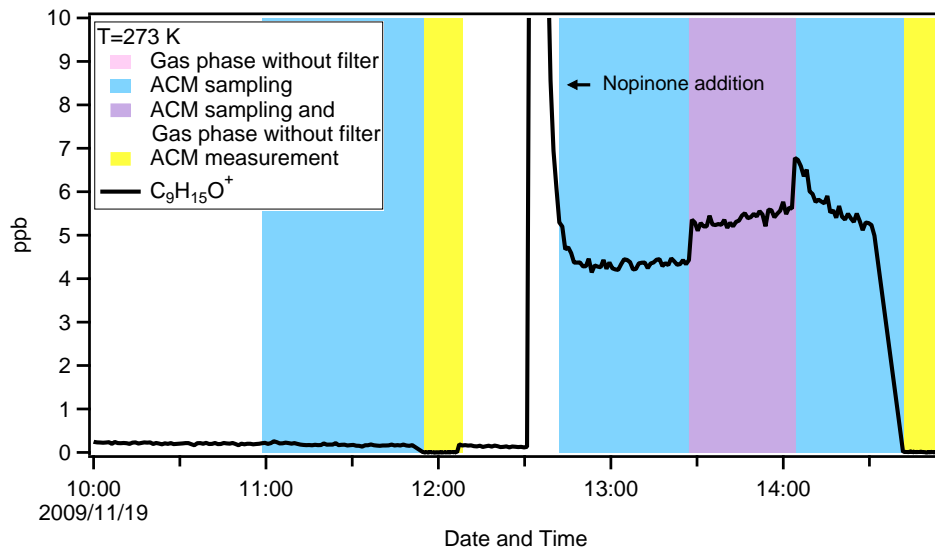
Figure 3.8: Nopinone experiment at 273 K. The black line shows the mixing ratio of the nopinone parent ion $C_9H_{15}O^+$. Colored areas mark PTR-ToF-MS measurement without filter(pink), ACM sampling (blue), PTR-ToF-MS measurement without filter and concurrent ACM sampling (violet), and ACM measurement (yellow).

Table 3.6: Overview of the nopinone experiment.

Date	T_{exp} in [K]	Added compound	Mixing ratio in [ppb]
2009/11/19	273	Ozone	940
		Nopinone	20
		Ozone	1000

Chapter 4

Procedures of data analysis

In this chapter the procedures of data analysis are explained in detail. The method to determine the mixing ratios from the PTR-ToF-MS data is presented, as well as the calibration of the PTR-ToF-MS. An analysis of the fragmentation in the PTR-ToF-MS drift tube is presented for β-pinene, α-pinene, and nopinone. Furthermore, details on the determination of the partitioning coefficient from PTR-ToF-MS measurements with and without particle filter, and from the coupling of the PTR-ToF-MS with the ACM are given.

4.1   Determination of the mixing ratios

To determine the mixing ratio in ppb from the data supplied by the PTR-ToF-MS, Equation 4.1 is applied to the signal of the respective ion.

$$C_{ppbV} = \underbrace{1.657 \cdot 10^{-11} \frac{U_{drift} T_{drift}^2}{k \cdot p_{drift}^2} \cdot \frac{C^+}{H_3O^+} \cdot \frac{TR_{H_3O^+}}{TR_{C^+}}}_{(I)} \cdot CF \cdot FF \qquad (4.1)$$

C_{ppbV} Mixing ratio of a compound in $[ppb]$

U_{drift} Voltage in the PTR-ToF-MS drift tube in $[V]$

T_{drift} Temperature in the PTR-ToF-MS drift tube in $[K]$

k Reaction rate of the specific ion with H_3O^+ in $\left[\dfrac{cm^3}{s}\right]$

     (see Table 4.1)

p_{drift} Pressure in the PTR-ToF-MS drift tube in $[mbar]$

C^+ Concentration of the specific ion

     from the PTR-ToF-MS signal in $\left[\dfrac{1}{s}\right]$

H_3O^+ Concentration of the primary ion H_3O^+

     from the PTR-ToF-MS signal in $\left[\dfrac{1}{s}\right]$

TR_{C^+} Transmission of the specific ion   (see section 4.2)

$TR_{H_3O^+}$ Transmission of the primary ion H_3O^+ (see section 4.2)

FF Fragmentation factor of the

     respective compound (see section 4.3)

CF Calibration factor (see section 4.2)

$1.657 \cdot 10^{-11}$ Constant factor from standard conditions

     and device-specific values (see text for details)

The basic part of the equation is taken from Ionicon and consists of a combination of standard conditions (namely $p_0 = 1013.25$ mbar for air pressure, $T_0 = 273.15$ K for temperature, $2.8\frac{cm^2}{Vs}$ for reduced mobility parameter μ_0) and device-specific values (like drift tube length of 9.3 cm) leading to part (I) of Equation 4.1.

The reaction rates k used in this work are taken from Zhao and Zhang (2004) and Tani et al. (2003). For compounds, for which no reaction rate could be found in literature, the functional group of the specific compound was considered and reaction rates of comparable compounds ware taken from Zhao and Zhang (2004) and Tani et al. (2003). The reaction rates used in this work are given in Table 4.1. For compounds not listed in Table 4.1 a reaction rate of $k \approx 2 \cdot 10^{-9}\frac{cm^3}{s}$ was assumed as a typical reaction rate.

Table 4.1: Reaction rates (k) used in this work. [†] Zhao and Zhang (2004), [‡] Tani et al. (2003)

Compound	k in $[10^{-9}\frac{cm^3}{s}]$
Benzene	1.97 [†]
Toluene	2.12 [†]
Ethylbenzene	2.25 [†]
a-Pinene	2.44 [†]
b-Pinene	2.50 [†]
Nopinone	4.40 [‡]

One of the aims of the experiments presented in this work was to find β-, and α-pinene ozonolysis products. These are not well-known so far. There-fore, it was not possible to use an absolute calibration, i.e. a calibration for all compounds which are expected to be measured. Thererfore, the PTR-ToF-MS data is processed with a device- and ion-specific transmission factor, as all measured ions have different transmission efficiencies in the PTR-ToF-MS. The transmission factors used in this work are based on a nonlinear, ex-perimental transmission curve provided by the PTR-ToF-MS manufacturer Ionicon. As the originally provided values did not contain all m/z needed for the data analysis of this work, additional values had to be extrapolated. The transmissions used in this work are displayed in Table 4.2. The original transmission values provided by Ionicon are highlighted in bold black.

Equation 4.1 is adjusted to the conducted experiments by including cali-bration factor CF and a fragmentation factor FF. The calibration factor is determined via the calibration with a BTX-standard conducted at the AIDA chamber. A description on its determination can be found in section 4.2. The fragmentation factor FF is determined for β-pinene, nopinone and α-pinene in this work (see section 4.3).

Table 4.2: Transmission of ions at different m/z in the PTR-ToF-MS

m/z	Transmission	m/z	Transmission
21	**0.033**	94	0.689
32	0.0485	95	0.7
33	0.05	96	0.707
37	0.1	**105**	**0.768**
39	0.117	**107**	**0.763**
40	0.126	109	0.782
53	0.238	**113**	**0.821**
54	0.247	**121**	**0.887**
59	0.29	122	0.889
67	0.4	123	0.891
69	0.4	135	0.916
79	**0.5**	136	0.918
80	0.505	137	0.92
81	0.51	138	0.92
82	0.525	139	0.92
83	0.54	140	0.921
84	0.548	**147**	**0.931**
91	0.601	**149**	**0.958**
92	0.609	155	0.966
93	**0.677**	**181**	**1**

4.2 Calibration

The PTR-ToF-MS was calibrated with a BTX-standard (National Physical Laboratory) containing benzene, toluene, ethyl-benzene, m-, p-, and o-xylene (see Table 4.3). Ethyl-benzene, m-, p-, and o-xylene all appear on the same m/z in the PTR-ToF-MS signal. This standard of aromatic compounds was chosen due to the fact that the signals and fragment signals do not show many interferences. Therefore, they lead to a clear calibration signal. In addition, the contained compounds were also part of the transmission curve provided by the manufacturer Ionicon (see section 4.1). The calibration measurements for the experiments of 2009/11/16 - 2009/11/27 were conducted on 2009/11/16, /17, /20, /23, and /26. For this purpose, the connection between the PTR-ToF-MS and the AIDA chamber was closed and the connection to the optional BTX-standard and synthetic air supply was opened (see Figure 3.2). The calibration procedure consisted of a 10 min measurement of the BTX-standard, followed by 10 min of synthetic air

Table 4.3: BTX-standard certified mixing ratios, m/z at which the ions are detected in the PTR-ToF-MS, and parent ion identification. Note that ethyl-benzene, m-, p-, and o-xylene are all detected on $C_8H_{11}^+$ at m/z 107.086.

Species	Mixing ratio in [ppb]	Detected on m/z	Parent ion identification
Benzene	9.8 ± 0.3	79.055	$C_6H_7^+$
Toluene	9.9 ± 0.3	93.070	$C_7H_9^+$
Ethyl-benzene	10.0 ± 0.3		
m-xylene	9.8 ± 0.3	107.086	$C_8H_{11}^+$
p-xylene	9.9 ± 0.3		
o-xylene	9.9 ± 0.3		

for a background determination, which was subtracted from the signal for the BTX-ions. For each BTX-compound, the measured BTX-value in ppb was calculated with part (I) of Equation 4.1, taking the fragmentation of the BTX-compounds in the PTR-ToF-MS into account. The factors between the determined BTX-measurement values and the BTX-values given in the standard were evaluated for each BTX-compound (Table 4.4).

Table 4.4: BTX-compounds, m/z where the ions are detected in the PTR-ToF-MS and expected amount in ppb on the respective m/z, taking into account that under the existing drift tube conditions 30% of the signal expected at m/z 107.086 is measured on m/z 79.055. The last column shows the deviation from the expected value in %.

Species	detected on m/z	expected ppb	calculated ppb	deviation from expected value in %
Benzene	79.055	12.8	19.2	50
Toluene	93.070	9.9	9.1	8
Ethyl-benzene				
m-xylene	107.086	36.6	32.8	10
p-xylene				
o-xylene				

These factors were used to determine a linear, m/z-dependent calibration curve (see Figure 4.1) following the linear equation

$$CF(m/z) = (1 - 21 \cdot b) + b \cdot m/z \tag{4.2}$$

CF is the calibration factor, m/z the mass to charge ratio and b the slope of the calibration curve ($b = 0.03062 \pm 0.00471$).
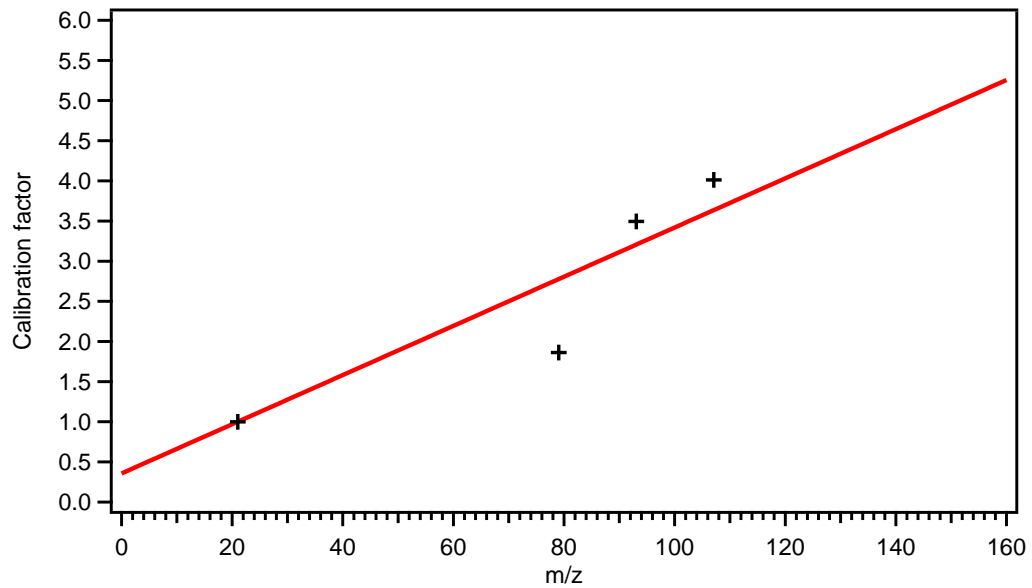
Figure 4.1: BTX-calibration curve

As every ion has to be multiplied with its m/z-respective calibration factor resulting from Equation 4.2 to determine its mixing ratio in ppb, the calibration function was integrated into the equation determining the mixing ratio (see section 4.1). It is assumed that the calibration factor for H_3O^+ at m/z 21 is 1. This assumption had to be made to allow the calculation of the measured mixing ratios of the BTX-values in ppb. It is pursued in the calibration function as a matter of consistency.

If considering the role of the calibration function in Equation 4.1, it can be interpreted as a correction of the transmission curve, which is described in section 4.1. Therefore, the calibrated transmission curve can be derived by dividing the transmission TR_{C^+} with the calibration factor CF for the respective m/z. The resulting transmission can be seen in Figure 4.2.
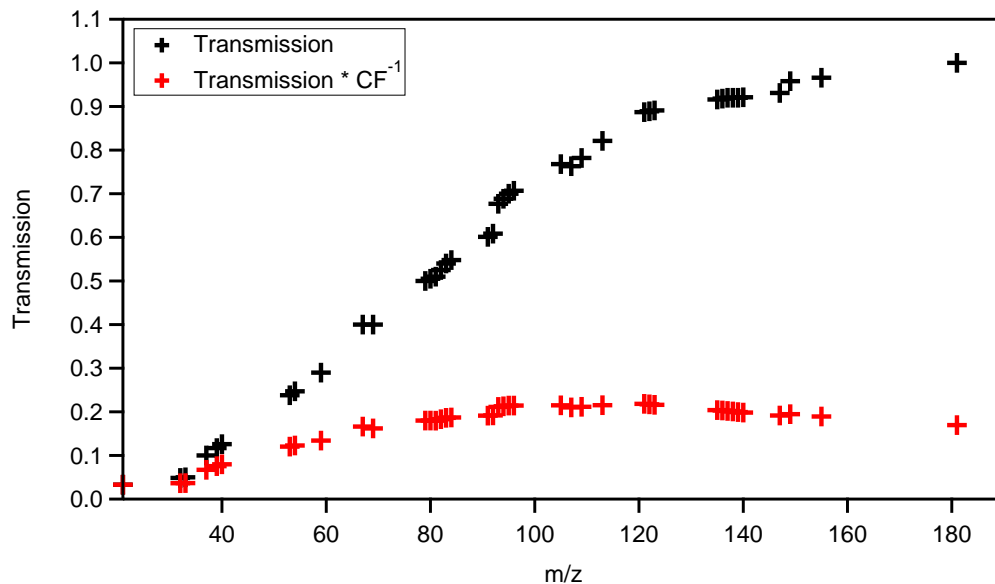
Figure 4.2: Original transmission curve (black) and transmission after processing with the BTX-calibration curve (red).

It has to be mentioned that a transmission curve determined from the PTR-ToF-MS at the AIDA chamber would have been preferable to the one provided by Ionicon and applying the described correction curve. Moving the instrument can result in slight changes in the transmission referring to the manufacturer. As in the present work, the PTR-ToF-MS was transported to the AIDA chamber, a change in the transmissions can be expected. The determation of a new transmission curve after setting the instrument up at a new measurement site is recommended. However, the three BTX-signals are not sufficient to determine a new transmission curve. Nevertheless, changes in the transmission can be covered by applying the calibration curve to Equation 4.1.
A measure of quality for the calibration curve can be derived from comparing the BTX-measurements determined with the calibration curve to the expected BTX-values from the standard (see Table 4.4). The deviations of the calculated amounts to the expected amounts of the BTX-compounds lie between 8 % (for toluene) and 50 % (for benzene). As ethyl-benzene, m-, p- and o-xylene add up on m/z 107.086 the deviation of the sum of the expected amount can be calculated. It lies at 10 %. This 10 % are in good agreement with the 8 % deviation for toluene. Although the behavior of benzene could well be interpreted as a spike, the sparsity of reference values does not al-

low to exclude benzene from the measure of quality of the calibration curve. Therefore, a systematic error from the calibration has to be considered to lead to ppb-values with an uncertainty of up to 50 % of the respective value. Note that this does not result in a variation of the mixing ratio of a compound within a 50 % range. The 50 % have rather to be considered as a possible constant offset for the mixing ratio of each compound.

4.3 Fragmentation

As described in section 2.1.2 compounds measured in the PTR-ToF-MS undergo fragmentation during their ionization process in the PTR-ToF-MS drift tube. To derive information about the amount of the original compound in a sample, the fragmentation of this compound at the experiment-specific drift tube conditions has to be determined. The fragmentation of a compound is the same for all experiments if the drift tube conditions are kept constant. Thus, fragments are linear correlated to each other. A measure for linear correlation is provided by the Pearson product-moment correlation coefficient r, or short Pearson correlation coefficient, developed by Pearson and Bravais (see Equation 4.3 (Hartung et al., 2009).

$$r = \frac{\sum_{i=1}^{n}(x_i - \bar{x})(y_i - \bar{y})}{\sqrt{\sum_{i=1}^{n}(x_i - \bar{x})^2 \cdot \sum_{i=1}^{n}(y_i - \bar{y})^2}} \tag{4.3}$$

The correlation coefficient r displays the linear correlation of an ion x at point i in a chosen time interval to an ion y at the same point i for all n values in the chosen time interval. r has values in the range of $-1 \leq r \leq 1$ with the following interpretation:

$\mathbf{r = 1}$	The signals of two ions are linear correlated.
$\mathbf{r = 0}$	The signals of two ions are not linear correlated.
$\mathbf{r = -1}$	The signals of two ions are linear anti-correlated.

Values between 0 and ± 1 can be considered more correlated/anti-correlated the closer the are to ± 1.
In this work, the fragmentation of the compounds was determined from the experimental data taken at the AIDA chamber. As mentioned above, no absolute calibration was conducted. Therefore, experiment periods had to

be chosen, in which only the respective compound was added to the chamber to keep the data as simple as possible. The chosen time intervals in the PTR-ToF-MS data include the injection of the compound under investigation to show a distinct variation of the signal of the compound in time. Only ions which follow the course of the compound under investigation will show a linear correlation to this compound. To derive information about the fragmentation of a compound in the PTR-ToF-MS drift tube one needs the signal of at least one certain identified ion which originates from the species under investigation. In the present work, α -, β -pinene, and nopinone fragmentation were determined. For these compounds, the respective parent ion could be used as certain identified ion in the matrix correlation.

In a first step, the PTR-ToF-MS raw signal of all ions between m/z 28 and m/z 172 is determined. Within this range, ion identity was defined (see section 2.1.4) and it was reasonable for consideration in the context of fragmentation identification. Following that, a correlation matrix determining the Pearson correlation coefficient is applied. It results in a matrix of the correlation coefficients for all compounds with each other within the specified mass range and time interval (see see appendix B). Due to the complex PTR-ToF-MS high resolution data this first step of raw data procession was used to filter for potential fragments of the compound under investigation. Therefore, an empirical threshold of $|r| = |0.6|$ was chosen. Ions showing a correlation coefficient higher than +0.6 were considered potential fragments of a specific compound and were further investigated. As an excerpt of the correlation matrix Figure 4.3 shows the correlation coefficients for compounds between m/z 37 and m/z 172 with $C_{10}H_{17}^+$ for the β-pinene fragmentation investigation.

For further investigations the potential fragment signals are processed with Equation 4.4, which is similar to part (I) combined with the calibration factor CF of Equation 4.1 but without including the reaction rate k. This was done to normalize the raw signal on the primary ion H_3O^+ and on the conditions in the PTR drift tube. It also takes into account the transmission in the PTR-ToF-MS. For fragments the reaction rate which has to be considered is the one of the respective parent ion with H_3O^+. At this point of the investigation, it is not known whether a specific ion is a fragment or not. So, a reaction rate cannot be assumed and is, therefore, not included in Equation 4.4.

$$C_{bK} = 1.657 \cdot 10^{-11} \frac{U_{drift} T_{drift}^2}{p_{drift}^2} \cdot \frac{C^+}{H_3O^+} \cdot \frac{TR_{H_3O^+}}{TR_{C^+}} \cdot CF \qquad (4.4)$$

55
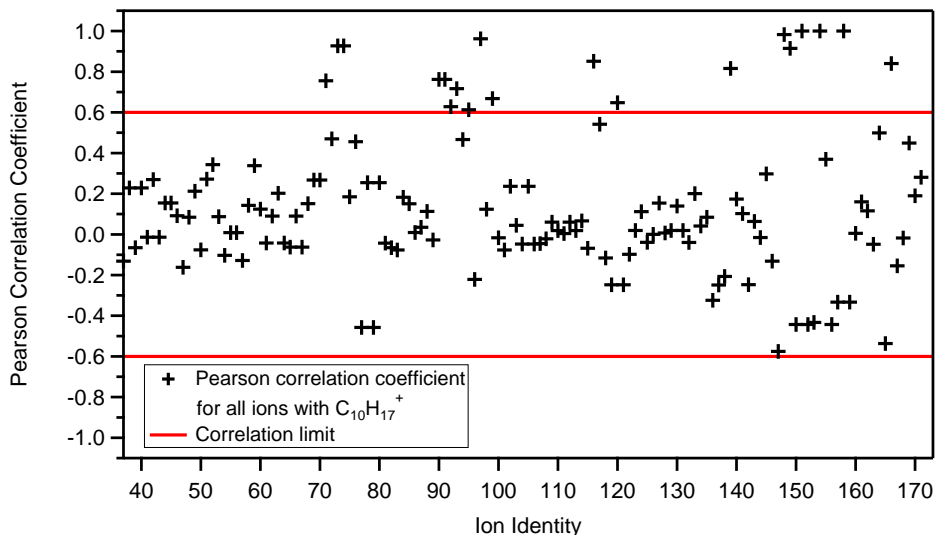
Figure 4.3: Pearson correlation coefficient for all ions in the mass range between m/z 37 and m/z 172 for β-pinene parent ion $C_{10}H_{17}^+$. The red lines indicate the threshold of significant correlation. A list of the ion identities can be found in the appendix (see Table C.1)

C_{bK}	Ion signal before applying a reaction rate
U_{drift}	Voltage in the PTR-ToF-MS drift tube in V
T_{drift}	Temperature in the PTR-ToF-MS drift tube in K
p_{drift}	Pressure in the PTR-ToF-MS drift tube in $mbar$
C^+	Concentration of the specific ion
	from the PTR-ToF-MS signal
H_3O^+	Concentration of the primary ion H_3O^+
	from the PTR-ToF-MS signal
TR_{C^+}	Transmission of the specific ion (see section 4.2)
$TR_{H_3O^+}$	Transmission of the primary ion H_3O^+ (see section 4.2)

After applying Equation 4.4, the correlation matrix is applied a second time. By this, correlations due to e.g. spikes from pressure changes, which could be seen at injection times in AIDA, are ruled out. Ions which appeared to be linear correlated to the parent ion of the compound under investigation after the second matrix processing were plotted against the parent ion. From the slope of the linear fits of those plots the percentage of the respective fragment

of the investigated compound can be derived under the assumption that all fragments are found in the process described above. For this, Equation 4.5 is applied.

$$F_j^+ = \frac{100}{\sum_j^m s_{f,j}} \cdot s_{f,j} \qquad (4.5)$$

F_j^+ Percentage of fragment j
of the total compound signal

$s_{f,j}$ slope of fragment j plotted
against the respective parent ion

where j is the run index for all m identified fragments.

During the experiments, there is always the possibility that other compounds in the sample produce an unexpected interfering signal or fragment signal on one or more fragments of the investigated compound. Therefore, summing the signals of the fragments up does not necessarily lead to the total compound signal. In this work the raw data showed no interfering signals on the positive ions of α-pinene , β-pinene and nopinone. Hence, the factor for the percentage of the parent ion ($F_{parent\ ion}^+$) to the total compound signal (equal 100 %) was calculated as a fragmentation factor FF.

$$FF = \frac{100}{F_{parent\ ion}^+} \qquad (4.6)$$

To finally determine the mixing ratio of a compound, the fragmentation factor is included into Equation 4.1.

4.3.1 β-Pinene Fragmentation

The fragmentation for the β-pinene experiments shown in this work is derived from the β-pinene ozonolysis experiment on 2009/11/17 for the time interval between 10:00:52 and 14:02:32 and all ions between m/z 28 and m/z 172. The time intervall is chosen to be at the beginning of the experiment. Therefore, it includes only the first β-pinene addition to the chamber in the presence of ozone. This is done to keep the mass spectra as simple as possible and to ensure potentially interfering signals from other compounds as low as possible. Figure 4.3 shows an excerpt of the correlation of all ions to β-pinene parent ion $C_{10}H_{17}^+$ derived from the matrix of correlation coefficients

for all ions correlated with each other. The resulting relative contributions of individual ions to the β-pinene signal can be found in Table 4.5. It shows the masses of the ionized compounds which are identified as β-pinene fragments and their percentages of the total β-pinene signal. It also shows the Pearson correlation coefficients of the respective fragment with $C_{10}H_{17}^+$ derived from the correlation matrix, as well as the neutral fragments which are abstracted during the ionization process in the PTR-ToF-MS drift tube.

Table 4.5: Fragmentation of β-pinene as calculated from Equation 4.5.

Mass [amu]	Ion	Pearson correlation coefficient	Neutral fragment	Percentage of the total β-pinene signal [%]
79.055	$C_6H_7^+$	0.67	C_4H_{10}	2.22 ± 0.17
81.070	$\mathbf{C_6H_9^+}$	0.93	C_4H_8	$\mathbf{51.33 \pm 2.43}$
82.074	$^{13}CC_5H_9^+$	0.93	C_4H_8	3.28 ± 0.16
93.070	$C_7H_9^+$	0.72	C_3H_8	1.96 ± 0.13
95.086	$C_7H_{11}^+$	0.96	C_3H_6	5.50 ± 0.15
96.089	$^{13}CC_6H_{11}^+$	0.67	C_3H_6	0.45 ± 0.03
135.117	$C_{10}H_{15}^+$	0.98	H_2	1.59 ± 0.04
137.133	$\mathbf{C_{10}H_{17}^+}$	1.00	-	$\mathbf{29.70 \pm 0.65}$
138.136	$^{13}CC_9H_{17}^+$	1.00	-	3.24 ± 0.07
140.120	$C_9H_{16}O^+$	1.00	CO	0.16 ± 0.003
155.107	$C_9H_{15}O_2^+$	0.84	CH	0.57 ± 0.03

The two major contributors to the β-pinene signal are the parent ion $C_{10}H_{17}^+$ with 29.70 ± 0.65 % on mass 137.133 amu, and the fragment $C_6H_9^+$ with 51.33 ± 2.43 % on mass 81.070 amu. Other than $C_9H_{16}O^+$ and $C_9H_{15}O_2^+$, all ionized and neutral fragments are the results of the reaction of $C_{10}H_{16}$ with H_3O^+. The fragments identified as $C_9H_{16}O^+$ on m/z = 140.120 and $C_9H_{15}O_2^+$ on m/z = 155.107 are very likely the outcome of an ionization of $C_{10}H_{16}$ with O_2^+ instead of H_3O^+. The ionization of $C_{10}H_{16}$ with O_2^+ leads, therefore, to the attachment of O^+ and the separation of CO in the case of $C_9H_{16}O^+$. In the case of $C_9H_{15}O_2^+$ O_2^+ is attached to $C_{10}H_{16}$ and CH is left as neutral fragment. Although the Pearson correlation coefficient equals one in the case of $C_9H_{16}O^+$, which is highly linear correlated to β-pinene , the percentage of the total β-pinene signal is comparably low. The sum of both fragments from ionization with O_2^+ account for less than 1 % of the total β-pinene signal. This is due to the fact that H_3O^+ is the major primary ion

in this experiment. Thus, it confirms that O_2^+ reactions in the drift tube are subordinate to ionizations with H_3O^+. As the PTR-ToF-MS leaves the opportunity to switch to O_2^+ as primary ion, it can be concluded that $C_9H_{16}O^+$ and $C_9H_{15}O_2^+$ will be major β-pinene fragments under that conditions.

To rule out interferences on the β-pinene fragment signals, the total β-pinene signal is not calculated as the sum of the fragments throughout the experiments, but by multiplication of the $C_{10}H_{17}^+$ signal with the fragmentation factor, which is derived from the percentage of the $C_{10}H_{17}^+$ signal of the total β-pinene signal following Equation 4.6. The β-pinene fragmentation factor is calculated to be 3.37 ± 0.07. A comparison of the β-pinene fragmentation to the α-pinene fragmentation and to literature can be found in section 4.3.3.

4.3.2 α-Pinene Fragmentation

The α-pinene fragmentation in the PTR-ToF-MS drift tube is determined from the data taken on 2009/11/26 between 10:00:02 and 16:22:05. Thus, it includes both α-pinene additions. A significant variation in the α-pinene signal, as needed for a clear identification of fragments with the correlation matrix, is therefore ensured. The resulting fragmentation can be seen in Table 4.6.

Table 4.6: Fragmentation of α-pinene as calculated from Equation 4.5.

Mass [amu]	Ion	Pearson correlation coefficient	Neutral fragment	Percentage of the total α-pinene signal [%]
81.070	$\mathbf{C_6H_9^+}$	0.94	C_4H_8	$\mathbf{47.82 \pm 1.38}$
82.074	$^{13}CC_5H_9^+$	0.94	C_4H_8	3.06 ± 0.09
92.063	$C_7H_8^+$	0.68	C_3H_9	0.38 ± 0.02
95.086	$C_7H_{11}^+$	0.87	C_3H_6	4.74 ± 0.15
135.117	$C_{10}H_{15}^+$	0.84	H_2	0.66 ± 0.02
137.133	$\mathbf{C_{10}H_{17}^+}$	1.00	-	$\mathbf{38.32 \pm 0.48}$
138.136	$^{13}CC_9H_{17}^+$	1.00	-	4.18 ± 0.05
140.120	$C_9H_{16}O^+$	1.00	CO	0.200 ± 0.003
155.107	$C_9H_{15}O_2^+$	0.66	CH	0.64 ± 0.04

The identified fragments with masses up to 138.136 amu result from reactions of α-pinene with H_3O^+. This reaction leads to the PTR-ToF-MS signal of the respective ion, as well as to the neutral fragments listed in Table 4.6. In analogy to β-pinene, the fragments $C_9H_{16}O^+$ and $C_9H_{15}O_2^+$ are resulting from a reaction with O_2^+, which is competing with H_3O^+ as a primary

ion. Nevertheless, the low signal of these two compounds, accounting for less than 1 % of the total α-pinene signal, shows that the reaction with O_2^+ is subordinate to the reaction with H_3O^+ (see Appendix E.) A comparison to β-pinene fragmentation and to literature can be found in section 4.3.3.

In analogy to the β-pinene fragmentation, the fragmentation factor FF is calculated for the α-pinene parent ion $C_{10}H_{17}^+$. To exclude the possibility of interfering signals on one or more of the fragment signals, the total α-pinene signal is calculated from the $C_{10}H_{17}^+$ signal times the fragmentation factor of 2.61±0.03 for all experiments (see Equation 4.6).

4.3.3 Comparison of β-pinene and α-pinene fragmentation to literature

A comparison to the results of Tani et al. (2003) shows that fragments at m/z 67, 81, 95 and 137 (identified as β-pinene , respectively α-pinene parent ion) have previously been reported for β-pinene and α-pinene fragmentation in a PTR-MS. Percentages from Tani et al. (2003) observed at 120 Td, in comparison to this work can be seen in Table 4.7. In comparison to the unit mass resolution data of a PTR-MS, the high mass resolution data of the PTR-ToF-MS allows to identify molecular formula of the respective fragment. These are also displayed in Table 4.7.

Table 4.7: Comparison of the α-pinene and β-pinene fragmentation with literature (Tani et al., 2003).

m/z	Percentage of the total monoterpene signal following Tani et al. (2003), at E/N = 120 Td	Percentage of the total monoterpene signal, this work, at E/N 154 Td	Identified fragment molecular formula
67	~1 %	-	-
81	40 %	48 % (α-pinene) 51 % (β-pinene)	$C_6H_9^+$
95	~1 %	5 % (α-pinene) 6 % (β-pinene)	$C_7H_{11}^+$
137	43-49 %	38 % (α-pinene) 30 % (β-pinene)	$C_{10}H_{17}^+$

Tani et al. (2003) investigated the of changes in the fragmentation due to changes in E/N (conducted between 80-120 Td). Percentages for signal on m/z 137 decrease, while percentages for fragments on m/z 95 and m/z 81 increase with increasing E/N. Therefore, lower percentages for $C_{10}H_{17}^+$ at E/N=154 (this work) and higher percentages for $C_6H_9^+$ and $C_7H_{11}^+$ are within good agreement with Tani et al. (2003). Although the fragment on m/z 67 also shows increasing behavior with increasing E/N in Tani et al. (2003), it could not be identified in the present work.

4.3.4 Nopinone fragmentation

For the determination of the nopinone fragments the PTR-ToF-MS data of 2009/11/19 was investigated. In that experiment, no α-pinene or β-pinene but only nopinone was added. Therefore, the correlation matrix to determine the Pearson correlation coefficient was used on the data of the whole experiment day. The ACM measurement periods were excluded to reduce the possibility of interfering signals that might occur due to molecules breaking up during ACM desorption. The resulting fragmentation can be seen in Table 4.8. It is more complex than the β-pinene and α-pinene fragmentation. Nevertheless, four major fragments could be determined. The nopinone parent ion $C_9H_{15}O^+$ on mass 139.112 shares 37.91 $\pm$ 0.12 % of the total nopinone signal. $C_9H_{13}^+$ on mass 121.102 shows 22.01 $\pm$ 0.25 %, $C_5H_7O^+$ on mass 83.050 has 12.46 $\pm$ 0.13 %, and $C_7H_9^+$ on mass 93.070 shares 7.48 $\pm$ 0.14 % of the total nopinone signal. All neutral fragments are determined under the assumption that they result from the ionization process $C_9H_{14}O$ with H_3O^+. A nopinone fragment on m/z 121 has been previously reported in literature (e.g. (Kim et al., 2010)). The fragmentation factor of $C_9H_{15}O^+$ from which the total nopinone signal is calculated is 2.64$\pm$0.01.

Table 4.8: Fragmentation of nopinone and percentages of the identified fragment compounds of the total nopinone signal.

Mass [amu]	Ion	Pearson correlation coefficient	Neutral fragment	Percentage of the total nopinone signal [%]
69.070	$C_5H_9^+$	0.96	C_4H_6O	2.36 ± 0.04
79.055	$C_6H_7^+$	0.95	C_3H_8	2.81 ± 0.05
80.063	$C_6H_8^+$	0.96	C_3H_7O	4.62 ± 0.08
81.070	$C_6H_9^+$	0.96	C_3H_6O	0.30 ± 0.01
83.050	$\mathbf{C_5H_7O^+}$	0.99	C_4H_8	$\mathbf{12.46 \pm 0.13}$
84.053	$^{13}CC_4H_7O^+$	0.99	C_4H_8	0.67 ± 0.01
93.070	$\mathbf{C_7H_9^+}$	0.95	C_2H_6O	$\mathbf{7.48 \pm 0.14}$
94.074	$^{13}CC_6H_9^+$	0.98	C_2H_6O	1.07 ± 0.01
94.078	$C_7H_{10}^+$	0.97	C_2H_5O	2.72 ± 0.04
95.086	$C_7H_{11}^+$	0.98	C_2H_4O	1.57 ± 0.02
95.050	$C_6H_7O^+$	0.96	C_3H_8	0.22 ± 0.004
96.058	$C_6H_8O^+$	0.98	C_3H_7	1.57 ± 0.02
121.102	$\mathbf{C_9H_{13}^+}$	0.98	H_2O	$\mathbf{22.01 \pm 0.25}$
122.105	$^{13}CC_8H_{13}^+$	0.98	H_2O	2.23 ± 0.02
139.112	$\mathbf{C_9H_{15}O^+}$	1.00	-	$\mathbf{37.91 \pm 0.12}$

4.4 Determination of the partitioning coefficient from a PTR-ToF-MS in a filter set-up

As described in chapter 3.2, the PTR-ToF-MS set-up at the AIDA chamber allowed measurements with and without particle filter in the sampling line. In this chapter, the determination of the partitioning coefficient from the comparison of the measurements with and without particle filter is described. A schematic of the set-up has been shown in Figure 3.2. During each experiment, the PTR-ToF-MS was switched several times between filtered and unfiltered sampling from the AIDA chamber. The basic assumption for this approach on deriving the partitioning coefficient was that during the measurements with particle filter the whole aerosol particle phase was removed from the sample. Thus, measurements only show aerosol gas phase in these periods. Second part of the basic assumption is that during the periods in which the particle filter was bypassed, the whole aerosol was measured by the PTR-ToF-MS. As the PTR-ToF-MS is a gas phase detector, the aerosol

particle phase had to be converted into the gas phase. This was realized by
the heated inlet line of the PTR-ToF-MS (see section 3.2.1). Following that,
the periods without particle filter in the sample line measure aerosol gas and
particulate phase. To gain aerosol particle phase information only, the gas
phase has to be subtracted from the data set of these periods. This approach
has previously been tested by Tillmann et al. (2010) with an identical set-up
for α-pinene ozonolysis experiments. Figure 4.4 shows an example for the
determination of the nopinone partitioning coefficient from PTR-ToF-MS
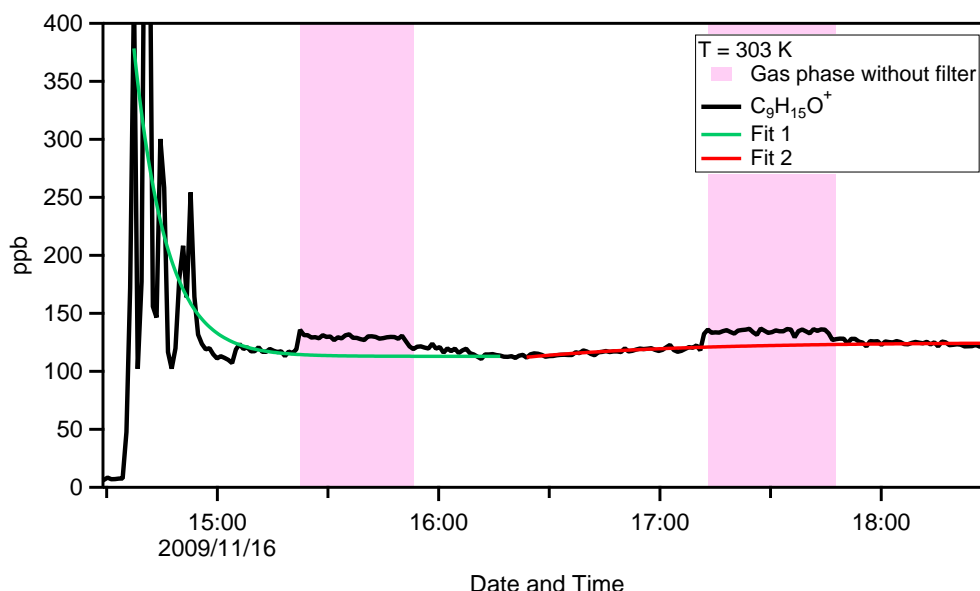measurements with and without filter.

Figure 4.4: Example for the determination of the partitioning coefficient from
PTR-ToF-MS measurements with and without filter. In black the mixing ratio of
the nopinone parent ion $C_9H_{15}O^+$ is shown during nopinone addition (14:34-14:57)
and two subsequent measurement periods without particle filter in the sampling
line (shaded in pink). The green line shows the nopinone gas phase fit, which
is needed to determine the gas phase mass concentration withing the first period
without filter. The red line shows the fit needed for the second period without
particle filter.

The partiotining coefficient is calculated from the experimental data fol-
lowing Equation 1.1.

$$K_{p,i} = \frac{C_{p,i}}{C_{g,i} \times C_{TSP}}$$

$K_{p,i}$ Equilibrium partitioning coefficient in $m^3 \cdot \mu g^{-1}$

$C_{p,i}$ Mass concentration of a species i in the aerosol particle phase per unit air volume in $\mu g \cdot m^{-3}$

$C_{g,i,}$ Mass concentration of a species i in the gas phase per unit air volume in $\mu g \cdot m^{-3}$

C_{TSP} Mass concentration of the total suspended mass of particles per unit air volume in $\mu g \cdot m^{-3}$

As in the present work, the nopinone partitioning coefficient is determined, species i in the equation is equal to nopinone. The mass concentration of the total suspended mass is provided by measurements from a Scanning Mobility Particle Sizer (SMPS), which was part of the standard instrumentation at the AIDA chamber. The ratio of particulate phase to gas phase was derived from the PTR-ToF-MS data. It is obvious that C_{TSP} and $\frac{C_{p,nopinone}}{C_{g,nopinone}}$ should be derived from the same time interval. In the periods without particle filter, the PTR-ToF-MS measured the whole aerosol phase. To get the mass concentration of nopinone in the gas phase in the periods without particle filter, a fit was applied to the gas phase data. An example for the gas phase fits can be seen in Figure 4.4. The green line shows the gas phase fit for the first period without filter. The red line shows the gas phase fit for the second period without filter. The fitted gas phase data is used to determine $C_{g,nopinone}$, and to subtract the gas phase from the whole aerosol phase measurements, which results in $C_{p,nopinone}$. As the fragmentation of nopinone in the drift tube of the PTR-ToF-MS is the same for $C_{g,nopinone}$ and $C_{g,nopinone}$, one can state that

$$\frac{C_{p,nopinone}}{C_{g,nopinone}} = \frac{C_{p,C_9H_{15}O^+}}{C_{g,C_9H_{15}O^+}}$$

Therefore, in this approach the $C_9H_{15}O^+$ signal in ppb (see section 4.1) is taken for the determination of the nopinone partitioning coefficient. For results from this approach see section 5.3.1.

4.5 Determination of the partitioning coefficient from a PTR-ToF-MS coupled with the ACM

The second experimental approach to determine the partitioning coefficient uses the coupling of PTR-ToF-MS and ACM. In this chapter, the details of this determination are explained.

Like the first approach, the determination of the nopinone partitioning coefficient is based on Equation 1.1. While the PTR-ToF-MS measurements provide on-line data, the ACM needs to sample aerosol particle phase in order to produce a desorption peak high enough for concurrent data analysis. Time equivalence can be achieved by using the average of total SOA mass concentration from the respective ACM sampling period for C_{TSP} from SMPS data and the average of the PTR-ToF-MS gas phase data for the same period for $C_{g,i}$. In the case that periods of PTR-ToF-MS measurements without filter are included in the ACM sampling times, the above described gas phase data fits are used (see section 4.4). Figure 4.5 shows the ACM desorption peak for nopinone on 2009/11/17 from the second ACM desorption of that experiment day. From the nopinone signal (shown in black) during the ACM measurement a baseline (shown in blue), which is fitted to the synthetic air signal from before and after the desorption peak, is subtracted. The baseline-subtracted signal is shown in violet. Between the vertical bars, the area of the desorption peak is defined in which the baseline corrected nopinone signal is integrated. The resulting area under the peak has to be devided by the PTR-ACM measurement time t_{PTR} in $[s]$ to derive the mixing ratio ζ_{PTR} in $[ppb]$ of the nopinone particulate phase in the volume that is sampled by the PTR-ToF-MS from the ACM (V_{PTR} in $[m^3]$).

$$\zeta_{PTR} = \frac{\int Peak}{t_{PTR}}$$

The collector mass loading M_{Coll} in $[\mu g]$ results from

$$M_{Coll} = \frac{p \cdot m \cdot \zeta_{PTR} \cdot 10^{-3}}{R \cdot T} \cdot V_{PTR}$$

where p is the pressure in AIDA in $[Pa]$, m the molecular mass in $\left[\frac{g}{mol}\right]$, R the ideal gas constant in $\left[\frac{J}{molK}\right]$, T the experiment temperature in $[K]$, and V_{PTR} the PTR-ACM measurement volume. The mass concentration of the investigated aerosol particle phase in the AIDA chamber $C_{p,i}$ in $\left[\frac{\mu g}{m^3}\right]$ equals the mass concentration in the ACM measurement volume V_{ACM}. Therefore,

it can be calculated as

$$C_{p,i} = \frac{M_{Coll}}{V_{ACM}}$$

Thus, the particulate mass concentration from the ACM, which is needed to determine the partitioning coefficient, can also be derived from:

$$C_{p,i} = \frac{V_{PTR}}{V_{ACM}} \cdot \frac{p \cdot m \cdot \zeta_{PTR} \cdot 10^{-3}}{R \cdot T} \tag{4.7}$$

The respective flow and time values of the PTR-ToF-MS and the ACM to derive the respective volumes can be found in Table 3.2 and 3.3. Results of the described method are presented and discussed in chapter 5.
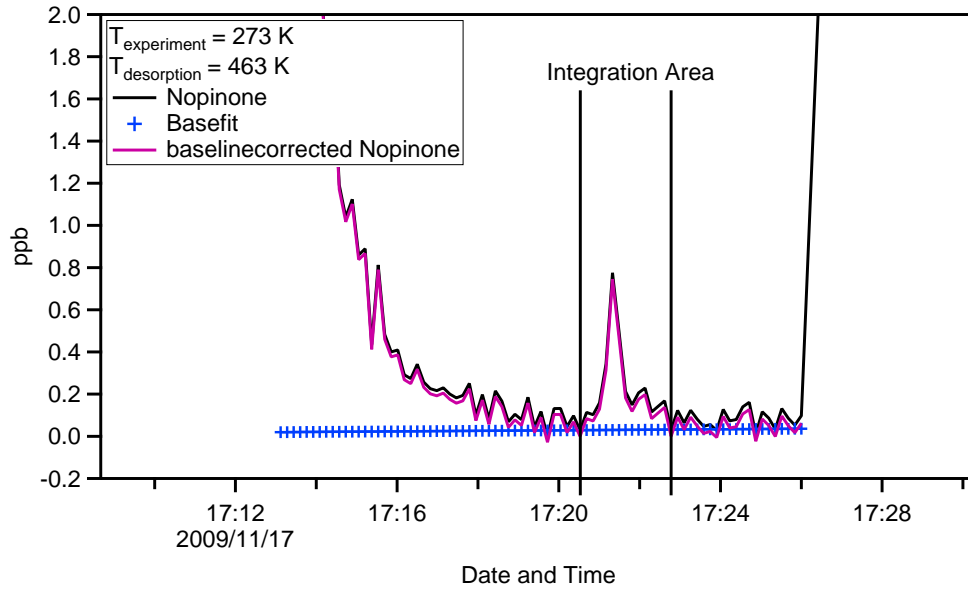

Figure 4.5: Determination of the particle phase mass concentration from the ACM desorption period. In black the nopinone signal in ppb is shown. A sharp desorption peak can be seen in the ACM measurement period. The blue crosses show the fitted baseline, which is subtracted in the black nopinone signal. The baseline-subtracted nopinone signal is shown in violet. Vertical bars indicate the area used for the integration of the baseline-corrected nopinone desorption peak.

Chapter 5

Results and discussion of β- and α-pinene ozonolysis experiments

In this chapter the results of the experiments on α- and β-pinene ozonolysis at the AIDA chamber of the Karlsruhe Institute of Technology (KIT) are presented and discussed. The partitioning coefficient of nopinone is determined at different temperatures from measurements of the PTR-ToF-MS in combination with a particle filter set-up and from the combination of PTR-ToF-MS and ACM. The results are compared to a partitioning coefficient experimentally determined at the Jülich Aerosol Chamber with a combination of ACM and a Gas Chromatography-Mass Spectrometer (GC-MS) and to theoretically determined partitioning coefficients. Additionally, the fraction of nopinone and total SOA from the combination of ACM and PTR-ToF-MS are compared to SOA measurements from a Scanning Mobility Particle Sizer (SMPS) and to literature.

5.1 α-Pinene Ozonolysis

Applying the data analysis procedures developed in this work and the fragmentation investigations, the α-pinene mixing ratios during the α-pinene ozonolysis experiments are shown in Figure 5.1 and 5.2. The upper panel of each graph shows the total SOA mass concentration from SMPS measurements and the ozone mixing ratio. A density of 1.25 $\frac{g}{cm^3}$ is assumed for the SOA mass (Saathoff et al., 2009). In the lower panel of the graphs the mixing ratios of α-pinene, respectively α-pinene and nopinone are shown. All Figures show a prompt SOA formation from the reaction of α-pinene with
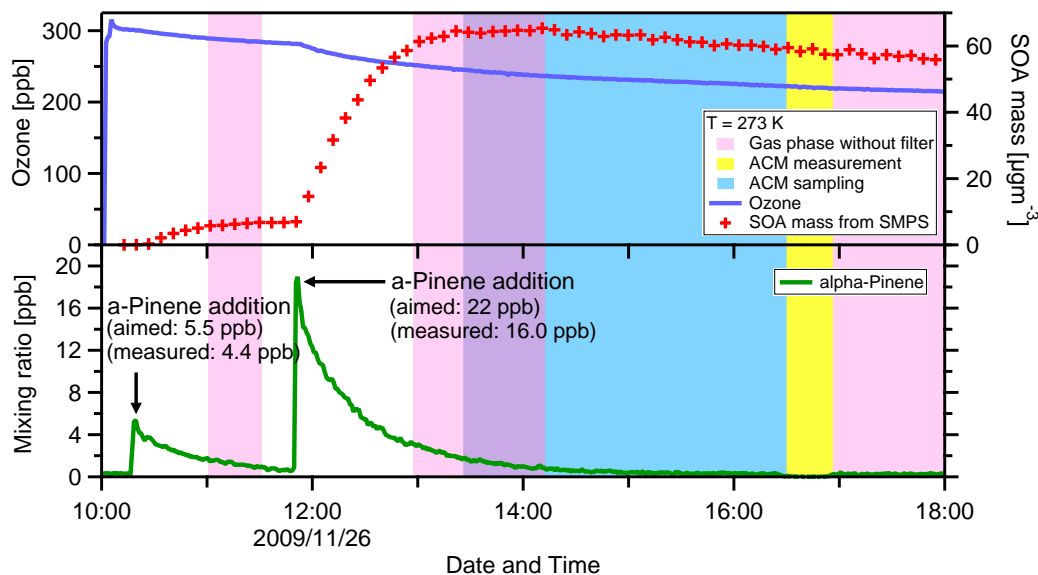
Figure 5.1: α-Pinene experiment from 2009/11/26. The upper panel shows the
ozone mixing ratio in ppb in the AIDA chamber and the total SOA mass in $\frac{\mu g}{m^3}$ from
SMPS-data. The lower panel shows the α-pinene mixing ratio from PTR-ToF-MS
measurements. The pink shaded areas mark measurement periods without particle
filter in the sample line. Blue areas mark periods, in which the ACM sampling took
place. Note that ACM-sampling and PTR-ToF-MS measurement were conducted
at the same time (see section 3.2). Periods with ACM-sampling and PTR-ToF-
MS measurement without particle filter are shaded in violet. ACM-measurement
periods are highlighted in yellow. For the determination of the α-pinene mixing
ratios after injection, a mixing time of 3 minutes after the injection process was
completed was considered.

ozone. Therefore α-pinene and ozone mixing ratios decrease with the start
of the α-pinene injection while the SOA mass concentration increases.
Figure 5.2 shows that nopinone addition to the chamber does not lead to an
increase in SOA mass concentration. With an injection of pinonaldehyde an
increasing SOA mass was detected. As pinonaldehyde is in the condensed
phase at the experiment temperature, it could not be detected in the PTR-
ToF-MS gas phase data (further investigations of pinonaldehyde can be found
in section 5.1.1). Unexpected is the increase of the nopinone signal at the in-
jection of pinonaldehyde. As a reason for that, one has to consider impurities
of the injected pinonaldehyde. It was generated in the Karlsruhe Institute
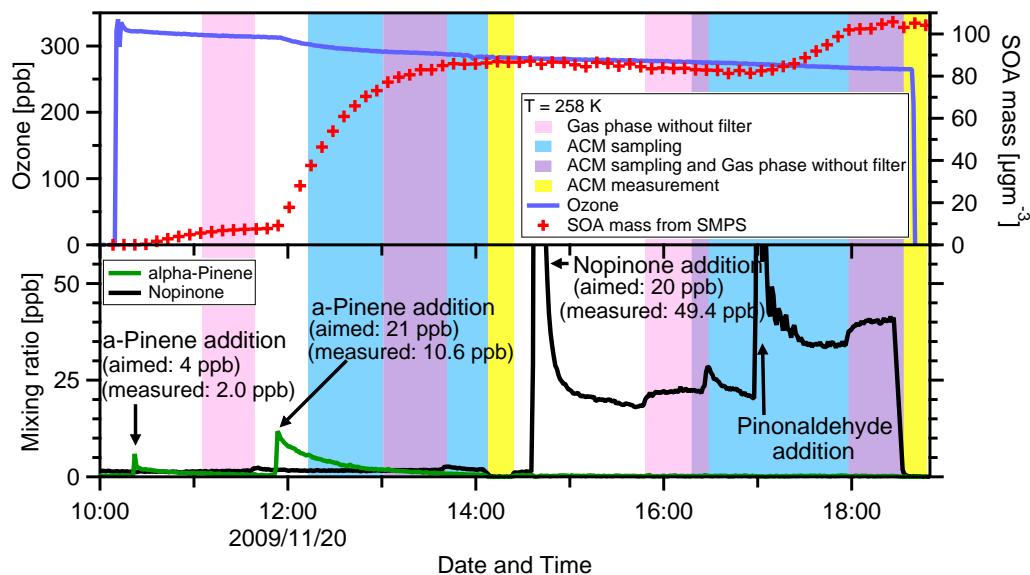of Technology (KIT) from the reaction of α-pinene and ozone. Hence, it had

Figure 5.2: α-Pinene experiment from 2009/11/20 (see Figure 5.1 for description).

no certified purity.

The errors of the mixing ratios were calculated based on gaussion error propagation for Equation 4.1 (for the error equation see appendix D). They are too small to show in the Figures. However, the systematic error discussed in chapter 4.2 leads to an uncertainty of 50 % of the respective mixing ratios. This leads to a possible offset of the mixing ratios, but leaves the relative course of the data undisturbed.

One of the aims of the PTR-ToF-MS was to give a measure on how precise the injection process at the AIDA chamber works. Therefore, the aimed mixing ratios have to compared with the ones measured by the PTR-ToF-MS. The measured value of each injected mixing ratio is determined after the injection time span plus additional 3 minutes to ensure homogeneous mixing in the chamber (see 3.1). The respective mixing ratio before the injection started was subtracted as background. Additionally, for α-pinene the amount that has reacted with ozone in the time span between the start of injection and the measurement time has to be considered. For that, the decrease in the ozone mixing ratio for that time is taken. It can be considered that one ozone molecule reacts with one α-pinene molecule. Therefore, the corresponding amount of α-pinene is added to the measured α-pinene mixing ratio. This corrects for the reactions between injection and measurement time. The aimed, measured, and reaction-corrected mixing ratios after

injection are compared in Table 5.1. For the experiment on 2009/11/26 the
measured and the aimed injected mixing ratios are within the uncertainty
range of the reaction-corrected values. In the experiment on the 2009/11/20
the reaction-corrected α-pinene mixing ratios are below the aimed values for
both injections. The measured nopinone mixing ratio on that day is higher
than the aimed value. Concluding from that, the aimed values were reached
within a factor of up to ≈ 2 for α-pinene and a factor of up to ≈ 0.4 for
nopinone. Reasons for differences between measured and aimed mixing ra-
tios lie e.g. in wall effects.

Table 5.1: Comparison of aimed, measured and ozone-reaction corrected mixing
ratios in the AIDA chamber after injection.

Experiment day	T [K]	Injection	Aimed mixing ratio [ppb]	Measured mixing ratio [ppb]	Reaction-corrected mixing ratio [ppb]
2009/11/20	258	α-pinene 1	4.0	2.0 ± 1.0	2.3 ± 1.15
		α-pinene 2	21.0	10.6 ± 5.3	10.8 ± 5.4
		Nopinone	20.0	49.4 ± 24.7	
2009/11/26	273	α-pinene 1	5.5	4.4 ± 2.2	5.0 ± 2.5
		α-pinene 2	22.0	16.0 ± 8.0	16.3 ± 8.15

5.1.1 α-Pinene Ozonolysis Products

One of the major α-pinene ozonolysis products is pinonaldehyde ($C_{10}H_{16}O_2$)
e.g. (Yu et al., 1999), (Tillmann, 2007). At temperatures of $T \leq 273K$
pinonaldehyde is in the condensed phase (Tillmann et al., 2010). The α-
pinene experiments were conducted at 258 K and 273 K. In accordance to
that, both α-pinene experiments show no gas phase signal in the PTR-ToF-
MS measurements for $C_{10}H_{17}O_2^+$ at m/z 169.1229. Therefore, the correlation
matrix, determining the Pearson correlation coefficient, to determine pinon-
aldehyde fragments could not be applied here. Tillmann (2007) found a
pinonaldehyde fragment on mass 151 amu in PTR-MS measurements. He
concluded that $C_{10}H_{15}O^+$ was generated by the abstraction of H_2O from
pinonaldehyde during ionization with H_3O^+.
As the gas phase data does not provide information on pinonaldehyde frag-
ments, the particle phase data from the ACM was investigated for pinonalde-
hyde and fragments. The second ACM-sampling on 2009/11/20 included the

pinonaldehyde injection (see Fig. 5.2). Therefore, the ACM-data should show either pinonaldehyde or pinonaldehyde fragments. Figure 5.3 shows the signals of $C_{10}H_{17}O_2^+$ for the protonated pinonaldehyde, $C_{10}H_{15}O^+$, and $C_9H_{11}O_2^+$ for possible pinonaldehyde fragments on m/z 151.
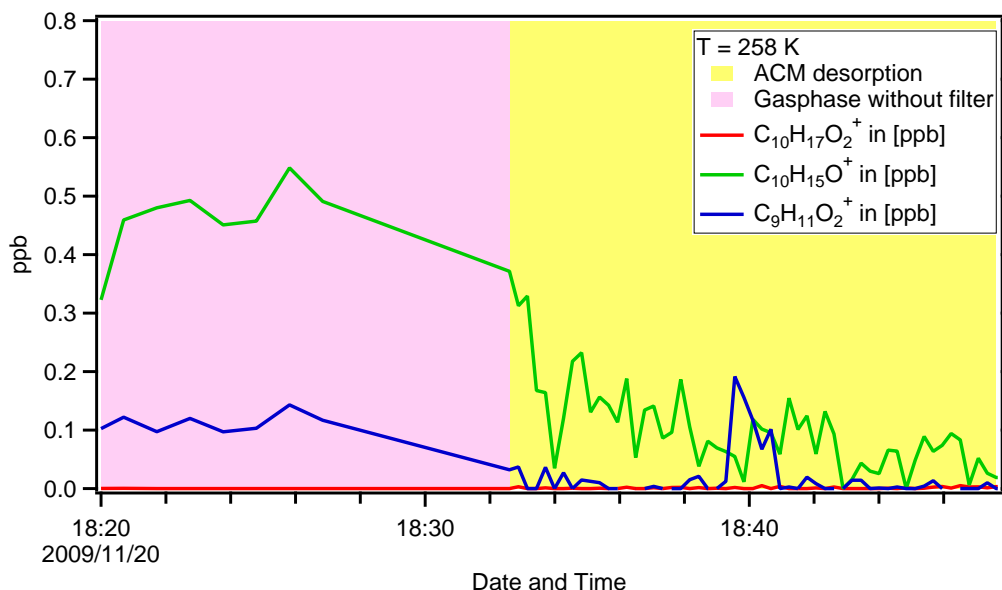

Figure 5.3: Second ACM-phase of the experiment on 2009/11/20. The pink shaded area shows gas phase measurements without filter. The yellow area shows the ACM desorption period. Pinonaldehyde is in the particulate phase at the experiment temperature of 258 K. Thus, no gas phase signal is expected. Nevertheless, the particulate phase is expected to result in a desorption peak of either the pinonaldehyde parent ion $C_{10}H_{17}O_2^+$ and/or signal from pinonaldehyde fragments. The pinonaldehyde parent ion $C_{10}H_{17}O_2^+$ (red line) and the fragment $C_{10}H_{15}O^+$ (green line) found in (Tillmann, 2007) show no desorption peak signal during the ACM desorption period. However, a small desorption peak can be seen for $C_9H_{11}O_2^+$ (blue line).

The pink area of the graph shows PTR-ToF-MS data without particle filter in the measurement line. The yellow area shows ACM measurement data. As mentioned before, the pinonaldehyde signal and the signal of the potential pinonaldehyde fragments on m/z 151 is zero, respectively close to zero in the gas phase data. The particulate phase from the ACM desorption shows no desorption peak for pinonaldehyde and for $C_{10}H_{15}O^+$, whereas, $C_9H_{11}O_2^+$ shows a small ACM desorption peak. This suggests that $C_9H_{11}O_2^+$ might be the pinonaldehyde fragment on m/z 151 which has previously been

interpreted as $C_{10}H_{15}O^+$ from unit mass resolution data. Nevertheless, abstraction of a water molecule from pinonaldehyde in the PTR-ToF-MS drift tube is far more likely than an ionizing reaction leading to $C_9H_{11}O_2^+$ which would require the abstraction of CH_6. To prove that the pinonaldehyde fragment on m/z 151 is $C_9H_{11}O_2^+$ further experiments at temperatures above 273 K have to be conducted. A matrix correlation of these experiments would result in a fragmentation pattern of pinonaldehyde.

5.2 β-Pinene Ozonolysis

The β-pinene and nopinone mixing ratios which result from the data analysis procedure and fragmentation investigation developed and conducted in this work can be seen in Figures 5.4 - 5.8.
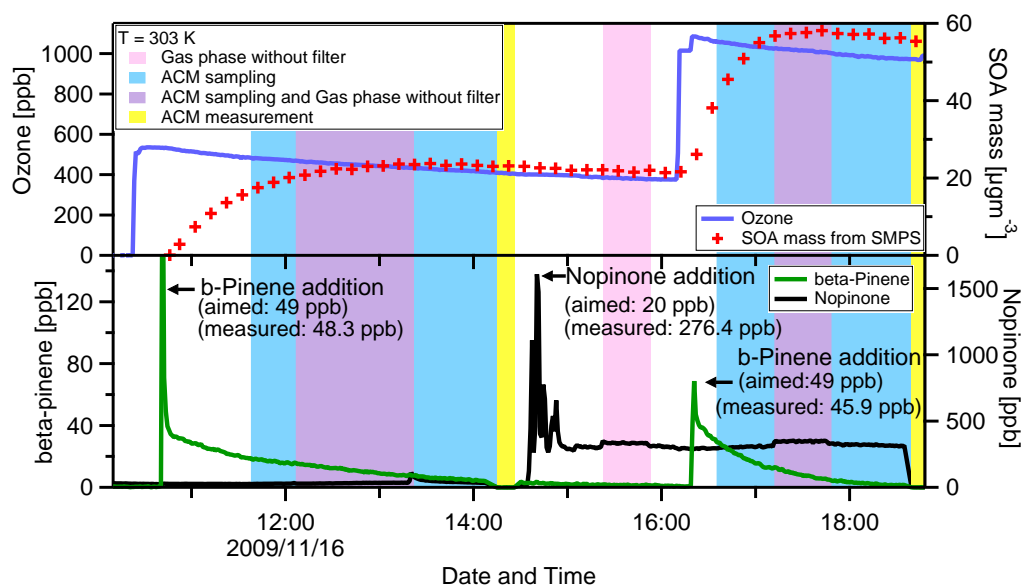

Figure 5.4: Experiment from 2009/11/16. The colored areas show gas phase without filter (pink), ACM sampling periods (blue), gas phase without filter and concurrent ACM sampling (violet), and ACM measurement periods (yellow). The upper panel shows SOA mass from SMPS measurements and ozone mixing ratios. The lower panel shows β-pinene and nopinone mixing ratios. This experiment shows a high difference between the aimed nopinone injection and the measured nopinone mixing ratio (right axis).

β-pinene was injected into the AIDA chamber after ozone. All Figures show a decreasing β-pinene mixing ratio due to the oxidation processes with ozone. This leads to a significant increase of the SOA mass concentration in all experiments after each β-pinene injection. The generation of nopinone from β-pinene ozonolysis was detected for all experiments as an increasing nopinone mixing ratio. It can be seen clearly in Figure 5.8. As in the α-pinene ozonolysis experiment on 2009/11/20 (Figure 5.2), it can be seen in all β-pinene ozonolysis experiment that nopinone injections did not lead to an increase in SOA mass concentration.
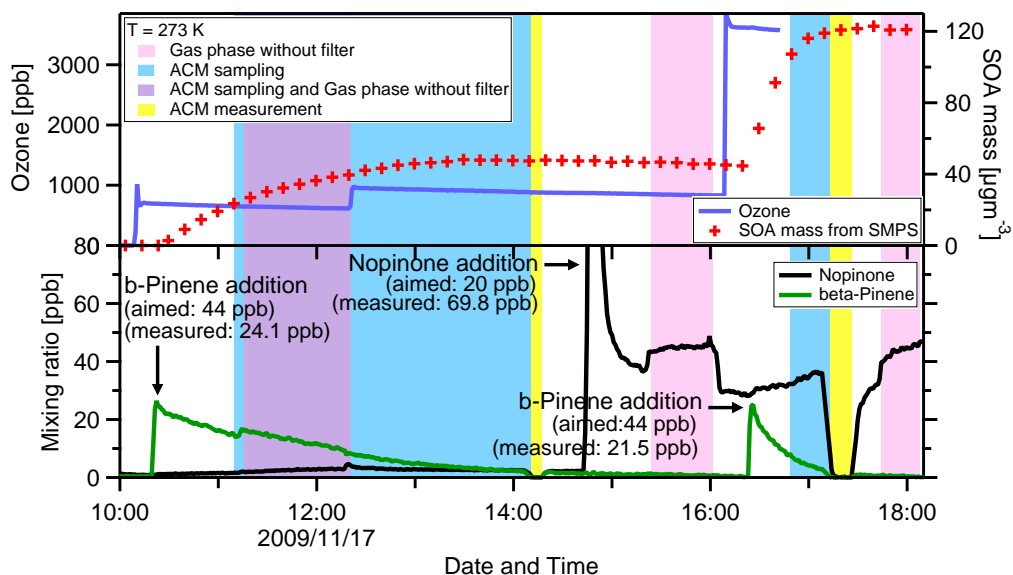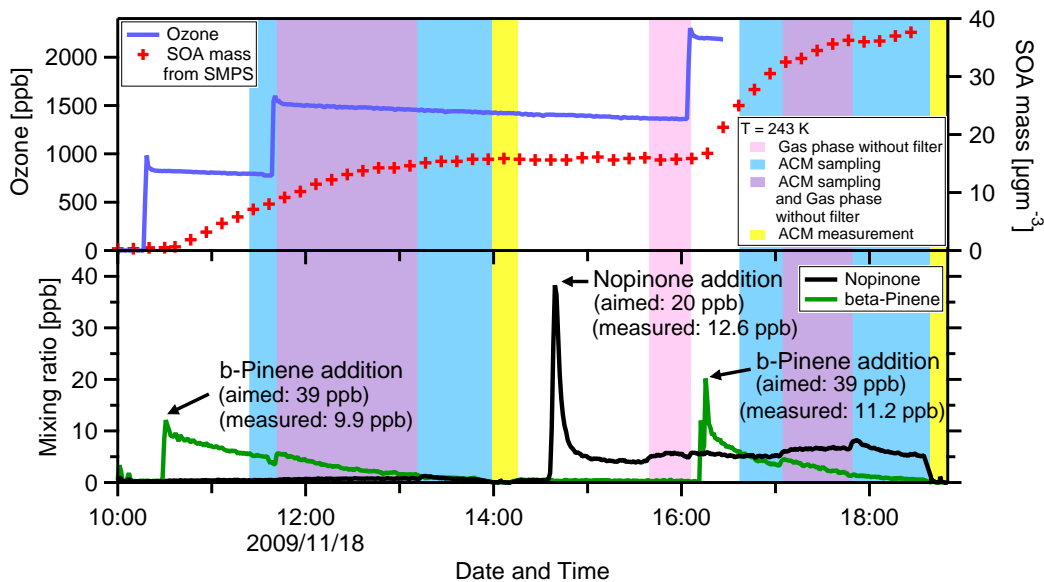
Figure 5.5: Experiment from 2009/11/17 (see Figure 5.4 for description).

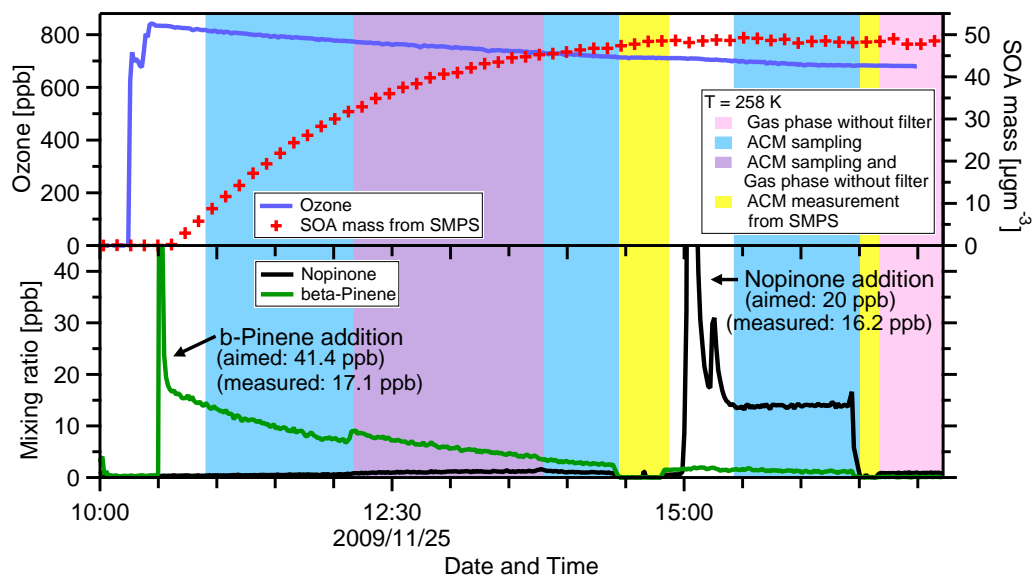Figure 5.6: Experiment from 2009/11/18 (see Figure 5.4 for description).

74

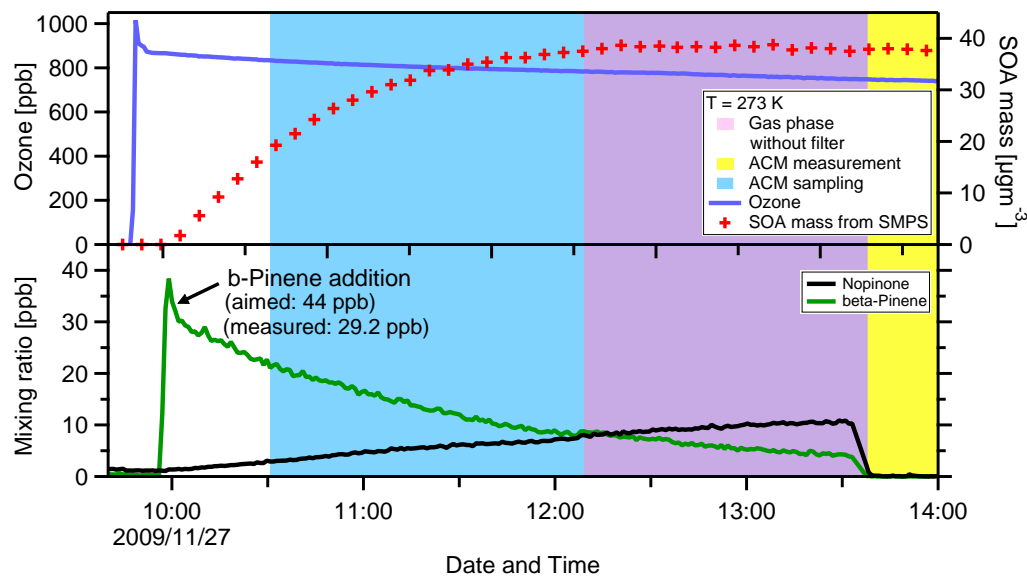Figure 5.7: Experiment from 2009/11/25 (see Figure 5.4 for description).

Figure 5.8: Experiment from 2009/11/27 (see Figure 5.4 for description).

In analogy to the α-pinene ozonolysis experiments, the errors calculated
from gaussian error propagation of Equation 4.1 are too small to show in the
Figures (for error equation see appendix D). Nevertheless, the systematic
error discussed in chapter 4.2 has to be taken into account. It leads to an
uncertainty of up to 50% of the respective mixing ratio. This results in a
possible offset of the mixing ratios, but leaves the relative course of the data
undisturbed. Thus, only an approximate measure of how precise the injection
process in the AIDA chamber is can be concluded. For this, the aimed mixing
ratios are compared with the measured mixing ratios for nopinone and with
the reaction-corrected mixing ratios for β-pinene . As described before, the
measured injection values are determined after the injection time span plus
3 additional minutes to ensure homogeneous mixing in the chamber. As a
background, the respective mixing ratio before the injection was subtracted.
For β-pinene the measured mixing ratio is corrected for the amount fraction
that already reacted with ozone within the time span from the start of the
injection until the measured value. Aimed and measured mixing ratios are
shown in each experiment Figure at the injection peak. An overview of
aimed, measured, and reaction-corrected mixing ratios is given in Table 5.2.

Table 5.2: Comparison of aimed and measured mixing ratios in the AIDA chamber
after injection.

Experiment day	T [K]	Injection	Aimed mixing ratio [ppb]	Measured mixing ratio [ppb]	Reaction-corrected mixing ratio [ppb]
2009/11/16	303	β-pinene 1	49.0	48.3 ± 24.15	49.3 ± 24.65
		Nopinone	20.0	276.4 ± 138.2	
		β-pinene 2	49.0	45.9 ± 22.95	46.4 ± 23.2
2009/11/17	273	β-pinene 1	44.0	24.1 ± 12.05	25.4 ± 12.7
		Nopinone	20.0	69.8 ± 34.9	
		β-pinene 2	44.0	21.5 ± 10.75	25.0 ± 12.5
2009/11/18	243	β-pinene 1	39.0	9.9 ± 4.95	11.2 ± 5.6
		Nopinone	20.0	12.6 ± 6.3	
		β-pinene 2	39.0	11.2 ± 5.6	12.2 ± 6.1
2009/11/25	258	β-pinene	41.4	17.1 ± 8.55	18.3 ± 9.15
		Nopinone	20.0	16.2 ± 8.1	
2009/11/27	273	β-pinene	44.0	29.2 ± 14.6	33.5 ± 16.75

The aimed and reaction-corrected values for the β-pinene injections on 2009/11/16 and on 2009/11/27 are in agreement within the uncertainty ranges. For nopinone, only the aimed and measured values for the injection on 2009/11/25 are in agreement within the uncertainty ranges. Regarding β-pinene, the aimed values are underestimated in comparison to the measured data by a factor of up to ≈ 3.5. For nopinone the factor between the aimed and the measured values ranges between ≈ 0.07 and ≈ 1.6. Therefore, no general factor can be concluded from the nopinone measurements. As mentioned before, differences between measured and aimed mixing ratios can result e.g. from wall effects. Figure 5.9 shows the detected fractions of reaction-corrected to aimed mixing ratios for β-pinene and measured to aimed mixing ratios for nopinone depending on the experiment temperature.
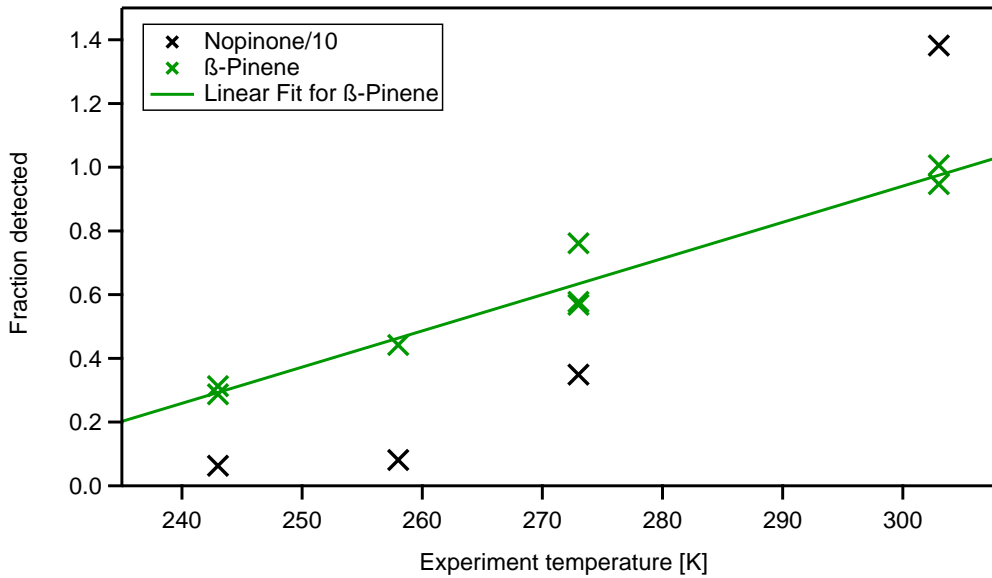

Figure 5.9: Detected fractions of the reaction-corrected mixing ratios for β-pinene (green) and of the measured to aimed mixing ratios for nopinone in dependence of the experiment temperature. The detected fraction shows a linear increase for β-pinene .

For clarity errors are not shown in this Figure. They follow the errors given in Table 5.2. For β-pinene the detected fractions show a linear increase with increasing experiment temperature (slope: 0.011 ± 0.001, y-intercept: -2.469 ± 0.293). Concluding from that, losses at the AIDA chamber walls show a linear decreasing behavior with increasing temperature for β-pinene.

The temperature behavior for the detected fraction of nopinone could not be
fitted sufficiently well due to the scarcity of data points. Nevertheless, Figure 5.9 clearly shows a non-linear temperature dependence for the detected
nopinone fraction. Thus, more complex wall effects can be considered in
the case of nopinone than for β-pinene. Therefore, further investigations for
nopinone remain to be implemented, considering the wall effects, but also a
higher than expected nopinone sensitivity of the PTR-ToF-MS.

5.3 β-Pinene Ozonolysis Products

5.3.1 Nopinone Partitioning

The partitioning coefficient of nopinone was determined using two different
experimental approaches described earlier, in combination with Equation
1.1. The two approaches result in the gas and particulate concentration of
nopinone. The total aerosol mass concentration was derived from SMPS measurements, assuming a density of 1.25 $\frac{g}{cm^3}$. An overview of the partitioning
coefficients derived from the different methods is shown in Table 5.3. The
errors of the experimentally determined partitioning coefficients result from
the Gaussian error propagation of Equation 1.1. For further comparison,
an experimentally derived value from Hohaus (2009), a theoretically derived
partitioning coefficient from Chen and Griffin (2005), and values calculated
following Jenkin (2004) are added.

Table 5.3: Partitioning coefficients in $\left[\frac{m^3}{\mu g}\right]$ from experimental data of this work, a β-pinene ozonolysis experiment at the Jülich Aerosol Chamber and two different model approaches. [1] Hohaus (2009); [2] Chen and Griffin (2005); [3] calculated following Jenkin (2004)

T [K]	PTR-ToF-MS with/without filter, this work	ACM-PTR-ToF-MS, this work	Jülich Aerosol chamber [1]	Chen 2005 [2]	Jenkin 2004 [3]
243	$2.34 \cdot 10^{-2} \pm 4.67 \cdot 10^{-3}$	$1.32 \cdot 10^{-3} \pm 4.24 \cdot 10^{-4}$			$3.81 \cdot 10^{-5} \pm 2.65 \cdot 10^{-6}$
243	$7.97 \cdot 10^{-3} \pm 9.15 \cdot 10^{-4}$	$2.77 \cdot 10^{-4} \pm 3.12 \cdot 10^{-5}$			
258	$1.13 \cdot 10^{-2} \pm 3.55 \cdot 10^{-3}$	$1.33 \cdot 10^{-3} \pm 2.36 \cdot 10^{-4}$			$7.33 \cdot 10^{-6} \pm 5.09 \cdot 10^{-7}$
258		$6.19 \cdot 10^{-5} \pm 1.42 \cdot 10^{-6}$			
273	$5.52 \cdot 10^{-3} \pm 1.31 \cdot 10^{-3}$	$2.20 \cdot 10^{-5} \pm 1.56 \cdot 10^{-6}$			$1.74 \cdot 10^{-6} \pm 1.21 \cdot 10^{-7}$
273	$1.03 \cdot 10^{-2} \pm 4.15 \cdot 10^{-4}$	$7.94 \cdot 10^{-5} \pm 2.37 \cdot 10^{-5}$			
294			$2.32 \cdot 10^{-5}$		$3.12 \cdot 10^{-7} \pm 2.17 \cdot 10^{-8}$
298					$2.32 \cdot 10^{-7} \pm 1.62 \cdot 10^{-8}$
303	$6.43 \cdot 10^{-3} \pm 5.62 \cdot 10^{-4}$				$1.63 \cdot 10^{-7} \pm 1.13 \cdot 10^{-8}$
303	$1.84 \cdot 10^{-3} \pm 2.11 \cdot 10^{-4}$	$1.40 \cdot 10^{-6} \pm 1.37 \cdot 10^{-7}$			
308				$7.60 \cdot 10^{-4}$	$1.16 \cdot 10^{-7} \pm 8.06 \cdot 10^{-9}$

Approach 1: With and without filter The nopinone partitioning coefficient from PTR-ToF-MS measurements with and without filter is shown in Figure 5.10.
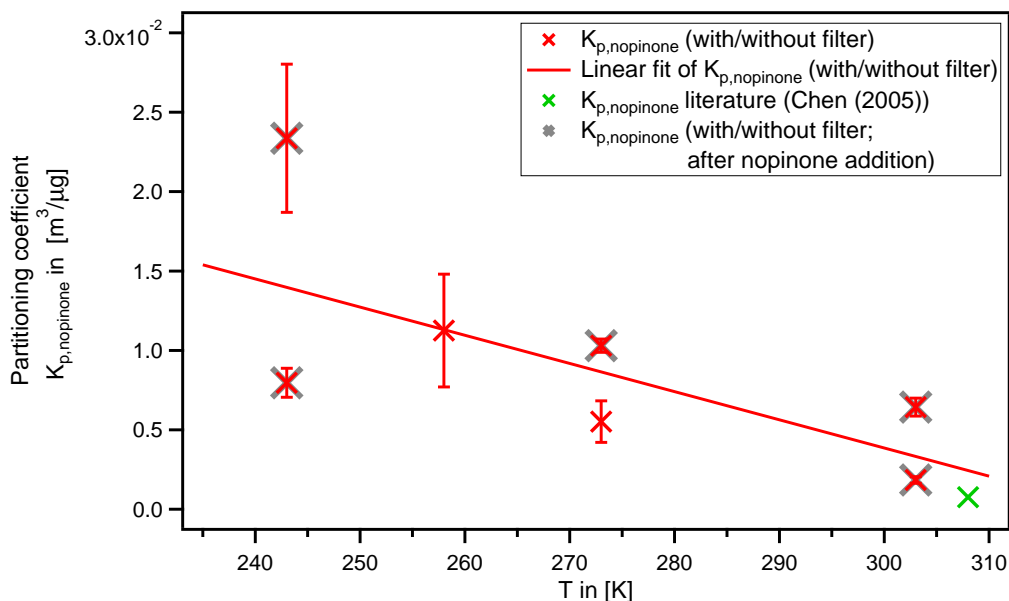

Figure 5.10: Nopinone partitioning coefficients from PTR-ToF-MS measurements with and without filter (red crosses). The red line shows a linear fit to the decreasing coefficients with increasing temperature. Gray crosses mark the partitioning coefficients determined after nopinone injection into the AIDA chamber. The green cross shows a partitioning coefficient from Chen and Griffin (2005).

It shows a linear decrease. A linear fit to the partitioning coefficients follows

$$K_{p,nopinone}(T) = -1.77 \cdot 10^{-4} \left(\pm 8.52 \cdot 10^{-5} \right) \cdot T + 5.71 \cdot 10^{-2} \left(\pm 2.23 \cdot 10^{-2} \right)$$

No trend for higher or lower partitioning coefficients can be observed when comparing coefficients determined from periods before and after nopinone injection into the AIDA chamber.

Discussion of the experimental partitioning coefficients from this work: The partitioning coefficients of approach 1 are several orders of magnitude higher than the partitioning coefficients from ACM measurements. At a temperature of 243 K, the difference is one order of magnitude to ACM measurements (see Table 5.3). With increasing temperature the difference

increases. At 303 K, the partitioning coefficients from approach 1 are 3 orders of magnitude higher than the one derived from the ACM measurement. The basic difference between the two approaches is the experimental determination of the nopinone particle phase information. For approach 1, the difference from measurements with and without filter results in the particle phase concentration. For approach 2, the integrated ACM desorption signal delivers $C_{p,nopinone}$. Therefore, the development of the mixing ratios of β-pinene and nopinone when switching to measurements without filter has to be further examined. Comparison of the periods without filter in Figures 5.4 to 5.8 show an increase of the nopinone signal, as expected. A short increase of the nopinone signal after switching back to filter measurement appears when the filter has to reach equilibrium with the restarted gas flow through the filter. Thus, only periods with equilibrium filter conditions were used for the determination of the partitioning coefficients. When considering the β-pinene signal at filter switching times, an unexpected increase of the β-pinene in periods without filter at lower experiment temperatures can be seen. β-Pinene is in the gas phase at all experiment temperatures (β-pinene vapor pressure $p_0 = 2.61 \; mbar$ at T=292 K, calculated from National Institute of Standards and Technology (NIST) based on (Hawkins and Armstrong, 1954)). Hence, a temperature-dependent filter sampling of the gas phase must be concluded. Considering the lower vapor pressure of nopinone in comparison to that of β-pinene, it is expected that this effect occurs for nopinone as well, but that it is concealed by the expected behavior for nopinone. In conclusion, the measured nopinone concentration in the gas phase is possibly lower than the real concentration. This leads to higher nopinone partitioning coefficients for both approaches. For approach 1, the particle phase concentration is derived by subtracting the gas phase concentration from the concentration derived at periods without filter. Therefore, a low gas phase concentration also leads to a higher particle phase concentration for this approach. This leads to an even higher partitioning coefficient for approach 1.

Discussion of the temperature dependence of partitioning coefficients from approach 1: The detected nopinone fraction in Figure 5.9 indicates non-linear wall effects for different temperatures. This would also lead to a non-linear filter sampling behavior, as the filter was kept at the experiment temperature. Concluding from this and from the filter behavior for β-pinene, the above described effect leading to high partitioning coefficients should be smaller with increasing temperature. Nevertheless, the differences in the partitioning coefficients between the two approaches increase with higher temperatures. While a decrease of the partitioning coefficient with

increasing temperature is expected, the temperature dependence from approach 1 is not comparable to that found in approach 2 and in the literature (see below).

Approaches 1 and 2 differ in one other aspect of the measurement, which should be discussed concerning the unexpected values and temperature behavior for approach 1. The filter set-up following Tillmann et al. (2010) is based on the assumption that all nopinone in the aerosol particle phase is converted to the gas phase while passing through the heated PTR-ToF-MS inlet line. Tillmann et al. (2010) showed that this worked well for pinonaldehyde. Considering that pinonaldehyde is less volatile than nopinone, the set-up should work for nopinone, as well. However, incomplete evaporation of nopinone to the gas phase would lead to lower measured particulate concentrations of nopinone and therefore to lower partitioning coefficients. The effect would be stronger for lower experiment temperatures. This could partly explain the only linear decrease of the partitioning coefficient with increasing temperature. However, the partitioning coefficients from approach 1 are generally higher than the calculated partitioning coefficients and those resulting from approach 2 (see below). Therefore, even if nopinone is only partly evaporated to the gas phase in the heated inlet line, this cannot fully explain the differences found.

Comparison of the partitioning coefficients of approach 1 with other experimental data: The partitioning coefficient from Hohaus (2009) originates from a β-pinene ozonolysis experiment, using PTR-ToF-MS, SMPS and ACM-GC-MS data in combination with Equation 1.1. There, ≈ 600 ppb β-pinene were added to the Jülich Aerosol Chamber in the presence of ozone. The experiment was conducted at 294 K. Detailed descriptions can be found in Hohaus (2009). However, the partitioning coefficient shown in Table 5.3 differs from that presented in Hohaus (2009). This is due to the fact that the PTR-ToF-MS gas phase data for nopinone has been recalculated. For this purpose, the nopinone fragmentation has been determined for that experiment using the correlation matrix method described in this work. This results in a partitioning coefficient slightly different from that presented in (Hohaus, 2009). The present work does not include experiments at temperatures of 294 K. Taking the linear fit of the partitioning coefficients from approach 1 into account (see Figure 5.10) the partitioning coefficient from approach 1 is two orders of magnitude higher than the result of Hohaus (2009).

Comparison of the partitioning coefficient from approach 1 with theoretically derived values: Shown in green in Figure 5.10 is the nopi-

none partitioning coefficient at 308 K from Chen and Griffin (2005). There, the partitioning coefficient was calculated with the Caltech Atmospheric Chemistry Mechanism (CACM) coupled to an aerosol module (Model to Predict Multi-phase Partitioning of Organics (MPMPO)). The gas-to-particle partitioning of semivolatile organic compounds is modeled and compared to data sets of β-pinene experiments on ozonolysis, photo-oxidation, and reactions with NO_3. The model simulations were based on Pankow (1994). The nopinone partitioning coefficient of $7.60 \cdot 10^{-4}$ $\left[\frac{m^3}{\mu g} \right]$ is well comparable to the coefficients derived from approach 1.

It has to be noted that the difference in nopinone partitioning coefficients from literature is three orders of magnitude, comparing the values of Chen and Griffin (2005) and the calculated partitioning coefficient according to (Jenkin, 2004). Following Jenkin (2004), the partitioning coefficient can be derived from Equation 5.1

$$K_p = \frac{7.501 \cdot 10^{-9} RT}{MW_{om} \zeta p_L^0} \tag{5.1}$$

$\quad K_p \qquad$ Equilibrium partitioning coefficient $\quad \left[\frac{m^3}{\mu g} \right]$

$\quad R \qquad$ Ideal gas constant $\quad \left[\frac{J}{mol K} \right]$

$\quad T \qquad$ Temperature $\quad [K]$

$\quad MW_{om} \qquad$ Mean molecular weight of the condensed organic phase $\quad \left[\frac{g}{mol} \right]$

$\quad \zeta \qquad$ Activity coefficient for the given species in the condensed organic phase $\quad [1]$

$\quad p_L^0 \qquad$ Sub-cooled liquid vapor pressure $\quad [Torr]$

In this approach, it is assumed that the aerosol has an amorphous, liquid-like character (Pankow, 1994). Thus, p_L^0 is one of the key parameters in determining the partitioning coefficient from Equation 5.1. Jenkin (2004) used an expanded, semi-empirical form of the Clausius-Clapeyron equation, as seen in Equation 5.2.

$$ln \frac{p_L^0}{760} = \frac{-\Delta S_{vap}(T_b)}{R} \left[1.8 \left(\frac{T_b}{T} - 1 \right) - 0.8 \left(ln \frac{T_b}{T} \right) \right] \tag{5.2}$$

$$p_L^0 \qquad \text{Sub-cooled liquid vapor pressure} \quad [Torr]$$

$$\Delta S_{vap}(T_b) \qquad \text{Vaporization entropy change at } T_b \quad \left[\frac{J}{molK}\right]$$

$$T_b \qquad \text{Boiling point temperature} \quad [K]$$

$$T \qquad \text{Temperature} \quad [K]$$

$$R \qquad \text{Ideal gas constant} \quad \left[\frac{J}{molK}\right]$$

The sub-cooled liquid vapor pressures are determined here from the boiling
points T_b and the vaporization entropy changes at T_b. The results in Table
5.3 are calculated using Equations 5.1 and 5.2 with a mean molecular weight
(MW_{om}) of 180 $\frac{g}{mol}$. The activity coefficient was set to one (Jenkin, 2004).
For the nopinone boiling point T_b a value of 469.45 $\pm$ 8.0 K [1] was used. To
determine the vaporization entropy change at T_b an enthalpy $\Delta H_{vap}(T_b)$ of
43.25 $\pm$ 3.0 $\frac{kJ}{mol}$ was used[2], leading to $\Delta S_{vap} = 92.13 \pm 6.58 \left[\frac{J}{molK}\right]$.
While the nopinone partitioning coefficients from approach 1 agree well with
the value of Chen and Griffin (2005), they are up to four orders of magnitude
higher than the values derived for the experiment temperatures following
Jenkin (2004). Additionally, the decrease in the partitioning coefficient with
increasing temperature does not follow the behavior described by Equations
5.1 and 5.2.

Approach 2: ACM Figure 5.11 shows the nopinone partitioning coeffi-
cient determined from ACM measurements (black crosses). The exact values
are given in Table 5.3. As discussed above, the nopinone partitioning coef-
ficients derived from approach 2 are several orders of magnitude lower than
those determined with approach 1 and the partitioning coefficient from Chen
and Griffin (2005). They compare well to the partitioning coefficient from
Hohaus (2009). Compared to values derived following Jenkin (2004), the
partitioning coefficients of ACM measurements are one order of magnitude
higher.

**Discussion of the temperature dependence of partitioning coeffi-
cients from approach 2:** The black line in Figure 5.11 shows the fitted
temperature behavior of the partitioning coefficients from approach 2. It fol-
lows Equation 5.1. The vapor pressures used here are equal to those used for

---

[1]Calculated using Advanced Chemistry Development (ACD/Labs) Software V11.2
(©1994-2012 ACD/Labs)

[2]Calculated using Advanced Chemistry Development (ACD/Labs) Software V11.2
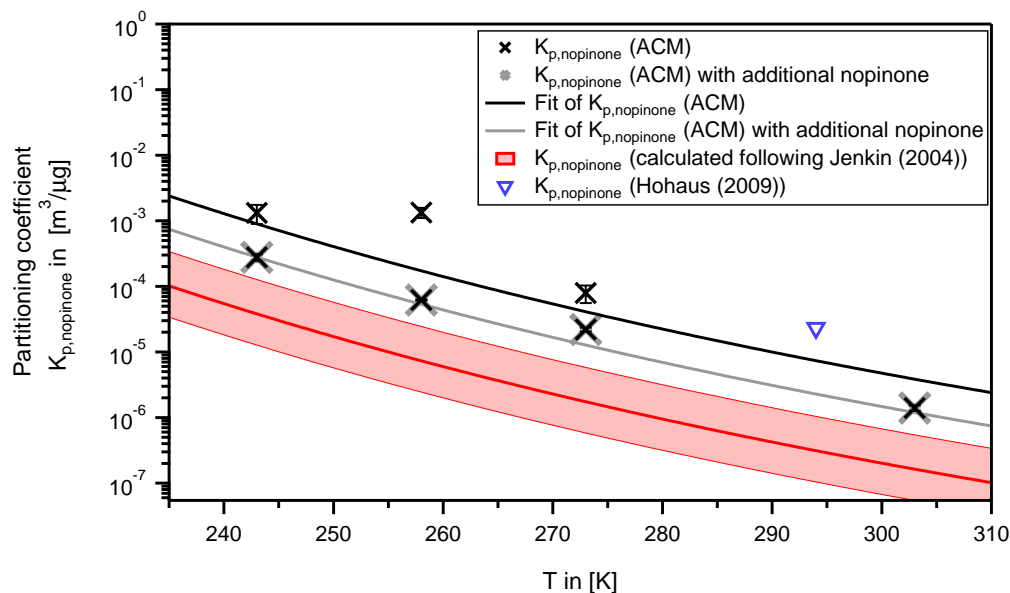(©1994-2012 ACD/Labs)

Figure 5.11: Nopinone partitioning coefficients at different temperatures from measurements with PTR-ToF-MS and ACM (black crosses) with a fit for the temperature dependence (black line). Gray crosses mark the partitioning coefficients from measurements with nopinone addition before the ACM sampling time started. The gray line shows the fit of these partitioning coefficients. The pink-shaded area marks the range of partitioning coefficients derived from Equations 5.1 and 5.2 with an activity coefficient between 3 (lower limit of the pink area) and 0.3 (upper limit of the pink area). The red line in the middle of the pink area shows the partitioning coefficients for an activity coefficient of 1. The blue triangle shows the experimentally derived partitioning coefficient from Hohaus (2009).

the calculations following Jenkin (2004). The activity coefficient was used as a free fitting parameter. This results in an activity coefficient of 0.042 ± 0.019. This is below the range of 0.3 - 3 that is typically assumed for activity coefficients in SOA formation (Seinfeld and Pankow, 2003). In Figure 5.11, the pink-shaded area shows the ranges of the partitioning coefficient derived following Jenkin (2004) with the activity coefficient between 0.3 and 3. The red line in the middle shows partitioning coefficients when the activity coefficient is set to one. For the lower limit the activity coefficient equals 3. In the upper limit the activity coefficient is 0.3.

There are three possible reasons for higher partitioning coefficients from approach 2 than found following Jenkin (2004):

1.) The filter behavior described above certainly leads to higher partition-

ing coefficients. However, the filter behavior is seen to be temperature-
dependent. Thus, the effect on the partitioning coefficient would be higher
for lower temperatures. As the temperature dependence found in approach
2 fits very well to that described by Equations 5.1 and 5.2 the filter behav-
ior can be ruled out as a reason for the difference between the partitioning
coefficients from ACM measurements and those calculated following Jenkin
(2004).
2.) The lower limit of the typically assumed range of 0.3 - 3 for the activity
coefficient is set too high.
3.) Several model studies (e.g. (McFiggans et al., 2010), (Chen and Griffin,
2005)) leave the activity coefficient, as well as the sub-cooled liquid vapor
pressure, as a free parameter to converge to one value during the simulation
steps. Therefore, the difference my also be due to lower vapor pressures re-
sulting from the experimental data.
It has to be noted that the experimental partitioning coefficients from ap-
proach 2 are generally lower for ACM sampling periods which were conducted
after nopinone injection into the AIDA chamber. These values are marked
with gray crosses in Figure 5.11. They are closer to the calculated partition-
ing coefficients following Jenkin (2004). Their temperature behavior is closer
to that described by Equations 5.1 and 5.2 than the temperature behavior
considering the whole experimental data set from approach 2. The fit of
the temperature behavior results in an activity coefficient of 0.137 ± 0.004,
which is again closer to the typically assumed range of 0.3 - 3.
In addition to the higher partitioning coefficient derived from periods before
nopinone addition, the first ACM periods from 2009/11/16 (T = 303 K) and
2009/11/17 (T = 273 K) do not show a desorption peak for nopinone. In the
early experiment periods, the SOA mass is comparatively low. Thus, also the
particulate nopinone concentration is lower than later throughout the exper-
iment day. It has to be verified, whether the nopinone collector mass loading
reached a lower limit for the early ACM periods. The nopinone collector mass
loadings for the different ACM measurements are shown in Table 5.4. They
are calculated from the particulate nopinone concentrations which result from
the ACM desorption peaks. These values are then multiplied by the total
sample volume of the respective ACM sampling period. Hence, the nopinone
collector mass loadings depend on the ACM sampling time spans. Thus,
Table 5.4 shows that early ACM periods do not necessarily result in lower
nopinone collector mass loadings. For the ACM periods which do not show a
nopinone desorption peak (ACM16.1, and ACM17.1), the minimum nopinone
percentage of the total SOA mass concentration from SMPS measurements
found for the respective experiment temperature is considered (see section
5.4). The nopinone collector mass loadings from these periods are within the

86

range of the ACM periods which show a desorption peak. Thus, the reason for the missing nopinone desorption peak in ACM16.1, and ACM17.1 is not too low nopinone collector mass loading. The lowest nopinone collector mass loading with an ACM desorption peak is $6.67 \cdot 10^{-4}$ μg.

As low collector mass loading is neither the reason for the ACM periods without desorption peak, nor for the observed difference in the partitioning coefficients from before and after nopinone addition, another effect has to account for these findings. For this purpose, further ACM measurements are needed. They should include more ACM periods during the course of one experiment.

Conclusions for the partitioning coefficients of approaches 1 and 2
As the partitioning coefficient derived from ACM measurements shows the temperature behavior expected from theory (e.g. (Pankow, 1994), (Jenkin, 2004)) it is considered the more reliable result than the partitioning coefficients from approach 1. All partitioning coefficients from ACM measurements are higher than expected from theory. This cannot be explained by filter artifacts. Equations 5.1 and 5.2 show that either a lower activity coefficient than expected, or a lower sub-cooled liquid vapor pressure result in the observed difference between the experimental results and theory. However, the experiments show that more nopinone is in the aerosol particle phase than expected from theory.

Table 5.4: Nopinone collector mass loadings for the different ACM measurements. For ACM periods without ACM desorption peak, the nopinone collector mass loadings were calculated from minimum percentage of the total SOA mass from SMPS measurements at the respective experiment temperature T (see chapter 5.4). The given errors for each collector mass loading are the statistical errors. As discussed in chapter 4.2 an offset of $\pm$ 50% of each value has to be considered as a systematic error for each value. Therefore, upper and lower limits are given.

T [K]	ACM period	Nopinone Collector Mass Loading [μg]	Nopinone Collector Mass Loading from SMPS percentage [μg]	Upper Limit [μg]	Lower Limit [μg]
243	ACM18.1	$1.07 \cdot 10^{-3} \pm 1.32 \cdot 10^{-5}$		$1.61 \cdot 10^{-3}$	$5.35 \cdot 10^{-4}$
243	ACM18.2	$2.18 \cdot 10^{-3} \pm 2.75 \cdot 10^{-5}$		$3.27 \cdot 10^{-3}$	$1.09 \cdot 10^{-3}$
258	ACM20.2	$6.67 \cdot 10^{-4} \pm 8.25 \cdot 10^{-6}$		$1.00 \cdot 10^{-3}$	$3.34 \cdot 10^{-4}$
258	ACM25.1	$3.46 \cdot 10^{-3} \pm 4.27 \cdot 10^{-5}$		$5.19 \cdot 10^{-3}$	$1.73 \cdot 10^{-4}$
258	ACM25.2	$1.39 \cdot 10^{-3} \pm 1.99 \cdot 10^{-5}$		$2.09 \cdot 10^{-3}$	$6.95 \cdot 10^{-4}$
273	ACM17.1		$2.10 \cdot 10^{-3} \pm 5.99 \cdot 10^{-4}$	$3.15 \cdot 10^{-3}$	$1.05 \cdot 10^{-3}$
273	ACM17.2	$1.06 \cdot 10^{-3} \pm 2.47 \cdot 10^{-5}$		$1.59 \cdot 10^{-3}$	$5.30 \cdot 10^{-4}$
273	ACM27.1	$1.72 \cdot 10^{-3} \pm 2.14 \cdot 10^{-5}$		$2.58 \cdot 10^{-3}$	$8.60 \cdot 10^{-4}$
303	ACM16.1		$6.80 \cdot 10^{-4} \pm 9.47 \cdot 10^{-5}$	$1.02 \cdot 10^{-3}$	$3.40 \cdot 10^{-4}$
303	ACM16.2	$1.34 \cdot 10^{-3} \pm 1.68 \cdot 10^{-5}$		$2.01 \cdot 10^{-3}$	$6.70 \cdot 10^{-4}$

5.3.2 Other β-Pinene Ozonolysis Products

To find information on other β-pinene ozonolysis products beside nopinone the correlation matrix from β-pinene fragmentation is further investigated. β-pinene products should show a Pearson correlation coefficient between -1 and -0.6. Despite the good results for the fragmentation, the matrix correlation does not result in correlation coefficients in that range for the correlation with $C_{10}H_{17}^+$. A coefficient of -0.44 can be found for $C_9H_{15}O^+$ (nopinone) and $C_9H_{13}O^+$, identified as the β-pinene ozonolysis product Bicyclo[3,1,1]hept-3-ene-2-one in Hohaus (2009).

The incident that a known β-pinene ozonolysis product like nopinone shows a correlation coefficient of -0.44 leads to the conclusion that the used correlation method is not appropriate to detect ozonolysis oxidation products reliably. A reason for that is that the different β-pinene ozonolysis products are built on different time scales. This results in a nonlinear relation between the time evolution of β-pinene and its ozonolysis products. As the Pearson correlation coefficient is only defined for linear correlation, the matrix correlation does not result in the β-pinene ozonolysis products.

Therefore, a search for β-pinene ozonolysis products based on (Hohaus, 2009) was conducted. Results can be seen in Table 5.5. Hohaus (2009) identified several β-pinene ozonolysis products in the particle phase. For these products, the PTR-ToF-MS gas phase data of the Hohaus (2009) experiment was searched. Additionally, the PTR-ToF-MS gas phase data and ACM particle phase data from the experiment on 2009/11/18 at the AIDA chamber were searched for these products. This experiment was conducted at 243K. Therefore, β-pinene ozonolysis products are more likely to be in the aerosol particle phase as in experiments at higher temperatures. The second ACM desorption period of that day shows a clear nopinone desorption peak. Thus, it is considered suitable to find β-pinene ozonolysis products. For the search of products in the gas phase, the whole gas phase data of that day was examined. For the comparison with the results from Hohaus (2009) it has to be kept in mind that $\sim$ 600 ppb of β-pinene were injected into the Jülich Aerosol chamber, whereas the β-pinene mixing ratios in AIDA were below a tenth of that value. A high β-pinene mixing ratio enhances particle formation. Further, it has to be mentioned that $C_9H_{15}O_2^+$, which was detected in the gas phase data of this work but not in the particulate phase, was identified to be a β-pinene and α-pinene fragment (see 4.3.1 and 4.3.2). As Hohaus (2009) uses a combination of ACM and GC-MS it is clear that his finding cannot be ascribed to fragmentation. This leads to the conclusion that $C_9H_{15}O_2^+$ can be found in the aerosol particle phase for high but not for low β-pinene concentrations.

Table 5.5: β-pinene ozonolysis products of an experiment at the Jülich Aerosol Chamber (Hohaus, 2009) compared to the findings of this work.

β-pinene ozonolysis products in the particle phase from (Hohaus, 2009)	Ionized compound	Mass of the ionized compound in [amu]	Detected in PTR-ToF-MS gas phase Hohaus, 2009	Detected in PTR-ToF-MS gas phase, this work	Detected in ACM particle phase this work,
acetone	$C_3H_7O^+$	59.050	yes	yes	yes
bicyclo[3.1.1]hept-3-ene-2-one	$C_9H_{13}O^+$	137.097	yes	yes	yes
nopinone	$C_9H_{15}O^+$	139.112	yes	yes	yes
3-oxonopinone	$C_9H_{13}O_2^+$	153.092	yes	yes	yes
myrtanal	$C_{10}H_{17}O^+$	153.128	no	no	no
myrtenol	$C_{10}H_{17}O^+$	153.128	no	no	no
1-hydroxynopinone	$C_9H_{15}O_2^+$	155.107	yes	yes	no
3,7-dihydroxy-nopinone	$C_9H_{15}O_3^+$	171.102	yes	no	no

Table 5.5 shows that from the list of identified β-pinene ozonolysis products in the aerosol particle phase from Hohaus (2009) for acetone (at $C_3H_7O^+$), bicyclo[3,1,1]hept-3-ene-2-one (at $C_9H_{13}O^+$), nopinone (at $C_9H_{15}O^+$), 3-oxonopinone (at $C_9H_{13}O_2^+$), and 1-hydroxynopinone (at $C_9H_{15}O_2^+$) signals were found in the gas phase in the experiment of 2009/11/18. The second ACM desorption phase of that day shows desorption peak signals for $C_3H_7O^+$, $C_9H_{13}O^+$, $C_9H_{15}O^+$, and $C_9H_{13}O_2^+$. It has to be mentioned that except for nopinone and acetone, the detected signals were close to the detection limit. So no reliable partitioning coefficient could be calculated for these compounds. Regarding the data for acetone, the ACM desorption process generates $C_3H_7O^+$ signal due to the breaking up of other compounds. The exact sources contributing to the $C_3H_7O^+$ desorption peak are not determined so far. Therefore, a partitioning coefficient calculated from that data would not represent the gas-to-particle partitioning of acetone.

5.4 ACM - SMPS comparison

To determine the SOA fraction detected by the ACM, a full list of compounds found in the ACM desorption periods has to be determined. As a first step, the raw data of the second ACM desorption phase on 2009/11/18 was searched for ions showing a desorption peak. This was done to reduce the amount of compounds for which the mixing ratios had to be calculated. Afterwards, the raw signal of the resulting ions was processed with Equation 4.1. A general reaction rate of $2 \cdot 10^{-9}$ $\frac{cm^3}{s}$ was assumed. As only the ion signals are investigated without considerations concerning the fragmentation, the fragmentation factor was set to one. This procedure normalized the signals on primary ion and PTR chamber condition changes. Then, it was checked again, if the ions show a clear desorption peak. The resulting list of ions can be found in appendix F. The mixing ratios of the ions were summed up to the full SOA signal in the desorption areas. The desorption peak data analysis was conducted in analogy to the one of nopinone. For the calculation of the SOA mass concentrations, the average molecular mass of 117.55 $\frac{g}{mol}$ resulting of the found ions was used. The percentage of total SOA detected by ACM is shown in Table 5.6. Also, Table 5.6 summarizes the percentage contribution of nopinone measured by ACM-PTR-ToF-MS to the overall SOA mass as derived from SMPS data. The SMPS-SOA mass concentrations considered here are the averages over the respective ACM sampling times.

Table 5.6: SOA mass and nopinone fractions of the total SOA mass from SMPS. Given are the statistical errors, as well as the upper and lower limits resulting from the systematic error discussed in chapter 4.2.

T [k]	ACM Desorption Phase	Percentage of total ACM signal to SOA from SMPS [%]	Upper Limit [%]	Lower Limit [%]	Percentage of nopinone from ACM to SOA from SMPS [%]	Upper Limit [%]	Lower Limit [%]
243	ACM18.1	21.31 ±4.81	31.97	10.66	0.63±0.14	0.95	0.32
243	ACM18.2	12.67 ±1.42	19.01	6.34	0.64±0.07	1.41	0.47
258	ACM20.1	19.97 ±4.24	29.96	9.99			
258	ACM20.2	15.06 ±1.50	22.59	7.53	0.06±0.01	0.09	0.03
258	ACM25.1	21.44 ±2.99	32.16	10.72	0.68±0.10	1.02	0.34
258	ACM25.2	17.45 ±0.38	26.18	8.73	0.54±0.01	0.81	0.27
273	ACM17.2	13.73 ±0.90	20.60	6.87	0.45±0.03	0.68	0.23
273	ACM27.1	12.02 ±2.54	18.03	6.01	0.34±0.07	0.51	0.17
303	ACM16.1	16.00 ±1.59	24.00	8.00			
303	ACM16.2	9.19 ±0.91	13.79	4.60	0.24±0.02	0.36	0.12

The total detected ACM-SOA signal ranges between 9.19 ± 0.91 % and 21.44 ±2.99 % of the SMPS derived SOA mass. The high variation in the detected SOA fraction detectable by ACM-PTR-ToF-MS can partly be explained from the shape of the desorption peak. Different from the nopinone desorption peaks, in some ACM desorption periods the total SOA peak decreased very slowly after its maximum and had not reached the baseline value at the end of the desorption period. Hence, not the complete signal could be considered by the integration of the desorption peak. It can be concluded that some of the SOA compounds evaporated slower from the ACM collector surface than others. Therefore, the desorption periods for investigations of compounds other than nopinone should be longer than the ones conducted in this work, or the temperature used for desorption should be higher.

The total SOA mass measured with the combination of ACM and GC-MS by Hohaus et al. (2010) shows a range between 6 % and 11 % of the total SOA mass. The fractions from the combination of PTR-ToF-MS and ACM are slightly higher. This may result from the fact that the PTR-ToF-MS is less limited in measuring oxiginated compounds and compounds at high molecular weight in comparison to the GC-MS set-up used by Hohaus et al. (2010).

The percentages of nopinone compared to the total SOA mass from SMPS in this work vary between 0.06 ± 0.01 % and 0.68 ± 0.10 %. Considering that Hohaus et al. (2010) investigated one experiment at 294 K these values compare well to the range of 0.1 % to 0.3 % found by Hohaus et al. (2010), derived with the combination of ACM and GC-MS.

5.5 Scientific findings of the α- and β-pinene ozonolysis experiments

Within this work, two α- and five β-pinene ozonolysis experiments were performed at the AIDA chamber of the Karlsruhe Institute of Technology (KIT). To investigate the SOA formation a first-time combination of a new aerosol collection technique and a high-resolution PTR-ToF-MS was used.

From α-pinene ozonolysis experiments the ion $C_9H_{15}O_2^+$ was found on m/z 155.107 amu in the aerosol particle phase data. It is interpreted as a PTR-ToF-MS fragment of the major α-pinene ozonolysis product pinonaldehyde. In the β-pinene ozonolysis experiments following compounds were found in the aerosol particle phase:

Table 5.7: β-pinene ozonolysis products in the aerosol particle phase.

identified products in the particle phase	Ionized compound	Mass of the ionized compound in [amu]
acetone	$C_3H_7O^+$	59.050
bicyclo[3,1,1]hept-3-ene-2-one	$C_9H_{13}O^+$	137.097
nopinone	$C_9H_{15}O^+$	139.112
3-oxonopinone	$C_9H_{13}O_2^+$	153.092

As the major point of this work, the nopinone partitioning coefficient and its temperature dependence was determined. Findings from the ACM show a temperature behavior in accordance with the semi-empirical form of the Clausius-Clapeyron equation, as expected from theory. Nevertheless, the experimentally determined partitioning coefficients are higher by one order of magnitude than calculated based on theoretical work. Concluding from that, more nopinone is in the aerosol particle phase than expected from theory. This is likely a representative result for semivolatile compounds and may in part explain why models tend to underpredict SOA. Therefore, the experimental results for the nopinone partitioning coefficient from this work can be used to improve model efforts which consider the contribution of biogenic compounds to SOA formation.

Chapter 6

Summary and Outlook

Summary

Organic aerosol makes up between 20 % and 90 % of the total submicron particulate mass in the atmosphere. It is considered to be of major importance in understanding the different effects of aerosols on climate. Despite the ongoing efforts, models still tend to underpredict organic aerosol mass. SOA from biogenic VOCs contributes an important amount to the total organic aerosol mass in the atmosphere. One key point in understanding the formation of SOA is the investigation of the gas-to-particle partitioning of semivolatile oxidation products of VOCs.

In the present work, a new aerosol collection technique was coupled to a high-resolution gas phase detector. This allowed a quasi-online compound-specific measurement of the aerosol particle phase. The Aerosol Collection Module (ACM) is a new device to collect atmospheric aerosols, convert them into the gas phase and transfer them to a gas phase detector for analysis. Within the ACM, the aerosol particles are separated from the gas phase and collected on a cooled collector surface. After the collection time, the aerosol particles are converted to the gas phase via thermal desorption and transferred to a gas phase detector. Different collection times were applied during this work. The minimum collection time span was 25 min. Generally, the minimum time span possible for collection is determined by the SOA mass concentration in the sample and the device-specific minimum collector mass loading. In the experiments presented in this work, the lowest detectable collector mass loading was $6.67 \cdot 10^{-4}$ μg for nopinone.

In this work, a first-time coupling of the ACM and a high-resolution PTR-ToF-MS was conducted and used in α - and β-pinene ozonolysis experiments at the AIDA chamber of the KIT, Karlsruhe, to investigate the formation

of SOA. As the PTR-ToF-MS is a relatively new gas phase detector, a data analysis routine had to be developed during this work. It was based on the data analysis routines for high resolution Aerosol Mass Spectrometer (AMS) data. Furthermore, a close investigation of the fragmentation within the PTR-ToF-MS drift tube had to be conducted to derive mixing ratios in the AIDA chamber for α-pinene, β-pinene, and nopinone. The ACM measurements were used to investigate α - and β-pinene ozonolysis products in the aerosol particle phase.

The experiments at the AIDA chamber were conducted at temperatures between 243K and 303 K. For the major β-pinene ozonolysis product nopinone, the partitioning coefficient and its temperature dependence was investigated. The features of ACM and PTR-ToF-MS were used to determine the partitioning coefficient with two different experimental approaches. In the first approach, the PTR-ToF-MS was operated in combination with a filter set-up according to Tillmann et al. (2010). The second approach used the combination of ACM and PTR-ToF-MS. Results were compared to experimental data from (Hohaus, 2009; Hohaus et al., 2010) and to partitioning coefficients from literature, which were derived from theory. Literature on the nopinone partitioning coefficient at different temperatures is relatively sparse. Thus, to derive a comparison of the temperature dependence, the partitioning coefficients at the experiment temperatures of this work were calculated following theory.

The partitioning coefficients from the two experimental approaches conducted in this work showed a difference of 1 to 3 orders of magnitude. The partitioning coefficients from PTR-ToF-MS measurements with the filter set-up were higher than those derived from ACM measurements. The filter set-up approach compared well to the modeled partitioning coefficients from Chen and Griffin (2005) but not with Jenkin (2004). Furthermore, they showed an unexpected linear temperature dependence. Thus, it is assumed that these results are mainly influenced by inconsistencies in the performance of the filter set-up method.

The temperature dependence of the nopinone partitioning coefficient from ACM measurements can be described by the equations used in Jenkin (2004). Nevertheless, the theoretically derived values are 1 order of magnitude below the ones determined using the ACM. Therefore, the experimental data of this work leads to the conclusion that the amount of nopinone in SOA is underestimated by theory.

In addition to the work described above, two improvements of the ACM collection section were conducted. In the old set-up, the collector is cooled with liquid nitrogen. This ensures low collection temperatures, but it also makes the instrument-dependent on a permanent liquid nitrogen supply du-

ring collection periods. To make the device more independent, the cooling is conducted via a peltier element in a new set-up.

In the experiments at the AIDA chamber, the desorption process which transforms the collected aerosol particles into the gas phase was conducted in one step. On the one hand, this gives compounds which evaporate at low temperatures excess energy, which can lead to a breaking-up of these compounds and makes their analysis more complex. On the other hand, a step-wise heating would allow to investigate compounds according to their evaporation temperature. Therefore, a semi-automatic step-wise heating procedure was developed and installed at the ACM collection section. The general performance of the new set-up was tested under laboratory conditions.

Outlook

The next step in improving the ACM is to perform experiments with the newly developed set-up of the ACM collection section. Furthermore, short sampling times in the ACM are desirable to provide a higher time resolution in the aerosol particle measurements. For this purpose, the limit of minimum collector mass loading which still ensures a significant desorption peak signal has to be determined. In addition, a virtual impactor at the ACM inlet system is an interesting possibility for pre-concentrating the aerosol, which should be explored to further shorten sampling times.

From the α-pinene experiments presented in this work it can be seen that an α-pinene ozonolysis experiment at a temperature above 273 K could be used for a detailed pinonaldehyde fragmentation study. From experiments at several temperatures above 273 K, the partitioning coefficient of pinonaldehyde could be determined in analogy to the nopinone partitioning coefficient in this work. Integrating the findings on the partitioning coefficient from this work holds the opportunity for improvements of model studies considering the formation of SOA. In general, the combination of ACM and PTR-ToF-MS provides interesting opportunities for detailed compound-specific studies of the chemistry and the formation of organic aerosol.

Appendix A

Detailed descriptions of the experiment processes

Experiment SOA09-06

$<T> = (303)$ K; $P = (1000)$ hPa; $[H_2O] = (\sim13000)$ ppm; r. h. $= (\sim30)$ %

Date	Time (Start)	Time (End)	Activity	SOA µg/m^3
15.11.09			Filling with water vapour and synthetic air	
16.11.09				
	09:36	10:06	+ Cyclohexane (Saturator at 25°C, 9 SLM)	
	10:22	10:26	+ Ozone (Sorbios 80% in O$_2$, t=10s) with 5 SLM	530ppb
	10:43	10:45	+ β-Pinene (2.0 hPa* in 2l) with 10 SLM*	(49ppb)
	13:00	14:30	Filter sampling (MZ, FZJ, IfT)	
	13:25	13:50	Meeting (seminar room)	
	14:36	14:56	+ Nopinone (Saturator at 50°C, 8 SLM)	(20ppb)
	15:00	16:00	Filter sampling (MZ, FZJ, IfT)	
	16:10	16:13	+ Ozone (Sorbios 80% in O$_2$, t=10s) with 5 SLM	1.1ppm
	16:21	16:23	+ β-Pinene (2.0 hPa* in 2l) with 10 SLM	(49ppb)
	17:30	19:00	Filter sampling (MZ, FZJ, IfT)	
	19:00		Start pumping, flushing, filling with water vapour, refilling with synthetic air and cooling to 273 K.	

*Gas canisters samples are take every hour since addition of beta-pinene

Experiment SOA09-07

$<T> = (273)$ K; $P = (1000)$ hPa; $[H_2O] = (\sim4080)$ ppm; r. h. = (~60) %

Date	Time (Start)	Time (End)	Activity	SOA µg/m^3
16.11.09			Filling with water vapour and synthetic air	
17.11.09				
	09:31	10:02	+ Cyclohexane (Saturator at 25°C, 9 SLM)	
	10:08	10:12	+ Ozone (Sorbios 80% in O$_2$, t=15s) with 5 SLM	710ppb
	10:22	10:26	+ β-Pinene (2.0 hPa* in 2l) with 10 SLM*	(44ppb)
	12:19	12:23	+ Ozone (Sorbios 80% in O$_2$, t=5s) with 5 SLM	970ppb
	13:00	14:30	Filter sampling (MZ, FZJ, IfT)	
	13:30		Meeting (seminar room)	
	14:45	14:52	+ Nopinone (Saturator at 50°C, 8 SLM)	(20ppb)
	15:00	16:00	Filter sampling (MZ, FZJ, IfT)	
	16:06	16:10	+ Ozone (Sorbios 80% in O$_2$, t=60s) with 5 SLM	3.7ppm
	16:25	16:27	+ β-Pinene (2.0 hPa* in 2l) with 10 SLM*	(44ppb)
	17:00	18:00	Filter sampling (MZ, FZJ, IfT)	
	18:15		Start pumping, flushing, filling with water vapour, refilling with synthetic air and cooling to 243 K.	

*Gas canisters samples are take every hour since addition of beta-pinene

Experiment SOA09-08

$\langle T \rangle$ = (243) K; P = (1000) hPa; $[H_2O]$ = (~400) ppm; r. h. = (~80) %

Date	Time (Start)	Time (End)	Activity	SOA µg/m^3
17.11.09			Filling with water vapour and synthetic air	
18.11.09				
	09:39	10:10	+ Cyclohexane (Saturator at 25°C, 9 SLM)	
	10:16	10:19	+ Ozone (Sorbios 80% in O_2, t=20s) with 5 SLM	830ppb
	10:30	10:32	+ β-Pinene (2.0 hPa* in 2l) with 10 SLM*	(39ppb)
	11:38	11:40	+ Ozone (Sorbios 80% in O_2, t=19s) with 5 SLM	1.57ppm
	13:00	14:30	Filter sampling (MZ, FZJ, IfT)	
	13:30	14:30	Seminar by Dr. Tajiri (MRI)	
	14:34	14:39	+ Nopinone (Saturator at 50°C, 8 SLM)	(20ppb)
	15:00	16:00	Filter sampling (MZ, FZJ, IfT)	
	15:15		Meeting (seminar room)	
	16:03	16:05	+ Ozone (Sorbios 80% in O_2, t=20s) with 5 SLM	2.2ppm
	16:14	16:16	+ β-Pinene (2.0 hPa* in 2l) with 10 SLM*	(39ppb)
	17:00	18:30	Filter sampling (MZ, FZJ, IfT)	
	18:30		Start pumping, flushing, filling with water vapour, refilling with synthetic air and heating to 273 K.	

*Gas canisters samples are take every hour since addition of beta-pinene

Experiment SOA09-09

$<T> = (273)$ K; $P = (1000)$ hPa; $[H_2O] = (\sim 5200)$ ppm; r. $h._{ice} = (\sim 60)$ %

Date	Time (Start)	Time (End)	Activity	SOA µg/m³
18.11.09			Filling with water vapour and synthetic air	
19.11.09				
	10:02	10:04	+ 2-Butanol (10*100/1010 in 1 l) with 10 SLM	
	10:42	10:42:30	+ DOP Droplets via Atomizer (1bar)	
	10:59	10:59:30	+ DOP Droplets via Atomizer (1bar)	
	11:12	11:15	+ Ozone (Sorbios 80% in O2, t=20s) with 5 SLM	940ppb
	11:31	12:00	+ TME (1000ppm/N2) with (100)/60 SCCM	
	12:32	12:37	+ Nopinone (Saturator at 50°C, 8 SLM)	
	14:30	15:20	Meeting (Seminar room)	
	15:23	15:24	+ DOP Droplets via Atomizer (1bar)	
	15:50		+ Ozone (Sorbios 80% in O2, t=5s) with 5 SLM	1.06ppm
	17:21	19:06	+ TME (1000ppm/N2) with 60 SCCM	
	17:47	18:47	Filter sampling (MZ, FZJ, IfT)	
	19:30		Start pumping, flushing, filling with water vapour, refilling with synthetic air and cooling to 258 K.	

Experiment SOA09-10

<T> = (258) K; P = (1000) hPa; [H_2O] = (~1200) ppm; r. h. = (~70) %

Date	Time (Start)	Time (End)	Activity	SOA µg/m^3
19.11.09			Filling with water vapour and synthetic air	
20.11.09				
	09:23	09:54	+ Cyclohexane (Saturator at 25°C, 9 SLM)	
	10:09	10:12	+ Ozone (Sorbios 80% in O2, t=7s) with 5 SLM	333ppb
	10:24	10:26	+ α-Pinen (2.0 hPa*191/1006 in 1l) with 10 SLM	4 ppb
	11:54	11:56	+ α-Pinen (2.0 hPa/1l) with 10 SLM	21 ppb
	13:30	14:30	Filter sampling (MZ, FZJ, IfT)	
	14:37	14:42	+ Nopinone (Saturator at 50°C, 8 SLM)	
	15:00	16:00	Meeting (cellar room)	
	17:00	17:50	+ Pinonaldehyde (Saturator at 65°C, 8 SLM)	
	18:00	19:00	Aerosol characterisation	
	19:20		Start pumping, flushing, filling with water vapour, refilling with synthetic air and heating to 293 K.	

Experiment SOA09-13

<T> = (258.1±0.1) K; P = (1000±2) hPa; [H_2O] = (~1100) ppm; r. h. = (~70) %

Date	Time (Start)	Time (End)	Activity	SOA µg/m^3
24.11.09			Filling with water vapour and synthetic air	
25.11.09				
	09:34	10:07	+ Cyclohexane (Saturator at 25°C, 9 SLM)	
	10:14	10:21	+ Ozone (Sorbios 80% in O_2, t=18s) with 5 SLM	850ppb
	10:33	10:35	+ β-Pinene (2.0 hPa* in 2l) with 10 SLM*	41.4 ppb
	13:00	14:30	Filter sampling (MZ, FZJ, IfT)	
	14:10	14:30	Meeting (seminar room)	
	15:01	15:07	+ Nopinone (Saturator at 50°C, 8 SLM)	
	15:30	17:00	Filter sampling (MZ, FZJ, IfT)	
	17:00		Start pumping, flushing, filling with water vapour, refilling with synthetic air and heating to 273 K.	

*Gas canisters samples are take every hour since addition of beta-pinene

APPENDIX A. DETAILED DESCRIPTIONS OF THE EXPERIMENT PROCESSES

Experiment SOA09-14

$\langle T \rangle$ = (273) K; P = (1000) hPa; [H_2O] = (~4500) ppm; r. h. = (~60) %

Date	Time (Start)	Time (End)	Activity	SOA μg/m^3
25.11.09			Filling with water vapour and nitrogen	
26.11.09				
	09:24	09:54	+ Cyclohexane (Saturator at 25°C, 9 SLM)	
	10:01	10:04	+ Ozone (Sorbios 80% in O2, t=6s) with 5 SLM	310ppb
	10:20	10:23	+ α-Pinen (2.0 hPa*250/1007 in 1l) with 10 SLM	(5.5ppb)
	11:53	11:55	+ α-Pinen (2.0 hPa/1l) with 10 SLM	(22ppb)
	13:00	14:30	Filter sampling (MZ, FZJ, IfT)	
	15:15		Meeting	
			Filter sampling as required	
	18:00		Start pumping, flushing, filling with water vapour, refilling with synthetic air and cooling to 273 K.	

Experiment SOA09-15

$\langle T \rangle$ = (273) K; P = (1000) hPa; [H_2O] = (~4000) ppm; r. h. = (~60) %

Date	Time (Start)	Time (End)	Activity	SOA μg/m^3
26.11.09			Filling with water vapour and nitrogen (5.0)	
27.11.09				
	09:09	09:39	+ Cyclohexane (Saturator at 25°C, 9 SLM)	
	09:48	09:52	+ Ozone (Sorbios 80% in O_2, t=18s) with 5 SLM	900ppb
	10:00	10:02	+ β-Pinene (2.0 hPa* in 2l) with 10 SLM	(44ppb)
	10:30		Meeting (seminar room)	
	13:00	14:30	Filter sampling (MZ, FZJ, IfT)	
	15:15		Start pumping, flushing, refilling with synthetic air and warming to 295 K.	

Appendix B

Pearson correlation matrix for β-pinene fragmentation
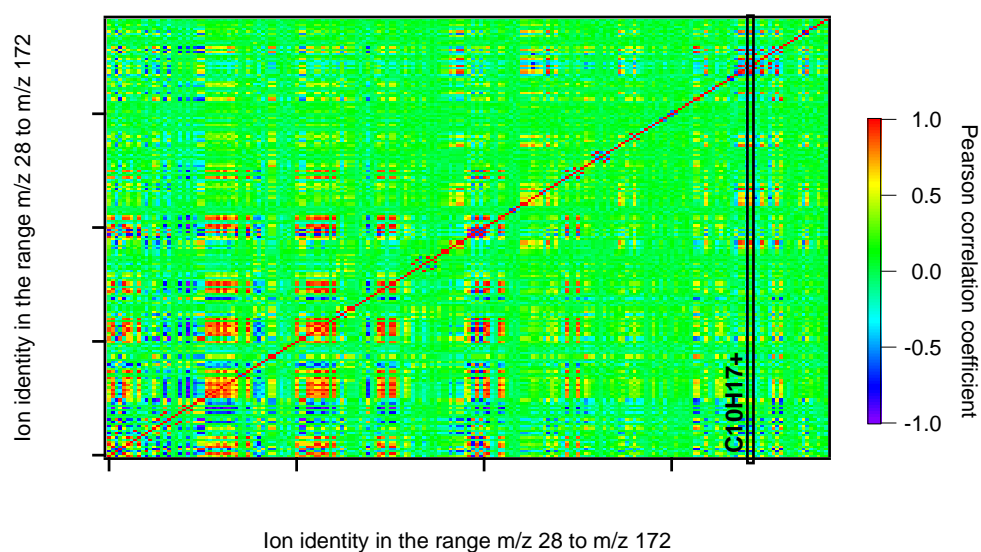
Figure B.1: Pearson correlation matrix for β-pinene fragmentation in the PTR-ToF-MS drifttube. The color codes shows the Pearson correlation coefficients for all ions in the mass range between m/z 28 and m/z 172 with each other. The red diagonal indicates the ions correlated with themselves, therefore showing a coefficient of one. The information for β-pinene fragmentation is highlighted in the black box, enclosing the correlation coefficient values for all ions with the β-pinene parent ion $C_{10}H_{17}^+$.

APPENDIX B. PEARSON CORRELATION MATRIX FOR β-PINENE FRAGMENTATION

Appendix C

Ion identities and Pearson correlation coefficient for ions correlated to $C_{10}H_{17}^+$

Ion number	Ion	Pearson Correlation Coefficient	Ion number	Ion	Pearson Correlation Coefficient
1	H5O2	0.09	31	C4H5	0.63
2	j13CC2H	0.01	32	j13CC3H5	0.63
3	C3H2	0.24	33	C4H6	-0.04
4	C3H3	0.61	34	H3OH4O2	-0.15
5	j13CC2H3	0.61	35	C4H7	0.33
6	C3H4	0.01	36	j13CC3H7	0.33
7	C2HO	-0.1	37	C4H8	-0.13
8	j13CC2H4	0.01	38	C4H9	0.23
9	C3H5	0.13	39	C3H6O	-0.07
10	C2H2O	-0.07	40	j13CC3H9	0.23
11	j13CC2H5	0.13	41	C3H7O	-0.01
12	C3H6	-0.22	42	C2H6NO	0.27
13	C2H3O	0.01	43	j13CC2H7O	-0.01
14	C3H7	0.36	44	C2H5O2	0.15
15	CH2NO	-0.04	45	j13CCH5O2	0.15
16	C2H4O	0.04	46	C2H6O2	0.09
17	j13CC2H7	0.36	47	C5H3	-0.16
18	C3H8	0.17	48	C4HO	0.08
19	C2H5O	0.07	49	C5H5	0.21
20	NO2	-0.29	50	C4H2O	-0.08
21	CH4NO	0.15	51	C5H6	0.27
22	C2H6O	-0.09	52	C5H7	0.34
23	CH3O2	-0.15	53	C5H8	0.09
24	j13CH3O2	-0.15	54	C4H5O	-0.1
25	CH4O2	-0.07	55	C5H9	0.01
26	C4H3	0.11	56	j13CC4H9	0.01
27	Cr	-0.05	57	C5H10	-0.13
28	C3O	0.24	58	C3H3O2	0.14
29	C4H4	0.11	59	C4H7O	0.34
30	C3HO	0.21	60	C5H11	0.12

Table C.1: List of ion identities for ions correlated to $C_{10}H_{17}^+$ and Pearson correlation coefficient to determine the β-pinene fragmentation (see section 4.3.1).

Ion number	Ion	Pearson Correlation Coefficient	Ion number	Ion	Pearson Correlation Coefficient
61	C3H5O2	-0.04	91	j13CC6H7	0.76
62	C4H9O	0.09	92	C7H8	0.63
63	C2H4NO2	0.2	93	C7H9	0.72
64	j13CC2H5O2	-0.04	94	C7H10	0.47
65	C3H6O2	-0.06	95	C5H3O2	0.61
66	j13CC3H9O	0.09	96	C6H7O	-0.22
67	j13CC2H6O2	-0.06	97	C7H11	0.96
68	C3H7O2	0.15	98	C6H8O	0.12
69	C6H6	0.27	99	C7H12	0.67
70	j13CC5H6	0.27	100	C5H5O2	-0.02
71	C6H7	0.76	101	C6H9O	-0.08
72	C6H8	0.47	102	C7H13	0.24
73	C6H9	0.93	103	C5H6O2	0.04
74	j13CC5H9	0.93	104	C6H10O	-0.05
75	C6H10	0.18	105	j13CC6H13	0.24
76	C4H3O2	0.46	106	j13CC5H10O	-0.05
77	C5H7O	-0.46	107	C6H11O	-0.05
78	C6H11	0.25	108	C6H12O	-0.02
79	j13CC4H7O	-0.46	109	C4H5O3	0.06
80	j13CC5H11	0.25	110	C5H9O2	0.02
81	C6H12	-0.04	111	C6H13O	0
82	C4H5O2	-0.07	112	j13CC3H5O3	0.06
83	C5H9O	-0.08	113	j13CC4H9O2	0.02
84	C6H13	0.18	114	C8H9	0.07
85	C6H14	0.15	115	C7H7O	-0.07
86	C4H7O2	0.01	116	C8H11	0.85
87	C3H5O3	0.03	117	C8H12	0.54
88	C7H5	0.11	118	C6H5O2	-0.12
89	C4H9O2	-0.03	119	C7H9O	-0.25
90	C7H7	0.76	120	C8H13	0.65

Ion number	Ion	Pearson Correlation Coefficient	Ion number	Ion	Pearson Correlation Coefficient
121	j13CC6H9O	-0.25	151	C10H17	1
122	C7H10O	-0.1	152	C9H13j17O	-0.44
123	C8H14	0.02	153	C9H14O	-0.43
124	C6H7O2	0.11	154	j13CC9H17	1
125	C7H11O	-0.04	155	C10H18	0.37
126	C8H15	0	156	C9H15O	-0.44
127	C5H5O3	0.15	157	j13CC8H15O	-0.33
128	C6H9O2	0.01	158	C9H16O	1
129	C4H3O4	0.02	159	C8H5O3	-0.33
130	C5H7O3	0.14	160	C10H13O	0.01
131	C6H11O2	0.02	161	C9H11O2	0.16
132	C6H12O2	-0.04	162	C10H15O	0.12
133	C9H11	0.2	163	C9H13O2	-0.05
134	C9H12	0.04	164	C9H15NO	0.5
135	C5H13O3	0.08	165	C12H11	-0.54
136	C9H13	-0.32	166	C9H15O2	0.84
137	C9H14	-0.25	167	C10H15O2	-0.15
138	C8H11O	-0.21	168	C9H13O3	-0.02
139	C9H15	0.82	169	C10H17O2	0.45
140	C6H5O3	0.17	170	j13CC9H17O2	0.19
141	C7H9O2	0.1	171	C9H15O3	0.28
142	C8H13O	-0.25			
143	C8H14O	0.06			
144	C7H11O2	-0.02			
145	C8H3O2	0.3			
146	C4H5NO4	-0.13			
147	C9H11O	-0.58			
148	C10H15	0.98			
149	C10H16	0.91			
150	C9H13O	-0.44			

Appendix D

Mixing ratio error

The statistical error ΔC_{ppbV} for the mixing ratio in ppb is calculated from gaussian error propagtion of equation 4.1 in combination with equation 4.2 for the calibration factor CF.

$$\Delta C_{ppbV}^2 =$$

$$\left(1.657 \cdot 10^{-11} \frac{U_{drift} T_{drift}^2}{k \cdot p_{drift}^2} \cdot \frac{C^+}{H_3O^+} \cdot \frac{TR_{H_3O^+}}{TR_{C^+}} \cdot FF \cdot (m/z - 21) \cdot \Delta b \right)^2 +$$

$$C_{ppbV}^2 \cdot \left(\left(\frac{\Delta U_{drift}}{U_{drift}} \right)^2 + \left(2\frac{\Delta T_{drift}}{T_{drift}} \right)^2 + \left(\frac{\Delta C^+}{C^+} \right)^2 + \left(\frac{\Delta FF}{FF} \right)^2 + \right.$$

$$\left. \left(2\frac{\Delta p_{drift}}{p_{drift}} \right)^2 + \left(\frac{\Delta H_3O^+}{H_3O^+} \right)^2 \right)$$

ΔC_{ppbV}	Error of the concentration of a compound in $[ppb]$
$1.657 \cdot 10^{-11}$	Constant factor from standard conditions
	and device-specific values (see chapter 4.1 for details)
U_{drift}	Voltage in the PTR-ToF-MS drifttube in $[V]$
T_{drift}	Temperature in the PTR-ToF-MS drifttube in $[K]$
k	Reaction rate of the specific ion with H_3O^+ in $\left[\frac{cm^3}{s} \right]$
	(see table 4.1)
p_{drift}	Pressure in the PTR-ToF-MS drifttube in $[mbar]$

C^+ Concentration of the specific ion

from the PTR-ToF-MS signal in $\left[\dfrac{1}{s}\right]$

H_3O^+ Concentration of the primary ion H_3O^+

from the PTR-ToF-MS signal in $\left[\dfrac{1}{s}\right]$

TR_{C^+} Transmission of the specific ion   (see section 4.2)

$TR_{H_3O^+}$ Transmission of the primary ion H_3O^+ (see section 4.2)

FF Fragmentation factor of the

respective compound (see section 4.3)

m/z mass to charge ratio of the ion of a compound in $[amu]$

Δb Error of the slope of the BTX-correction curve (see section 4.2)

C_{ppbV} Concentration of a compound in $[ppb]$

ΔU_{drift} Error of the voltage in the PTR-ToF-MS drifttube in $[V]$

ΔT_{drift} Error of the temperature in the PTR-ToF-MS drifttube in $[K]$

ΔC^+ Error of the concentration of the specific ion

from the PTR-ToF-MS signal in $\left[\dfrac{1}{s}\right]$

ΔFF Error of the fragmentation factor

of the respective compound

Δp_{drift} Error of the pressure in the PTR-ToF-MS drifttube in $[mbar]$

ΔH_3O^+ Error of the concentration of the primary ion H_3O^+

from the PTR-ToF-MS signal in $\left[\dfrac{1}{s}\right]$

Appendix E

Fragments from ionization of $C_{10}H_{16}$ with O_2^+
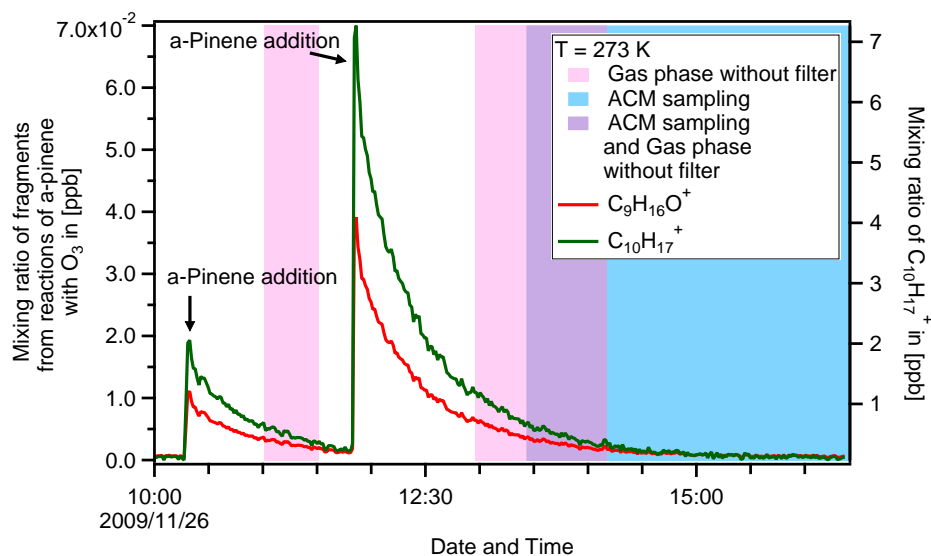
Figure E.1: Experiment from 2009/11/26. $C_9H_{16}O^+$ signal (left axis) and $C_{10}H_{17}^+$ signal (right axis) in ppb. The pearson correlation coefficient of $C_9H_{16}O^+$ with $C_{10}H_{17}^+$ is 1. Therefore, $C_9H_{16}O^+$ is an identified fragment of α-pinene . Nevertheless, it originates from the reaction of $C_{10}H_{16}$ with O_2^+ instead of H_3O^+. The low signal of $C_9H_{16}O^+$ in comparison to the $C_{10}H_{17}^+$ signal (please note the left scale for $C_9H_{16}O^+$ and the right scale for $C_{10}H_{17}^+$) leads to the conclusion that ionization with O_2^+ in the drifttube is subordinate to ionization with H_3O^+ , as expected. However, for experiments where O_2^+ is chosen as primary ion in the PTR-ToF-MS, the results indicate that $C_9H_{16}O^+$ can be considered to be one of the major α-pinene fragments.

Appendix F

Ions in the aerosol particle phase of a β-pinene experiment at 243 K

Table F.1: List of ions found in the aerosol particle phase in ACM18.2 on 2009/11/18 (see section 5.4).

Ion	m/z $\left[\frac{g}{mol}\right]$
$C_3H_7O^+$	59.05
$C^{13}C_2H_7O^+$	60.05
$C_6H_7^+$	79.05
$C_6H_9^+$	81.07
$C^{13}C_5H_9^+$	82.07
$C_7H_9^+$	93.07
$C_7H_{11}^+$	95.09
$C_6H_{11}O^+$	99.08
$C_9H_{13}^+$	121.10
$C_9H_{13}O^+$	137.10
$C_9H_{15}O^+$	139.11
$C^{13}C_8H_{15}O^+$	140.12
$C_8H_5O_3^+$	149.02
$C_9H_{13}O_2^+$	153.09
$C_{10}H_{17}O_2^+$	169.12
$C^{13}C_9H_{17}O_2^+$	170.13
$C_9H_{15}O_3^+$	171.10

APPENDIX F. IONS IN THE AEROSOL PARTICLE PHASE OF A
β-PINENE EXPERIMENT AT 243 K

References

Cappellin, L., Biasioli, F., Fabris, A., Schuhfried, E., Soukoulis, C., Märk, T. D., and Gasperi, F.: Improved mass accuracy in PTR-TOF-MS: Another step towards better compound identification in PTR-MS, International Journal of Mass Spectrometry, 290, 60 – 63, doi:10.1016/j.ijms. 2009.11.007, URL http://www.sciencedirect.com/science/article/pii/S1387380609003571, 2010.

Chen, J. and Griffin, R. J.: Modeling secondary organic aerosol formation from oxidation of alpha-pinene, beta-pinene, and d-limonene, Atmospheric Environment, 39, 7731–7744, 2005.

Goldstein, A. H. and Galbally, I. E.: Known and Unexplored Organic Constituents in the Earth's Atmosphere, Environmental Science & Technology, 41, 1514–1521, 2007.

Hallquist, M., Wenger, J. C., Baltensperger, U., Rudich, Y., Simpson, D., Claeys, M., Dommen, J., Donahue, N. M., George, C., Goldstein, A. H., Hamilton, J. F., Herrmann, H., Hoffmann, T., Iinuma, Y., Jang, M., Jenkin, M., Jimenez, J. L., Kiendler-Scharr, A., Maenhaut, W., McFiggans, G., Mentel, T. F., Monod, A., PrÃ©vÃ´t, A. S. H., Seinfeld, J. H., Surratt, J. D., Szmigielski, R., and Wildt, J.: The formation, properties and impact of secondary organic aerosol: current and emerging issues, Atmospheric Chemistry and Physics, 9, 3555–3762, 2009.

Hartung, J., Elpelt, B., and Klösener, K.-H.: Statistik: Lehr- und Handbuch der angewandten Statistik, Oldenbourg Wissenschaftsverlag, 15. Auflage, 2009.

Hawkins, J. E. and Armstrong, G. T.: Physical and Thermodynamic Properties of Terpenes. III. The Vapor Pressures of alpha-Pinene and beta-Pinene, Journal of the American Chemical Society, 76, 3756–3758, doi:10.1021/ja01643a051, URL http://pubs.acs.org/doi/abs/10.1021/ja01643a051, 1954.

REFERENCES

Hohaus, T.: Development of a new online method for compound specific measurements of organic aerosols, Doktorarbeit, Forschungszentrum Jülich, 2009.

Hohaus, T., Trimborn, D., Kiendler-Scharr, A., Gensch, I., Laumer, W., Kammer, B., Andres, S., Boudries, H., Smith, K. A., Worsnop, D. R., and Jayne, J. T.: A new aerosol collector for quasi on-line analysis of particulate organic matter: the Aerosol Collection Module (ACM) and first applications with a GC/MS-FID, Atmospheric Measurement Techniques, 3, 1423–1436, doi:10.5194/amt-3-1423-2010, URL `http://www.atmos-meas-tech.net/3/1423/2010/`, 2010.

IPCC: Climate Change 2001: The Scientific Basis, Cambridge University Press, UK, 2001.

IPCC: Climate Change 2007: The Physical Science Basis, Cambridge University Press, UK, 2007.

Jayne, J. T., Leard, D. C., Zhang, X. F., Davidovits, P., Smith, K. A., Kolb, C. E., and Worsnop, D. R.: Development of an aerosol mass spectrometer for size and composition analysis of submicron particles, Aerosol Science and Technology, 33, 49–70, 2000.

Jenkin, M. E.: Modelling the formation and composition of secondary organic aerosol from alpha- and beta-pinene ozonolysis using MCM v3, Atmospheric Chemistry and Physics, 4, 1741–1757, 2004.

Jimenez, J. L., Canagaratna, M. R., Donahue, N. M., Prevot, A. S. H., Zhang, Q., Kroll, J. H., DeCarlo, P. F., Allan, J. D., Coe, H., Ng, N. L., Aiken, A. C., Docherty, K. S., Ulbrich, I. M., Grieshop, A. P., Robinson, A. L., Duplissy, J., Smith, J. D., Wilson, K. R., Lanz, V. A., Hueglin, C., Sun, Y. L., Tian, J., Laaksonen, A., Raatikainen, T., Rautiainen, J., Vaattovaara, P., Ehn, M., Kulmala, M., Tomlinson, J. M., Collins, D. R., Cubison, M. J., E., Dunlea, J., Huffman, J. A., Onasch, T. B., Alfarra, M. R., Williams, P. I., Bower, K., Kondo, Y., Schneider, J., Drewnick, F., Borrmann, S., Weimer, S., Demerjian, K., Salcedo, D., Cottrell, L., Griffin, R., Takami, A., Miyoshi, T., Hatakeyama, S., Shimono, A., Sun, J. Y., Zhang, Y. M., Dzepina, K., Kimmel, J. R., Sueper, D., Jayne, J. T., Herndon, S. C., Trimborn, A. M., Williams, L. R., Wood, E. C., Middlebrook, A. M., Kolb, C. E., Baltensperger, U., and Worsnop, D. R.: Evolution of Organic Aerosols in the Atmosphere, Science, 326, 1525–1529, doi:10.1126/science.1180353, URL `http://www.sciencemag.org/content/326/5959/1525.abstract`, 2009.

Jordan, A., Haidacher, S., Hanel, G., Hartungen, E., Märk, L., Seehauser, H., Schottkowsky, R., Sulzer, P., and Märk, T.: A high resolution and high sensitivity proton-transfer-reaction time-of-flight mass spectrometer (PTR-TOF-MS), International Journal of Mass Spectrometry, 286, 122 – 128, doi:10.1016/j.ijms.2009.07.005, URL `http://www.sciencedirect.com/science/article/pii/S1387380609002371`, 2009.

Kanakidou, M., Seinfeld, J. H., Pandis, S. N., Barnes, I., Dentener, F. J., Facchini, M. C., Dingenen, R. v., Ervens, B., Nenes, A., Nielsen, C. J., Swietlicki, E., Putaud, J. P., Balkanski, Y., Fuzzi, S., Horth, J., Moortgat, G. K., Winterhalter, R., Myhre, C. E. L., Tsigaridis, K., Vignati, E., Stephanou, E. G., and Wilson, J.: Organic aerosol and global climate modelling: a review, Atmospheric Chemistry and Physics, 5, 1053–1123, 2005.

Kiehl, J. T.: Twentieth century climate model response and climate sensitivity, Geophys. Res. Lett., 34, L22 710–, URL `http://dx.doi.org/10.1029/2007GL031383`, 2007.

Kim, S., Karl, T., Guenther, A., Tyndall, G., Orlando, J., Harley, P., Rasmussen, R., and Apel, E.: Emissions and ambient distributions of Biogenic Volatile Organic Compounds (BVOC) in a ponderosa pine ecosystem: interpretation of PTR-MS mass spectra, Atmospheric Chemistry and Physics, 10, 1759–1771, doi:10.5194/acp-10-1759-2010, URL `http://www.atmos-chem-phys.net/10/1759/2010/`, 2010.

Koch, D., Schulz, M., Kinne, S., McNaughton, C., Spackman, J. R., Balkanski, Y., Bauer, S., Berntsen, T., Bond, T. C., Boucher, O., Chin, M., Clarke, A., De Luca, N., Dentener, F., Diehl, T., Dubovik, O., Easter, R., Fahey, D. W., Feichter, J., Fillmore, D., Freitag, S., Ghan, S., Ginoux, P., Gong, S., Horowitz, L., Iversen, T., Kirkevåg, A., Klimont, Z., Kondo, Y., Krol, M., Liu, X., Miller, R., Montanaro, V., Moteki, N., Myhre, G., Penner, J. E., Perlwitz, J., Pitari, G., Reddy, S., Sahu, L., Sakamoto, H., Schuster, G., Schwarz, J. P., Seland, Ø., Stier, P., Takegawa, N., Takemura, T., Textor, C., van Aardenne, J. A., and Zhao, Y.: Evaluation of black carbon estimations in global aerosol models, Atmospheric Chemistry and Physics, 9, 9001–9026, doi:10.5194/acp-9-9001-2009, URL `http://www.atmos-chem-phys.net/9/9001/2009/`, 2009.

Kulmala, M., Asmi, A., Lappalainen, H. K., Baltensperger, U., Brenguier, J.-L., Facchini, M. C., Hansson, H.-C., Hov, Ø., O'Dowd, C. D., Pöschl, U., Wiedensohler, A., Boers, R., Boucher, O., de Leeuw, G., Denier van der

121

Gon, H. A. C., Feichter, J., Krejci, R., Laj, P., Lihavainen, H., Lohmann, U., McFiggans, G., Mentel, T., Pilinis, C., Riipinen, I., Schulz, M., Stohl, A., Swietlicki, E., Vignati, E., Alves, C., Amann, M., Ammann, M., Arabas, S., Artaxo, P., Baars, H., Beddows, D. C. S., Bergström, R., Beukes, J. P., Bilde, M., Burkhart, J. F., Canonaco, F., Clegg, S. L., Coe, H., Crumeyrolle, S., D'Anna, B., Decesari, S., Gilardoni, S., Fischer, M., Fjaeraa, A. M., Fountoukis, C., George, C., Gomes, L., Halloran, P., Hamburger, T., Harrison, R. M., Herrmann, H., Hoffmann, T., Hoose, C., Hu, M., Hyvärinen, A., Hõrrak, U., Iinuma, Y., Iversen, T., Josipovic, M., Kanakidou, M., Kiendler-Scharr, A., Kirkevåg, A., Kiss, G., Klimont, Z., Kolmonen, P., Komppula, M., Kristjánsson, J.-E., Laakso, L., Laaksonen, A., Labonnote, L., Lanz, V. A., Lehtinen, K. E. J., Rizzo, L. V., Makkonen, R., Manninen, H. E., McMeeking, G., Merikanto, J., Minikin, A., Mirme, S., Morgan, W. T., Nemitz, E., O'Donnell, D., Panwar, T. S., Pawlowska, H., Petzold, A., Pienaar, J. J., Pio, C., Plass-Duelmer, C., Prévôt, A. S. H., Pryor, S., Reddington, C. L., Roberts, G., Rosenfeld, D., Schwarz, J., Seland, Ø., Sellegri, K., Shen, X. J., Shiraiwa, M., Siebert, H., Sierau, B., Simpson, D., Sun, J. Y., Topping, D., Tunved, P., Vaattovaara, P., Vakkari, V., Veefkind, J. P., Visschedijk, A., Vuollekoski, H., Vuolo, R., Wehner, B., Wildt, J., Woodward, S., Worsnop, D. R., van Zadelhoff, G.-J., Zardini, A. A., Zhang, K., van Zyl, P. G., Kerminen, V.-M., S Carslaw, K., and Pandis, S. N.: General overview: European Integrated project on Aerosol Cloud Climate and Air Quality interactions (EUCAARI) – integrating aerosol research from nano to global scales, Atmospheric Chemistry and Physics, 11, 13 061–13 143, doi:10.5194/acp-11-13061-2011, URL `http://www.atmos-chem-phys.net/11/13061/2011/`, 2011.

Lindinger, W., Hansel, A., and Jordan, A.: On-line monitoring of volatile organic compounds at pptv levels by means of proton-transfer-reaction mass spectrometry (PTR-MS) - Medical applications, food control and environmental research, International Journal of Mass Spectrometry, 173, 191–241, 1998.

McFiggans, G., Topping, D. O., and Barley, M. H.: The sensitivity of secondary organic aerosol component partitioning to the predictions of component properties - Part 1: A systematic evaluation of some available estimation techniques, Atmospheric Chemistry and Physics, 10, 10 255–10 272, doi:10.5194/acp-10-10255-2010, URL `http://www.atmos-chem-phys.net/10/10255/2010/`, 2010.

Pankow, J. F.: An absorption model of gas/particle partitioning of organic

compounds in the atmosphere, Atmospheric Environment, 28, 185–188, 1994.

Saathoff, H., Moehler, O., Schurath, U., Kamm, S., Dippel, B., and Mihelcic, D.: The AIDA soot aerosol characterisation campaign 1999, Journal of Aerosol Science, 34, 1277 – 1296, doi:10.1016/S0021-8502(03)00363-X, URL http://www.sciencedirect.com/science/article/pii/S002185020300363X, ¡ce:title¿Intercomparison of Soot Measurement Techniques¡/ce:title¿, 2003.

Saathoff, H., Naumann, K.-H., Möhler, O., Jonsson, Å. M., Hallquist, M., Kiendler-Scharr, A., Mentel, T. F., Tillmann, R., and Schurath, U.: Temperature dependence of yields of secondary organic aerosols from the ozonolysis of alpha-pinene and limonene, Atmospheric Chemistry and Physics, 9, 1551–1577, doi:10.5194/acp-9-1551-2009, URL http://www.atmos-chem-phys.net/9/1551/2009/, 2009.

Seinfeld, J. H. and Pandis, S. N.: Atmospheric Chemistry and Physics: From Air Pollution to Climate Change, Wiley-Interscience, 2006.

Seinfeld, J. H. and Pankow, J. F.: Organic Atmospheric Particulate Material, Annual Review of Physical Chemistry, 54, 121–140, 2003.

Spracklen, D. V., Carslaw, K. S., Pöschl, U., Rap, A., and Forster, P. M.: Global cloud condensation nuclei influenced by carbonaceous combustion aerosol, Atmospheric Chemistry and Physics, 11, 9067–9087, doi:10.5194/acp-11-9067-2011, URL http://www.atmos-chem-phys.net/11/9067/2011/, 2011.

Tani, A., Hayward, S., and Hewitt, C.: Measurement of monoterpenes and related compounds by proton transfer reaction-mass spectrometry (PTR-MS), International Journal of Mass Spectrometry, 223-224, 561 – 578, doi:10.1016/S1387-3806(02)00880-1, URL http://www.sciencedirect.com/science/article/pii/S1387380602008801, in Memoriam of Werner Lindinger, 2003.

Tillmann, R.: Bildung sekundärer organischer Aerosole durch die Oxidation von Monoterpenen: Ein massenspektrometrischer Ansatz zur Auswertung von Atmosphären-Simulationskammer Experimenten, Ph.D. thesis, Forschungszentrum Jülich, 2007.

Tillmann, R., Hallquist, M., Jonsson, Å. M., Kiendler-Scharr, A., Saathoff, H., Iinuma, Y., and Mentel, T. F.: Influence of relative humidity

and temperature on the production of pinonaldehyde and OH radicals from the ozonolysis of α-pinene, Atmospheric Chemistry and Physics, 10, 7057–7072, doi:10.5194/acp-10-7057-2010, URL `http://www.atmos-chem-phys.net/10/7057/2010/`, 2010.

Yu, J., III, D. R. C., Griffin, R. J., Flagan, R. C., and Seinfeld, J. H.: Gas-Phase Ozone Oxidation of Monoterpenes: Gaseous and Particulate Products, Journal of Atmospheric Chemistry, 34, 207–258, 1999.

Zhang, Q., Jimenez, J. L., Canagaratna, M. R., Allan, J. D., Coe, H., Ulbrich, I., Alfarra, M. R., Takami, A., Middlebrook, A. M., Sun, Y. L., Dzepina, K., Dunlea, E., Docherty, K., DeCarlo, P. F., Salcedo, D., Onasch, T., Jayne, J. T., Miyoshi, T., Shimono, A., Hatakeyama, S., Takegawa, N., Kondo, Y., Schneider, J., Drewnick, F., Borrmann, S., Weimer, S., Demerjian, K., Williams, P., Bower, K., Bahreini, R., Cottrell, L., Griffin, R. J., Rautiainen, J., Sun, J. Y., Zhang, Y. M., and Worsnop, D. R.: Ubiquity and dominance of oxygenated species in organic aerosols in anthropogenically-influenced Northern Hemisphere midlatitudes, Geophysical Research Letters, 34, 2007.

Zhao, J. and Zhang, R.: Proton transfer reaction rate constants between hydronium ion (H3O+) and volatile organic compounds, Atmospheric Environment, 38, 2177 – 2185, doi:10.1016/j.atmosenv.2004.01.019, URL `http://www.sciencedirect.com/science/article/pii/S1352231004000895`, 2004.

List of Figures

List of Tables

Abbrevations

ACM	Aerosol Collection Module
AIDA	Aerosol Interaction and Dynamics in the Atmosphere
AMS	Aerosol Mass Spectrometer
GC-MS	Gas Chromatography - Mass Spectrometer
IUPAC	International Union of Pure and Applied Chemistry
KIT	Karlsruhe Institute of Technology
NIST	National Institute of Standards and Technology
OA	Organic Aerosol
PIKA	Peak Integration by Key Analysis
ppb	Parts Per Billion
PTR-MS	Proton Transfer Reaction - Mass Spectrometer
PTR-ToF-MS	Proton Transfer Reaction - Time of Flight - Mass Spectrometer
QMS	Quadrupole Mass Spectrometer
SMPS	Scanning Mobility Particle Sizer
SOA	Secondary Organic Aerosol
SQUIRREL	SeQUential Igor data RetRiEvaL
ToF-AMS	Time of Flight - Aerosol Mass Spectrometer
VOC	Volatile Organic Compounds

Danksagung

Zum Abschluss dieser Arbeit möchte ich mich von ganzem Herzen bei allen bedanken, die diese Promotion ermöglicht und mich bei der Arbeit daran unterstützt haben.

Prof. R. Koppmann möchte ich ganz herzlich für die Übernahme des Referats danken und für die Zeit und Hilfe, die er mir mit seinen konstruktiven Anregungen gewidmet hat.

Ich möchte mich ebenso herzlich bei Prof. A. Wahner für die Übernahme des Koreferates bedanken und dass mir ermöglicht wurde, am Forschungszentrum Jülich in dieses spannende Forschungsfeld einzutauchen.

Mein besonderer Dank gilt meiner Betreuerin Prof. Astrid Kiendler-Scharr. Selten habe ich von einer derart engagierten Betreuung gehört, wie ich sie erfahren habe. Die fruchtbaren Diskussionen und vielen Anregungen haben entscheidend zu dieser Arbeit beigetragen.

Desweiteren möchte ich mich bei folgenden Personen bedanken:

Bei der gesamten Hetero-Gruppe für das unterstützende und fruchtbare Arbeitsklima. Besonders für die Hilfe in allen chemischen aber auch in anderen Belangen möchte ich PD Dr. Thomas Mentel, Dr. Ralf Tillmann, Dr. Iulia Gensch und Florian Rubach danken. Dr. Uwe Kuhn danke ich für das ausgesprochen harmonische und sehr unterstützende Büroklima und die Bereitschaft, sich in alle Belange mit einzudenken und wertvolle Hinweise zu geben.

Dr. Thorsten Hohaus möchte ich sowohl für die Einführung in die Arbeit mit PTR-ToF-MS und ACM wie auch für die anhaltende Unterstützung im Nachhinein danken.

Helga London und Michael Decker möchte ich für die vielen Unterstützungen und Erleichterungen im IT-Bereich, Hilfe bei LaTeX-Problemen und für Unterhaltungen danken, die einen auch mal wieder an das eigentliche Leben erinnern.

Wolfgang Lüdtke danke ich für die gute Zusammenarbeit bei der Weiterentwicklung des ACM.

Brigitte Berger, Gabi Nork und Franziska Kaspereit danke ich für ihre aus-